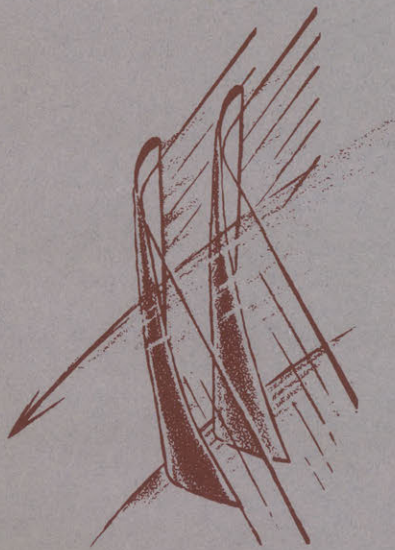


Last Copy do not Remove

**GAS TURBINE
LIBRARY
REPORT NO. 97**

A LIGHT SCATTERING INVESTIGATION OF DROPLET GROWTH IN NOZZLE CONDENSATION

RICHARD ROBERTS



Research was carried out under the Sponsorship of the U.S. Navy, Office of Naval Research, Power Branch

Contract Nonr 3963(07)

FEBRUARY 1969

**GAS TURBINE LABORATORY
MASSACHUSETTS INSTITUTE OF TECHNOLOGY
CAMBRIDGE, MASSACHUSETTS 02139**

A LIGHT SCATTERING INVESTIGATION OF DROPLET GROWTH
IN NOZZLE CONDENSATION

by

Richard Roberts

Research was carried out under the
Sponsorship of the U. S. Navy, Office
of Naval Research, Power Branch
Contract Nonr 3963(07)

GAS TURBINE LABORATORY

REPORT No. 97

February 1969

MASSACHUSETTS INSTITUTE OF TECHNOLOGY

Cambridge, Massachusetts

ABSTRACT

An experimental and theoretical study has been made of the condensation of water vapor (with air carrier) in a supersonic nozzle in order to investigate the possible existence of condensate droplets which are substantially larger than predicted by the standard application of classical condensation theory. Droplet size was measured using light scattering techniques, which when combined with the total mass concentration of condensate, provided limits on the maximum and average droplet size.

It was found that approximately one part in 10^3 of the droplet concentration reached a size a factor of 10 greater than predicted by the classical theory (radius in range 400 - 1000 $\overset{\circ}{\text{A}}$ for water mass fractions in range $.005 < \omega_0 < .015$). The maximum droplet size, furthermore, was not seen to decrease proportionately as the nucleation zone was approached, indicating that the larger droplets are formed during the early stages of condensation. Inconclusive evidence suggests that this occurs following the completion of nucleation but before the vapor supply is exhausted.

A calculation procedure which allowed the separation of the nuclei into a distribution of sizes, arising from a varying stability criterion and radius dependent growth rate, resulted in the establishment of a qualitatively correct distribution shape but no theoretical substantiation of an aging or coarsening mechanism. A separate application of Brownian coagulation theory to surface-averaged condensation theory resulted in the prediction that the average droplet size increased by a factor of between 2.5 and 4. No conclusion could be drawn concerning the actual existence of this size increase due to the level of uncertainty in the determination of average droplet size.

ACKNOWLEDGEMENTS

In the development of this work to its present state of completion, the author has come into the debt of a great many people for their advice and assistance. Although it is impossible to acknowledge each individually, sincere thanks are offered to all who have helped.

The author would like to extend special thanks to his thesis advisor, Professor Philip G. Hill, and the other members of his thesis committee, Professor Kenneth C. Russell of the Dept. of Metallurgy, Professor David G. Wilson and Professor William H. Dalzell of the Dept. of Chemical Engineering for their ever-available guidance and assistance. The author would also like to thank Professor Edward S. Taylor, past director of the Gas Turbine Laboratory, and Professor Jack L. Kerrebrock, present director, both for their interest in this work and for the pleasant and stimulating atmosphere which is to be found in the G.T.L.

In addition, the contributions of the following people are gratefully acknowledged:

Mrs. Joan Moore, for her indispensable help in the preparation of the computer programs.

Mr. Thorwald Christensen, for his help with the photography and innumerable other items which position themselves squarely in the path of progress.

John Roberts, the author's brother, for the many hours spent in the reduction of experimental data.

The author's support for the year 1966-67 was provided by a National Science Foundation Graduate Traineeship. This was followed by the appointment to a full-time research assistantship in the Gas Turbine Laboratory, made possible by the sponsorship of the U.S. Navy, Office of Naval Research (Power Branch), contract Nonr 3963(07). Support for the summer of 1968 came from a grant to the Department of Mechanical Engineering made by the E.I. du Pont de Nemours Companies. This assistance is gratefully acknowledged.

Finally, a measure of deep appreciation must go to the author's wife, Judy, in recognition of everything that she has done to make this work possible. In addition to providing the necessary encouragement and moral support, there were the many long hours spent in all-night lab sessions, in data reduction and in converting this report to typed form.

TABLE OF CONTENTS

	page
Abstract	ii
Acknowledgements	iii
Table of Contents	iv
List of Figures	vii
List of Tables	x
Nomenclature	xi
I. INTRODUCTION	1
A. Background and Previous Work	1
B. Introduction to the Present Study	5
II. EXPERIMENTAL PROGRAM	8
A. Preliminary Considerations	8
B. Application of Light Scattering Theory	10
1. The general Mie theory	10
2. Some limiting cases and techniques	13
3. Application to the present experiment	19
C. Apparatus and Procedure	27
1. Nozzle and related equipment	28
(a) Carrier air supply	28
(b) Nozzle	29
(c) Water vapor injection apparatus	32
2. Light scattering apparatus	34
(a) Incident light source	36
(b) Multiplier phototube	37

	page
(c) The rotating arm	39
3. Experimental procedure	40
D. Interpretation of Experimental Results	42
1. Data reduction	42
2. Estimation of experimental error	43
III. THEORETICAL PROGRAM	47
A. Classical Condensation Theory	48
1. Nucleation rate	48
2. Droplet growth	52
3. Gas dynamics	55
4. Application of condensation theory	59
B. Differential Growth and the Aging Phenomenon	61
C. Brownian Coagulation	64
D. Coagulation due to Directed Motion	66
IV. PRESENTATION AND DISCUSSION OF RESULTS	69
V. CONCLUSIONS	77
A. Application of Light Scattering Theory	77
B. Condensation Theory and Coagulation Mechanisms	78
C. Comparison of Theory to Experiment	79
VI. RECOMMENDATIONS FOR FURTHER STUDY	81
REFERENCES	82
APPENDIX A	88
A.1 Formulation of the Mie angular intensity functions i_1 and i_2 for spheres of arbitrary size	88

	page
A.2 Transformations and calculation procedures used in the evaluation of i_1 and i_2	90
A.3 The estimation of particle size and size distribution	95
(a) Light scattering average size	95
(b) Upper limiting average size for a delta distribution at $\bar{\alpha}$.	97
(c) Particle size distribution	99
APPENDIX B	103
B.1 Scattering geometry	103
B.2 Photomultiplier calibration	104
B.3 The comparison of scattered to incident intensity	105
B.4 Alignment procedures	107
APPENDIX C - Calculation Procedure for Vapor Mass Fraction	110
APPENDIX D - Brownian Coagulation	113
D.1 Collision frequency by continuum theory	114
D.2 Collision frequency by free molecule theory	116
D.3 The transition zone	117
D.4 Application of the theory	118
APPENDIX E - Coagulation by Slip-Collision	122
APPENDIX F - Tabulation of Experimental Data	126
FIGURES 1 - 27	

LIST OF FIGURES

1. Definition of perpendicular and parallel components of scattered and incident light; plane of observation.
2. Angular intensity functions, i_1 , i_2 , versus angle of observation, θ ;
 - (a) $0.1 < \alpha < 1.0$, $m = 1.33$
 - (b) $1.0 < \alpha < 4.0$, $m = 1.33$
3. Distribution functions satisfying light scattering data for $\omega_o = .015$, $(P/P_o)_i = .30$, distance from throat = 4.5 in.
 - (a) Number distribution, $p(\alpha)$
 - (b) Mass distribution, $\alpha^3 p(\alpha)$
 - (c) Scattered intensity distribution, $I_1(90^\circ)p(\alpha)$
4. Fraction of mass responsible for 90% of scattered light versus dividing size, 10-90% scattered intensity.
5. Maximum average size versus dividing size, 10-90% scattered intensity.
6. Particle size distribution versus distance from throat; assumed minimum size of $\alpha = 0.04$, $\omega_o = .010$, $(P/P_o)_i = 0.26$.
7. Layout of experimental apparatus (1)
8. Layout of experimental apparatus (2)
9. Details of nozzle construction
10. External view of nozzle
11. Nozzle area ratio versus distance from throat
12. Schematic of vapor injection apparatus
13. Typical X-Y recorder trace; experimental scattered light intensity
14. Number of particles N_r versus average group radius for water vapor in air.

15. Growth history of group radii and their relation to the critical radius.
16. Number of particles \bar{n} versus average group radius for pure water vapor.
17. Vapor pressure and temperature at incidence of condensation.
18. Maximum and average droplet size from light scattering measurements.
 - (a) $\omega_o = .005$
 - (b) $\omega_o = .010$
 - (c) $\omega_o = .015$
19. Droplet concentration from light scattering measurement and condensation theory versus point of incidence.
 - (a) $\omega_o = .005$
 - (b) $\omega_o = .010$
 - (c) $\omega_o = .015$
20. Droplet size versus distance from throat; comparison of theory and experiment.
 - (a) $\omega_o = .005, (P/P_o)_i = .42$
 - (b) $\omega_o = .005, (P/P_o)_i = .33$
 - (c) $\omega_o = .005, (P/P_o)_i = .26$
 - (d) $\omega_o = .005, (P/P_o)_i = .23$
 - (e) $\omega_o = .010, (P/P_o)_i = .45$
 - (f) $\omega_o = .010, (P/P_o)_i = .34$
 - (g) $\omega_o = .010, (P/P_o)_i = .27$
 - (h) $\omega_o = .015, (P/P_o)_i = .42$
 - (i) $\omega_o = .015, (P/P_o)_i = .35$
 - (j) $\omega_o = .015, (P/P_o)_i = .30$

21. Comparison between theory and experiment, $\alpha = 0.325$
22. (a) Schematic of light scattering geometry.
(b) Variation of scattering volume with angle.
23. Dimensions of scattered light detection system.
24. (a) Exit plane target
(b) Position of alignment images on nozzle target
25. (a) Pattern observation when aligning phototube housing
(b) Alignment pattern with rectangular aperture installed.
26. Variation in collision rate with Knudsen number for a homogeneous aerosol.
27. Particle drag coefficient versus Mach number for Reynold's number = .01, 5, 100.

LIST OF TABLES

(Appendix F)

- F.1 Theoretical Distribution Parameters
- F.2 Experimental Scattered Light Intensity (millivolts)
- F.3 Experimental Static Pressure Ratios, Nozzle Flow Conditions

PRINCIPAL NOMENCLATURE

A list of the principal notation follows. Other symbols are defined as they appear.

A	nozzle flow area
A*	nozzle flow area at throat
c _L	specific heat of condensate
c _p	specific heat of a perfect gas at constant pressure
c _v	specific heat of a perfect gas at constant volume
g*	number of molecules in a critical sized cluster
ΔG*	free energy of formation of a critical sized cluster
h	scaling factor for assumed family of distribution curves, no./unit volume
h _f	specific enthalpy of condensate
h _{fg}	latent heat of vaporization
I	scattered light intensity, from experimental measurement
i	theoretical angular intensity function
J	nucleation rate, units of nuclei/unit volume - time
K	light scattering theory: a combination of geometric calibration factors, constant for given experimental conditions; condensation theory = a constant equal to $(\frac{1}{\gamma - 1} + \frac{1}{2})$
k	Boltzmann's constant
M	Mach number
M'	mass concentration of condensate, units of mass/unit volume
\bar{M}	molecular weight

m	light scattering theory: index of refraction of scattering particle with respect to surrounding medium; other: droplet, particle or molecular mass, as indicated
\dot{m}	mass flow rate
N	number concentration of condensate particles, units of no./unit volume
n	light scattering theory: exponent in assumed family of distribution curves condensation theory: number concentration of vapor molecules
\dot{n}	number of vapor molecules impinging on unit surface area per unit time
P	pressure
p	partial pressure
p(α)	absolute distribution function, units of no./unit volume
R	light scattering theory: distance from scattering volume to point of observation other: gas constant per unit mass
r	droplet radius, radius of scattering particle
r*	radius of critical sized cluster
\bar{r}	surface area averaged radius
T	temperature
t	time
U _f	internal energy of condensate
u	local stream velocity; local droplet velocity
v _L	volume per molecule of liquid phase
x	streamwise coordinate (along nozzle axis)

y_o mole fraction of condensable vapor

Greek Letters

α light scattering theory: dimensionless size parameter
equal to $2\pi r/\lambda$
condensation theory: thermal accommodation coefficient

$\bar{\alpha}$ light scattering average size

α' upper limiting number average size obtained from "missing mass" analysis

β condensation theory: mass flux impinging on droplet surface

Γ "gasification" correction factor to classical nucleation theory

γ ratio of specific heats = c_p/c_v

θ angle of observation, as defined in Figure 1

λ wavelength of incident light

μ condensation theory: mass fraction of condensed moisture
other: viscosity

ξ mass accommodation coefficient

ρ density

σ surface tension

ω_o mass fraction of condensable vapor; specific humidity

Subscripts

1, 2 indicate perpendicular and parallel plane polarization, respectively

0 light scattering theory: refers to incident light intensity
other: refers to initial or stagnation conditions

c	referring to the carrier gas
D	referring to the droplet conditions
i	referring to conditions at incidence of condensation
L	referring to the liquid state
max.	referring to the maximum value of size parameter
min.	referring to the minimum value of size parameter
v	referring to the vapor
∞	referring to conditions at the flat-film equilibrium state

I. INTRODUCTION

A. Background and Previous Work

From an engineering point of view, the phenomenon of condensation is of interest primarily due to the role it plays in various power and propulsion systems. Of the various types of condensation, homogeneous nucleation from the supersaturated vapor phase, in which nuclei are spontaneously formed from vapor molecules, is the type usually encountered in flow devices and is of more basic theoretical interest. Typically, condensation occurs when a vapor with an initial sub-saturation level is expanded or cooled, producing an unstable supersaturated condition. A large concentration of liquid or solid particles are introduced into the stream and the aerodynamic properties of the flow are altered by the release of the heat of vaporization. In steam turbines, condensation must be considered in performance calculations and blade erosion from the resulting water droplets can be the limiting factor in operating life. In hypersonic wind tunnels, condensation will cause a change in aerodynamic characteristics and requires a reliable calculation method to predict actual performance. Also, condensation of metallic vapors in rocket nozzles can cause considerable thrust losses. The recent increase in attention given to homogeneous nucleation stems both from the discovery that classical theory is not always applicable to fluids other than water vapor and from current trends in new power systems. With the increased use of different operating fluids, such as metal vapors in closed loop reactors, condensation studies have been extended to a larger range of materials. The ultimate goal is to develop a theoretical correlation which will accurately predict the

condensation behavior of any given fluid under given operating conditions. This is particularly desirable when one considers that, for a variety of reasons, many fluids are not amenable to extensive experimentation.

The condensation phenomenon was observed well before a theoretical treatment was available. The initial experiments were done in cloud chambers by Wilson⁽¹⁾ and Powell⁽²⁾ with water vapor as the condensing fluid. Much additional work has been done, mainly using water vapor; Hirth and Pound⁽³⁾ provide a useful review of the experimental data. However, there appear to be major difficulties associated with the use of the cloud chamber for incidence studies. The most serious is that the method depends on the visual sighting of a condensed cloud, something that may vary among observers and which certainly occurs sometime after the actual incidence of nucleation. Also, due to the relatively slow expansion rate, any appreciable concentration of foreign particles (dust) or ions will favor heterogeneous nucleation. Finally, the observations are qualitative rather than quantitative.

Owing to the difficulties in interpreting cloud chamber data and to the fact that condensation in nozzles has direct application to engineering problems, the supersonic nozzle has been used as an alternative for studying the condensation process. As demonstrated by Stodola⁽⁴⁾ and others, the expansion is sufficiently rapid that homogeneous nucleation should prevail even at the highest conceivable concentrations of dust or ions. (The exception here is when there is a precondensing vapor present in the flow.) In fact, the expansion rate is so much faster that it affects the critical supersaturation; growth rates can no longer be considered to be "infinitely" rapid and a drop growth

mechanism must be included in a theoretical description of the process. Other advantages of nozzle studies are that a continuous process is being viewed, that the incidence of condensation and downstream growth can be quantitatively deduced from static pressure data, and that wall effects are virtually eliminated by the presence of a boundary layer at near stagnation conditions. Furthermore, a one-dimensional frictionless gas dynamic model is a very good approximation for typical experiments.

A substantial number of nozzle experiments have been performed using pure water vapor, water vapor in air, and a number of other fluids. The existing data on water vapor have been comprehensively reviewed by Hill⁽⁵⁾⁽⁶⁾. Data on other fluids are not as plentiful and are generally more recent. Hill et. al.⁽⁷⁾ have treated the case of metal vapors. Air and its principal components, relating to hypersonic wind tunnel practice, have been studied most recently by Daum and Gyarmathy⁽⁸⁾, who include a comprehensive bibliography of earlier investigations. A recent series of tests have been conducted in the Gas Turbine Laboratory using a variety of fluids in an effort to further refine the experimental correlation of existing theories. Kremmer and Okurounmu⁽⁹⁾ studied pure ammonia, Jaeger⁽¹⁰⁾ used water vapor and ammonia with an air carrier, Duff⁽¹¹⁾ used pure carbon dioxide and Dawson⁽¹²⁾ investigated the behavior of several organic vapors.

The theoretical treatment of condensation requires a nucleation theory, which predicts the formation of stable clusters, and a droplet growth theory, by which these nuclei increase in size. There are presently two conflicting versions of nucleation theory. The earlier

approach, now called the classical theory, is derived from classical thermodynamics. It is most frequently connected with the names of Volmer, Becker and Döring, and Zeldovich; these early contributions and many others are reviewed by Feder et. al.⁽¹³⁾. Lothe and Pound⁽¹⁴⁾ and others have proposed a revised theory in which the partition functions for the rotational and translational degrees of freedom of the nuclei are explicitly taken into account. This results in about a 10^{15} - 10^{17} factor increase in the predicted nucleation rate over that predicted by classical theory. The new work, however, has been challenged⁽¹⁵⁾ and the debate continues. There are in addition uncertainties associated with thermal and mass accommodation coefficients and with the applicability of bulk surface tension values to a cluster containing 10-100 molecules, but these are not large enough to obscure the difference between the classical and revised theories. The droplet growth process is assumed to be thermal diffusion limited and is presently not a matter of dispute.

While the revised theory is believed to be more theoretically correct, the experimental data do not always bear this out. Oswatitsch⁽¹⁶⁾ and Hill⁽⁵⁾⁽⁶⁾ have shown that water vapor behaves as predicted by classical theory. Following experiments in the Gas Turbine Laboratory, carbon dioxide has been shown to obey classical theory with the assumption of supercooled liquid droplets below the triple point⁽¹⁷⁾; ammonia, chloroform, benzene and Freon 11, on the other hand, adhere to the revised theory. The present state of affairs is that although many substances are empirically well understood, there is as yet no universally applicable condensation theory.

A great majority of the work to date has concerned itself with the

measurement and prediction of incidence of nucleation. Along with incidence behavior, condensation theory provides a prediction of condensate particle size and number concentration as a function of distance from the nucleation zone. It would appear that experimental measurements of these quantities would enable the absolute verification of condensation theory for the fluid in question. This has been done in two independent experiments, using water vapor in air as the condensing medium. Thomann⁽¹⁸⁾ employed a probe sampling technique in a low pressure wind tunnel. Working with water mass fractions less than .0007, he measured ice particles having a radius of $14\overset{\circ}{\text{A}}$, invariant with humidity. No concentration measurements were made. Wegener and Stein⁽¹⁹⁾⁽²⁰⁾ used a light scattering technique and a 5° included angle, two-dimensional nozzle exhausting from atmospheric pressure into a vacuum. The water mass fraction was varied over the range $.001 < \omega_0 < .01$ and measurements were taken at a distance of between 1 and 4 cm. from the nucleation zone. Condensate particle radius varied as $20\text{--}60\overset{\circ}{\text{A}}$ and number concentration varied as $2 \times 10^{12} - 10 \times 10^{12}$ with increasing ω_0 . Both studies fully support the classical nucleation theory. Wegener and Stein, however, were unable to differentiate between supercooled liquid drops and ice crystals exhibiting reduced surface tension (equilibrium considerations require that the condensate be in the form of ice crystals at temperatures below the triple point).

B. Introduction to the Present Study

In certain areas, such as the investigation of turbine erosion or the design of colloid ion propulsion systems, it is important to be able

to accurately predict the size, and the size distribution, of condensate particles that will occur. In view of the good agreement between theory and experiment in the above investigations, this would appear to be a minor problem. However, a number of observations have indicated that larger particles can in fact be formed.

Yellot⁽²¹⁾⁽²²⁾, investigating condensing steam, and Duff⁽¹¹⁾, working with pure carbon dioxide, report visual observation of a condensate cloud coincident with the point of onset of condensation as determined from pressure measurements. This observation remained valid despite changes which resulted in the axial shift of condensation in the nozzle. It is to be expected that substantial nucleation would occur somewhat before the appearance of a visible cloud due to the theoretically small sizes of the forming nuclei. In addition, erosion damage in steam turbines indicates that micron or supermicron sized drops are present. The theoretically predicted sizes are much smaller and would be able to follow the flow. As a final instance, Linhardt⁽²³⁾ has concluded from experiments with a wedge probe that the condensation droplets obtained from potassium vapor are an order of magnitude larger than would be expected from the theory.

In view of these differing observations, it was decided to further investigate the particle growth process in a supersonic nozzle. The work to be described in what follows was undertaken with the intention of investigating the possibility of producing and measuring larger than predicted condensate droplets. To complement the experimental work, existing condensation theory was re-examined in an attempt to establish a theoretical basis for the existence of these larger droplets. In

particular, theoretical support was sought for the presence of an "aging" process, wherein a given size distribution is continuously transformed to another of larger, more uniform size.

II. EXPERIMENTAL PROGRAM

A. Preliminary Considerations

In an investigation of condensate particle size in a supersonic nozzle, the selection of a measurement technique becomes the first order of business. For the vapor and concentration levels to be studied, the expected size range was 50-5000^oÅ. This is seen to vary from considerably below up to the order of the wavelength of visible light, and serves to eliminate macroscopic optical techniques such as photography and holography. In addition to the limitation imposed by the size range, it is desirable that the measurements be taken without disturbing the flow. A final qualification is that a well established and proven technique should be used if possible. Following treatments by Winkler⁽²⁴⁾ and Durbin⁽²⁵⁾ and the work of Wegener and Stein⁽²⁰⁾, light scattering in one of its variations presented itself as the obvious choice.

Although pure water vapor would have been more applicable to steam turbine problems, it was decided to use water vapor in air due to its ease of handling and its adaptability to existing metering and injection equipment. In addition, a vapor-carrier mixture has the desirable feature that the maximum amount of condensate is fixed by the vapor mass fraction.

In order to maximize the growth aspect of the condensation process, a nozzle whose total length was large compared to the size of the nucleation zone was desired. As will be described later, a conical nozzle having a supply pressure of about eight atmospheres, 0.25 in throat diameter, 1° included angle and length from throat to exit of 12.5 in. was constructed. The flow residence time is about 0.5 millisecond under these conditions. These specifications represent a considerably higher

operating pressure and a much smaller pressure gradient than was used in the previously mentioned size studies.

Light scattering techniques are more easily applied when the optical path is unencumbered by glass windows or container walls, eliminating the need to correct for reflections, etc. With this in mind, it was decided to use a nozzle with atmospheric exit pressure and to take the light scattering measurements in the region just beyond the exit plane. The well known "diamond" shock pattern provides a conical volume beyond the exit plane in which the flow remains supersonic (See Shapiro⁽²⁶⁾, p.143). It was found to be very important that the condensate particles be measured before passing through the shock, as this mechanism was observed to cause an increase in size due to coagulation. No correction was made for the fact that the incident and scattered light beams pass through regions of varying density; this was assumed to be an insignificant source of error since the indices of refraction for air and vacuum differ only in the 4th decimal place⁽²⁷⁾.

To measure particle sizes at points closer to the nucleation zone, another characteristic of supersonic flow was employed: namely, that disturbances propagate at the local speed of sound, with the result that a change in flow conditions at a given point in the nozzle will not affect the flow upstream of this point. Because of this, size data corresponding to a shorter growth time could be taken by the simple expedient of cutting off the end of the nozzle and realigning the optical system to the new exit plane. The alternative of moving the incidence point closer to the exit cannot be used, since the required increase in stagnation temperature exceeds the limit imposed by the plastic nozzle

construction.

B. Application of Light Scattering Theory

1. The general Mie theory

Light can be represented as an electromagnetic wave and as such has a transverse oscillating electric field associated with it, whose direction is normal to the direction of propagation. When this energy passes through a particle, the electric field causes the charges contained in the particle to be set into forced oscillation at a frequency equal to that of the incident light. These vibrating electric charges, in turn, are each sources of electromagnetic radiation, scattered light. To describe the character of this scattered light, it is necessary to account for the size, shape and composition of the scattering particle. This amounts to finding a strict solution to the diffraction problem in its most general sense, i.e. an integration of Maxwell's equations for a plane parallel wave which strikes an arbitrary surface separating two regions of differing optical properties. This operation has proven to be possible only for particles having simple geometric shapes.

The general problem was first solved by Mie⁽²⁸⁾ in 1908 for the case of a single spherical particle suspended in a transparent, homogeneous and isotropic medium. A discussion of this derivation is contained in the book by Born and Wolf⁽²⁹⁾. Mie expressed the solution as the sum of a series of partial solutions, each corresponding to a forced mode of vibration of the spherical particle at the frequency of the incident light. If, in reference to Figure 1, the incident and scattered light is resolved into two mutually perpendicular, plane polarized components, the relations between scattered and incident light

are as follows:

For perpendicular polarization,

$$I_1 = \frac{\lambda^2 i_1}{4\pi^2 R^2} I_{o1} \quad (2.1)$$

for parallel polarization,

$$I_2 = \frac{\lambda^2 i_2}{4\pi^2 R^2} I_{o2} \quad (2.2)$$

and for the total scattered light when the incident light is unpolarized (contains both components),

$$I = \frac{\lambda^2 (i_1 + i_2)}{8\pi^2 R^2} I_o \quad (2.3)$$

where:

λ = wavelength of the incident and scattered light in the medium surrounding the particle.

R = distance from scattering particle to point of observation, which must be large compared to the incident wavelength, λ .

I, I_o = intensities of the scattered and incident light, per unit area and time.

i_1, i_2 = the Mie scattering functions, which take the general form:

$$\begin{aligned} i_1 &= i_1(\alpha, m, \theta) \\ i_2 &= i_2(\alpha, m, \theta) \end{aligned} \quad (2.4)$$

where:

α = dimensionless size parameter $\equiv \frac{2\pi r}{\lambda}$

r = radius of scattering particle

m = index of refraction of scattering particle with respect
to surrounding medium.

θ = angle of observation, as defined in Figure 1.

The complete formulations for i_1 and i_2 are presented in section 1 of Appendix A.

From the equations 2.1-2.4 it can be seen that for mixed values of λ , m , R and the intensity and state of polarization of the incident light, the angular distribution of the scattered intensity is a function only of α . It is interesting to note that, for the case of plane polarized light lying in or perpendicular to the plane of observation, the quantities I_1 and I_2 are dependent only on the corresponding components of the incident light; i.e., a perpendicularly polarized incident beam will theoretically produce only perpendicularly polarized scattered light. (For other orientations, the scattered light will be elliptically polarized.) Polar diagrams of $i_1(\theta)$ and $i_2(\theta)$ for a number of values of α and m are given by Erickson⁽³⁰⁾ and Winkler⁽²⁴⁾.

The scattering theory, given above, is derived for a single particle. In order to apply the Mie results to the present experiment where a large number of particles will be simultaneously observed, it is necessary that the particles act as independent scatterers. If this is the case, the total intensity of scattered light is simply the sum of all the individual scattered intensities. Deviations from independent scattering arise from two sources. First, if there is a sufficient number

of scattering particles in the optical path (proportional to particle concentration, optical path length), the incident beam will be attenuated and all particles will not experience the same incident intensity. The second mechanism, known as multiple scattering, arises when the particles are so closely spaced that the light scattered from one particle will cause secondary scattering from another particle. In the present experiment, independent scattering is assumed to prevail since the particle separation is on the order of 100 times their radius and since the incident beam was not significantly attenuated in passing through the scattering region.

It is further assumed that the scattering particles are spherical and isotropic, neglecting the fact that water is slightly anisotropic at the molecular level. The ergodic condition, in which the time and space averages coincide, may be assumed to apply since the nozzle flow is steady and since there are 10^9 - 10^{10} condensate particles randomly located in the test volume at any given time. It is not always necessary to assume that the scattering particles are of uniform size.

2. Some limiting cases and techniques

By considering the upper and lower limits of light scattering theory, a range of practical application of the method is determined. As presented in Appendix A, the equations for i_1 and i_2 are in the form of infinite series and are quite complex. In calculating these quantities for particular values of α , m and θ , the number of terms that need to be included increases with increasing values of α . When α is very small, i.e. when $r \ll \lambda$, the series converge very rapidly and only the first order electric oscillation term need to be considered. (An additional requirement is that m should be close to 1, so that the incident light will experience minimal distortion in passing through the scattering particle.) Mie's general theory then reduces to the

solution for an electric dipole, as was derived by Lord Rayleigh⁽³¹⁾ prior to the appearance of the general solution. Following Winkler⁽²⁴⁾,

$$i_1 = \frac{64\pi^6 r^6}{\lambda^6} \left| \frac{m^2 - 1}{m^2 + 2} \right|^2 \quad (2.5)$$

$$i_2 = \frac{64\pi^6 r^6}{\lambda^6} \left| \frac{m^2 - 1}{m^2 + 2} \right|^2 \cos^2 \theta$$

$$I = I_1 + I_2 = \frac{8\pi^4 r^6}{R^2 \lambda^4} \left| \frac{m^2 - 1}{m^2 + 2} \right|^2 (1 + \cos^2 \theta) I_0 \quad (2.6)$$

In the range $0 < \alpha < 0.2$, the angular intensity functions (2.5) exhibit no change in slope and hence this fact cannot be used to determine particle size. When a fixed number of particles, N , are contained in the scattering volume, the ratio between scattered and incident intensity can be written with the assumption that the particles are monodisperse (of uniform size). Typically, a measurement is taken at a fixed angle and known polarization. For the case of perpendicular polarization:

$$\frac{I_{\perp}}{I_0} = \frac{16\pi^4}{R^2 \lambda^4} \left| \frac{m^2 - 1}{m^2 + 2} \right|^2 N r^6 \quad (2.7)$$

With the product Nr^6 thus determined, a different combination of these factors must be measured before size and concentration can be separated. In the case of condensation in an inert carrier⁽²⁰⁾, the total mass of particles per unit volume is known, providing the factor $\frac{4}{3} \pi \rho r^3 N$.

The upper limiting case occurs when $\alpha \gg 1$. Here, a great many terms are significant in the determination of i_1 and i_2 , merging into the diffraction pattern for a circular disc. The light scattering solutions reduce to the simpler Huygen's principle as applied to diffraction and reflection problems in physical optics. In such cases, the practical value of Mie's solution diminishes, and approximate macroscopic theories should be used.

When α falls in the range $0.2 < \alpha < 30$, the full Mie solution must be used. If it can be assumed that the scattering particles have uniform size and fixed concentration N , equations 2.1 and 2.2 take the form:

$$I_1 = N \frac{\lambda^2 i_1}{4\pi^2 R^2} I_{o1} \quad (2.8)$$

and

$$I_2 = N \frac{\lambda^2 i_2}{4\pi^2 R^2} I_{o2} \quad (2.9)$$

For fixed experimental conditions, the scattered light intensity is seen to be a function of the product of N and i , the appropriate angular intensity function. Curves of $i_1(\alpha, \theta)$ and $i_2(\alpha, \theta)$ are plotted for the ranges $0.1 < \alpha < 1.0$ (Figure 2a.) and $1.0 < \alpha < 4.0$ (Figure 2b). As can be seen, the angular intensity functions change principally in magnitude and to a lesser degree in shape (slope) up to $\alpha = 1.0$, beyond which point there is a significant variation in detail in the form of relative maxima and minima and a diminishing change in amplitude. For very large values of α , the detail becomes difficult to measure experimentally.

The range $0.1 < \alpha < 1.0$ witnesses the transition from pure Rayleigh scattering, where intensity varies as r^6 with no change in shape, to the case for large α where the location and number of maxima and minima are the primary variables.

The importance of this change in shape of the scattering diagram is that if the particle size is sufficiently large ($\alpha > 0.2$), α may be uniquely determined from it alone. A normalized curve of $I_1(\theta)$ or $I_2(\theta)$, measured with constant incident intensity, is compared with the corresponding normalized curve of $i_1(\alpha, \theta)$ or $i_2(\alpha, \theta)$ calculated from the Mie theory, with α being determined by the best fit between theory and experiment. Here normalized means divided through by the value of intensity of the perpendicular component at 90° , so that all curves have the value 1.0 at this angle. The comparison procedure is necessarily iterative due to the complicated nature of the relationships for i (see Appendix A); the experimental curve of $I_1(\theta)$ or $I_2(\theta)$ is broken down into a series of values at discrete angular intervals and the best fit is taken to be that value of α for which the root-mean-square error between theory and experiment is minimized. When the scattering particles are of uniform size, either $I_1(\theta)$ or $I_2(\theta)$ may be used independently or in any combination since they both provide the same information. The experimental technique may be simplified when α is below 2-2.5. Here the angular intensity functions are sufficiently simple in shape that a unique value of α is provided by single angle measurements such as the polarization ratio, $I_2(\theta_1)/I_1(\theta_1)$, or the dissymmetry, $I_1(\theta_1)/I_1(180^\circ - \theta_1)$. These may be plotted versus α , thereby removing the need to iterate. Other combinations can of course be used, but all share the shortcoming of not providing a unique result when α is large.

Once α has been determined, the absolute value of either $i_1(\theta)$ or $i_2(\theta)$ may be calculated; N is then a function only of the ratio of scattered to incident intensity and a number of experimental constants for a particular angle and may be easily calculated from either 2.8 or 2.9.

In general, it cannot be assumed that the scattering particles are of uniform size unless some additional test, such as the presence of higher order Tyndall spectra, or suitable theoretical argument can be made. When there is indeed a distribution of sizes present, the total scattered intensity $I_1(\theta)$ or $I_2(\theta)$ will be the sum of the contributions of all scattering particles:

$$I_1(\theta) = \frac{\lambda^2 I_{o1}}{4\pi^2 R^2} \sum_{j=1}^N i_1(\alpha_j, \theta) \quad (2.10)$$

or, if the absolute (units of no./unit volume) distribution function is written $p(\alpha)$,

$$I_1(\theta) = \frac{\lambda^2 I_{o1}}{4\pi^2 R^2} \int p(\alpha) i_1(\alpha, \theta) d\alpha \quad (2.11)$$

with the integration carried out over the range of sizes present.

There are similar expressions for $I_2(\theta)$. It would appear at this point that any number of distribution functions could be made to satisfy an experimental curve $I_1(\theta)$, thus making the problem indeterminate or at best, dependent on the appropriateness of an assumed distribution function.

The behavior of the integral in equation 2.11 will depend critically on the range of sizes encompassed by $p(\alpha)$. For example, if scattering

particles are present in the range $0 < \alpha < 1.0$ and $p(\alpha)$ is anything like a uniform distribution, the light scattered by the larger sizes will completely dominate the scattering pattern; conversely, 10^6 particles of size $\alpha = 0.1$ will have approximately the same scattered intensity as one particle of size $\alpha = 0.1$ (see Figure 2). If on the other hand, all the scattering particles are larger than $\alpha = 2-3$, the scattered intensity is no longer monotonic with increasing size and the net scattered intensity will be a complicated function of both size and $p(\alpha)$.

A number of experimental techniques have been developed for determining the particle size distribution when the scattering particles lie in the range $1.0 < \alpha < 20-25$. Kerker, Kratochvil, et.al.⁽³²⁾⁽³³⁾⁽³⁴⁾ measure the polarization ratio $I_2(\theta)/I_1(\theta)$ over a range of angles; Heller, et.al.⁽³⁵⁾ take scattering measurements at a fixed angle for varying wavelengths of incident light; Takahashi and Iwai⁽³⁶⁾ present a method which is essentially a combination of these two techniques. These techniques share the common feature that the Mie angular scattering functions in equation 2.8 and 2.9 are replaced by the integrated quantities

$$\begin{aligned} \bar{i}_1(\theta) &= \frac{\int i_1(\alpha, \theta) p(\alpha) d\alpha}{\int p(\alpha) d\alpha} \\ i_2(\theta) &= \frac{\int i_2(\alpha, \theta) p(\alpha) d\alpha}{\int p(\alpha) d\alpha} \end{aligned} \quad (2.12)$$

where $p(\alpha)$ is an arbitrarily assumed distribution function. In the above cited references, the function is chosen by physical argument and is characterized by a mean value α_{mean} and a standard deviation σ . A series of theoretical calculations are then compared with the experimental

measurements until the best fit is obtained, fixing α_{mean} and σ . The method depends on the different but known change in shape of i_1 and i_2 versus α , hence the practical lower limit of $\alpha = 1.0$.

3. Application to the present experiment

By exhibiting measureable dissymmetry, the experimental light scattering data indicated that an estimate of α could be obtained by comparison with normalized curves of $i_1(\alpha, \theta)$ and $i_2(\alpha, \theta)$ in the manner indicated above. Taking the index of refraction of pure water to be $m=1.33$ and for an incident wavelength of $\lambda = 2328\overset{\circ}{\text{A}}$ (red), α was found to lie in the range $0.3 < \alpha < 1.0$ (the actual comparison procedure is outlined in sections 2 and 3(a) of Appendix A). Since in the present case of a vapor condensing in an inert carrier the mass of condensate/unit volume is known, it is possible to check for uniformity of particle size. If uniform size is assumed, equation 2.8 or 2.9 (with the instrument calibration described in Appendix B) leads to a value of number concentration N at the already determined size α ; a value of mass/unit volume follows directly. When the values of mass concentration calculated in this manner were compared with the known values of total mass concentration, it was found that only 10-40% of the mass could be accounted for by the scattered intensity. It is therefore evident that a distribution of sizes is present. Furthermore, due to the fact that scattered light intensity increases with r^6 versus r^3 for mass, the "missing" mass must be found at sizes smaller than the above measured α . This size, which is obtained from the shape of the scattered intensity versus θ , represents a light scattering average size and will be designated by $\bar{\alpha}$.

In the usual application of light scattering theory, if particle

sizes less than $\alpha = 1.0$ are indicated and a distribution of sizes is known to be present, any number of arbitrary distribution functions can be made to satisfy the light scattering measurements. This is shown by equation 2.11. However, in the present situation where the total mass under the distribution curve is fixed, it is to be expected that there will be some reduction in the range of possible distribution functions. The extent of this reduction is investigated in what follows.

There are three constraints which must be satisfied by a given distribution of particle sizes:

(i) Normalized slope of $I_1(\theta)$ or $I_2(\theta)$; provides an estimate of the light scattering average size $\bar{\alpha}$ by direct comparison with $\int p(\alpha) i_1(\alpha, \theta) d\alpha$ or $\int p(\alpha) i_2(\alpha, \theta) d\alpha$ in the manner described above. In the present range of α , $I_1(\theta)$ and $I_2(\theta)$ give equivalent information; there is no measurable difference in the behavior of the two curves versus α .

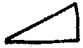

(ii) The measured ratio of scattered to incident intensity; the quantity $I_1(90^\circ)/I_{01}$ was used in the present analysis. The combination of (i) and (ii) completely characterizes the experimental light scattering pattern, for fixed incident intensity. This latter statement is due to the implied criterion that slope (or shape) of the scattering diagram is a monotonically increasing and known function of size in the range of interest, and that slope = 0 for $\alpha = 0$.

(iii) Total mass/unit volume which must be contained by the size distribution.

These constraints are not sufficient to completely determine a unique distribution curve, since a portion of the condensate mass may

by contained in particles of very small size which will not contribute significantly to the scattered light intensity. The introduction of the mass constraint, however, does impose a definite qualitative limit on the type of distribution which is possible. This will be shown by the determination of a quantitative upper limit on number average particle size.

Figure 3(a,b,c) shows the behavior of six types of distribution, all of which satisfy constraints (i) and (ii) for a particular case ($\omega_0 = .015$, P/P_0 incidence = 0.30, distance from throat = 4.5 in.) as can be seen from Figure 3(c). The distributions used are a delta function located at $\bar{\alpha}$ and the following continuous curves originating at $\alpha = .01$.

1. linear triangle 
2. linear triangle 
3. power law curve, $h \left(\frac{1}{\alpha^3} - \frac{1}{\alpha_{max}^3} \right)$
4. power law curve, $h \left(\frac{1}{\alpha^{3.6}} - \frac{1}{\alpha_{max}^{3.6}} \right)$
5. power law curve, $h \left(\frac{1}{\alpha^6} - \frac{1}{\alpha_{max}^6} \right)$

These are plotted in Figure 3(a). The corresponding mass distributions, represented as $\alpha^3 p(\alpha)$, are plotted in Figure 3(b) and the scattered intensity distributions, $I_1(90^\circ)p(\alpha)$, are plotted in Figure 3(c). The delta distribution and curves 1 \rightarrow 3 contain insufficient mass and curve 5 contains far too much mass.

It is evident from Figure 3 that for a given distribution curve, the scattered light intensity dies off with decreasing α before the number or mass distribution does. The significance is that below this point of extinction, the remaining mass may be arranged any number of

different ways without affecting the light scattering measurements. However, some estimate can be made of the maximum size at which that "missing" mass may be placed. If the α axis of Figure 3(c) is divided up so that 90% of the scattered intensity for a particular distribution shape is due to particles lying to the right of a value α and 10% is due to those lying to the left, this dividing size can serve as a coordinate roughly corresponding to a 10% experimental error in the measured value of $I_1(90^\circ)/I_{01}$. This value of α also represents the minimum size which can be accounted for by light scattering, again for a particular assumed distribution. (The error levels associated with $\bar{\alpha}$ and mass concentration are independent and are not considered here--see Chapter II.D). The fraction of total mass responsible for 90% of the scattered light is plotted versus this dividing size in Figure 4. The data points corresponding to the assumed distribution shapes in Figure 3 are indicated by the appropriate number. This figure indicates that it is possible to have all the mass contribute meaningfully to the scattered light. In this case, the dividing size becomes the minimum particle size present and is, for this example, around $\alpha = 0.2-0.25$.

Now for those distributions where only a fraction of the mass contributes to the scattered intensity, let us assume that the remaining mass is located in a delta function at a size α' chosen so that the contribution to the scattered intensity will be 10% of the total. This again corresponds to the 10% error level in $I_1(90^\circ)/I_{01}$. The calculation procedure for determining this size is given in Appendix A.3(b). The resulting placement of the additional mass is shown in Figure 5, along

with the corresponding number average size of the entire distribution for each case. As in Figure 4, the numbered points correspond to the distribution curves in Figure 3. The average size is very close to the delta function due to the very large number of particles at the size α' . The maximum possible α' , for the assumed error level of 10%, is seen to be around $\alpha = 0.25$. Thus it may be concluded, for the example in question, that regardless of the type of distribution chosen the number average particle size can be no larger than $\alpha = 0.25$ (250Å particle radius).

It may be noted that for fixed values of "missing" mass concentration and scattered light intensity, the use of a delta function provides the maximum placement of α' . If another distribution were assumed, the number average size of the "missing" mass and consequently the upper limiting number average size of the entire distribution would be lowered. It should be noted also that the only arbitrary assumption involved in the above determination of average size is the error level on $I_1(90^\circ)/I_{01}$; the value of 10% is representative of the actual experiment. Entirely similar results would be obtained with a different family of distribution curves, provided that they covered the range of from too little to too much mass concentration. For other sets of experimental data, the upper limiting number average size varied between α (or α') = 0.10 for the low mass fractions (.005) up to about $\alpha = 0.38$ for the largest mass fractions (.015).

As can be seen from Figure 3, the maximum particle size present can vary from the light scattering average size, $\bar{\alpha} = .74$, up to some

very large size depending on the particular distribution assumed. The experimentally determined value of α has the significance that there are some particles present which are at least this big. However, it is the number concentration at these larger particle sizes which is of primary interest to people working in turbine erosion, etc. This cannot be fixed as accurately as $\bar{\alpha}$, since the arrangement of particles depends on the assumed distribution; curves 1-4 in Figure 3 as well as the delta distribution at $\bar{\alpha}$ satisfy all the constraints when the appropriate delta function is added at α' , and provide a variety of concentration behavior. A rough order-of-magnitude estimate can be obtained by calculating the number concentration contained in the delta function at $\bar{\alpha}$. This typically results in a value between 10^9 - 10^{10} particles/cm³, as shown in Figure 19, compared with a total concentration predicted from the surface averaged condensation theory of 10^{13} - 10^{14} particles/cm³.

In the treatment of the full set of experimental data, the upper limiting value of average size is obtained by applying the above described "missing mass" analysis to a delta distribution located at size $\bar{\alpha}$. The calculation procedure is essentially the same as that described above (Appendix A.3(b)) with the additional calculation of the mass contained in the delta function at $\bar{\alpha}$. The difference between the average size obtained in this way and the values obtained from the other distributions (see Figure 5) is not enough to warrant calculating a similar curve for each set of experimental measurements.

Thus two of the four limits on number average and maximum particle

size are determined directly from the experimental measurements. The corresponding values of lower limiting number average size and upper limiting maximum particle size may be estimated with the assumption of a specific distribution function as follows.

The minimum particle size can be as low as zero, as far as can be determined from the light scattering measurements, but this limit is raised by the physical considerations of the condensation phenomenon. It is reasonable to assume that the particle size is no smaller than the average droplet size obtained from condensation theory (Chap. III.A).

This assumption is particularly valid when one considers the experiments of Wegener and Stein⁽¹⁹⁾⁽²⁰⁾, in which the measured particle sizes were found to be in good agreement with classical condensation theory. If such a size is taken as the lower limit in the fitting of a distribution curve to the three experimental constraints (i)-(iii), an estimate of maximum particle size is obtained which is a good representation of the maximum size present in significant concentration. A continuous, monotonically decreasing distribution function is assumed. This has physical basis in experimental distribution curves obtained in precipitation studies in metals, a theoretically analagous process. An inverse power law decay, $h \left(\frac{1}{\alpha^n} - \frac{1}{\alpha_{\max}^n} \right)$, is used in place of an exponential or other curve of infinite bound in order to simplify the numerical calculations. This type of distribution may additionally be more valid; Lifshitz and Slyozov^(36a) have shown theoretically, for precipitation from a supersaturated solid solution, that the upper size pinches off very sharply.

A calculation procedure which incorporates the above assumptions is detailed in Appendix A.3(c). Briefly, curves of $I_1(90^\circ)/I_{01}$ and the best root-mean-square fit between $I_1(\theta)$ and $\int i_1(\alpha, \theta)p(\alpha) d\alpha$ are plotted versus n and α_{\max} , the distribution parameters. α_{\min} and mass/unit volume are held fixed in the calculations. The point of intersection of the two curves determines values of α_{\max} and n , which are taken to estimate the distribution. As an argument for the validity of this approach, the calculated distribution curves were seen to steepen (Figure 6) as the measuring station was moved closer to the nucleation zone (shorter growth times).

Thus from the scattered intensity measurements and the mass concentration of condensate, it is possible to determine limiting bands for the number average and maximum particle sizes corresponding to each set of experimental data. No further information about the average size is obtainable without a reduced error level on $I_1(90^\circ)/I_{01}$. Returning to the discussion of number concentration at the larger particle sizes, it may be seen from Figure 6 that the assumption of a continuous distribution function sharply limits the concentration behavior between $\bar{\alpha}$ and α_{\max} . Since this sort of distribution function is reasonable to expect, the calculated number concentration is probably quite representative of the experiment, at least in this upper size range. The calculated concentration behavior for each set of experimental conditions may be constructed using the assumed inverse power law distribution function and the information contained in Table F.1.

C. Apparatus and Procedure

An experimental apparatus was designed and constructed for the purpose of measuring the light scattered by condensation particles at the exit plane of a supersonic nozzle. Since this work follows several previous condensation studies in the Gas Turbine Laboratory, certain pieces of equipment, such as the vapor injection system, were available and could be adapted to the present experiment. The light scattering apparatus however, had to be constructed especially for this project. The general arrangement of the various principal components is shown in Figure 7 and 8. As can be seen, the test nozzle was positioned along a vertical optical axis and angular scattering measurements were taken in

a horizontal plane of observation. The nozzle was mounted on a telescoping pipe to allow the exit plane to be adjusted relative to the light scattering equipment, thus permitting the nozzle length to be varied. A detailed description of the experimental apparatus follows.

1. Nozzle and related equipment

(a) Carrier air supply

The carrier air was provided by an oil-free, two-stage, reciprocating compressor. To achieve stable steady-flow test conditions, the receiving tank was bled to keep the compressor constantly under load. With the regulator at its maximum setting of 125 psig, the compressor was capable of supplying ~ 12 lbm/sec at 105-110 psig, thus fixing the maximum throat size of the nozzle. Other than routine filtering, no attempt was made to clean the carrier air; when the apparatus was run at reduced pressure, thus allowing the alumina dryers to be used to reduce the moisture content to a non-condensing level, there was no trace of light scattering by suspended dust particles.

Since full pressure was needed for shock-free nozzle operation, the dryers could not be used during actual condensation tests. There was no harm done, since the condensation of water vapor was being investigated, but it became necessary to accurately determine the moisture content of the carrier air. An "Alnor Dewpointer" was used for this purpose. It is a cloud chamber device which relates the dew point of the moist air to the expansion ratio at which a condensation cloud first appears. The mass fraction of water vapor was found to remain quite constant over the period of a few hours and to vary

between $\omega_o = .0015-.003$ depending on outside air conditions and cooling cooling jacket temperatures. This measurement was made at a point upstream of the injection of additional water vapor. Although it would have been useful to also check the moisture content at a point after injection, this was not done because the scale of the instrument was exceeded.

The temperature of the air leaving the compressor was on the order of 80°F; since higher temperatures were required to adjust the onset of condensation to positions downstream of the nozzle throat, a high-pressure steam heat exchanger capable of producing temperatures up to 240°F was used. The stagnation pressure and temperature, P_o and T_o , were measured at a point directly ahead of the nozzle entrance. A Statham strain-gage transducing cell No. UC3, installed in a 0-200 psi pressure fixture and connected to a model UR-4 precision readout meter was used to determine P_o . It was calibrated against a mercury manometer and was found to be both linear and stable. T_o was measured using a bare copper-constantan thermocouple connected to a Leeds-Northrup Model 8690 millivolt potentiometer with a 32°F ice reference junction. This combination was checked at the ice and steam points of water and was found to reproduce the standard values.

(b) Nozzle

In the theoretical treatment of condensation in a nozzle, the flow inside the boundary layer is assumed to be that of a perfect gas with heat addition due to the release of the heat of vaporization. It is therefore essential that the wall boundary layer be well controlled. Important factors here are a smooth entrance region and a steep negative

pressure gradient. An axisymmetric geometry provides maximum flow area versus wall surface and is desirable where angular light scattering measurements will be made. For a given air supply, these boundary layer considerations compete with the requirements that the nozzle be as long as possible and that there be shock-free flow to the exit. A final consideration is that the nozzle should be able to be fabricated using conventional methods.

A two-piece conical design was settled on, where the converging section is machined of aluminum and the diverging section is cast in plexiglass. The plexiglass section was made by grinding a steel mandrel to the specified dimensions on a center-type grinder and then embedding it in the plastic. When external machining was completed, the mandrel could be pressed out, leaving an accurately dimensioned passage. After the two pieces were clamped together, the throat area was lightly polished, providing smooth transition. Details of the nozzle construction are shown in Figures 9 and 10. Following some experimentation, a nozzle having a 0.25 in. diameter throat, 1° included cone angle and a maximum length of 12.45 in. from geometric throat to exit plane was constructed. This configuration is actually over expanded close to the shock limit for atmospheric exit pressure, resulting in some boundary layer thickening near the exit. It was found that smaller included angles were not sufficient to keep the wall boundary layers apart, causing a reduction in stagnation pressure and at the extreme a return to subsonic flow.

Twenty-three static pressure taps of .016 in. diameter were drilled as shown in Figure 9. The static pressures at these points

were measured simultaneously on a bank of 100 in. mercury-filled U-tube manometers and were recorded photographically using 4x5 in. Polaroid sheet film.

For the purpose of gas dynamics calculations, a supersonic nozzle is described by the variation of its effective flow area with distance from the throat. Here the effective flow area is defined as the geometric flow area minus the boundary layer displacement thickness. If it is assumed that the flow inside the boundary layer is a one-dimensional, isentropic expansion of a perfect gas, the following relation is obtained (from Shapiro⁽²⁶⁾) between the area ratio and the static pressure ratio:

$$\frac{A}{A^*} = \left[\frac{\gamma-1}{2} \left(\frac{2}{\gamma+1} \right)^{\frac{\gamma+1}{\gamma-1}} \right]^{\frac{1}{2}} \left(\frac{P}{P_0} \right)^{-\frac{1}{\gamma}} \left[1 - \left(\frac{P}{P_0} \right)^{\frac{\gamma-1}{\gamma}} \right]^{-\frac{1}{2}} \quad (2.13)$$

Dawson⁽¹²⁾ has shown that it may additionally be assumed, with reasonable accuracy, that the boundary layer will not be greatly affected by small changes in local temperature and pressure level. Thus the effective area ratio distribution may be determined from a single set of measurements of P/P_0 versus length along the nozzle for non-condensing flow of the carrier air. Using equation 2.13 as tabulated in the Gas Tables of Keenan and Kayes⁽³⁷⁾, with $\gamma = 1.4$ for pure air, the curve of A/A^*_{eff} shown in Figure 11 was obtained. The curve of geometric area ratio versus distance from the throat is also plotted in Figure 11. Using these two curves, the displacement thickness at the exit is calculated to be $\sim .032$ in. assuming a zero thickness at the throat.

At the higher stagnation temperatures, the plexiglass portion of the nozzle was observed to be running quite hot. This appeared to be due to conduction from the supply pipe through the aluminum converging section rather than local conduction from the boundary layer. Since plexiglass loses strength rapidly with temperatures, a 1/2 in. thick phenolic gasket and a water jacket were used as shown in Figures 9 and 10. A very low water flow was used in the cooling jacket, and there was no observable change in either the boundary layer or the condensation behavior. The cooling jacket was not used at the shortest nozzle length due to space limitations. Although precise measurements were not taken, the plastic nozzle appeared to have sufficient dimensional stability since the last data sets fell along the initially determined isentrope.

(c) Water vapor injection apparatus

To increase the carrier air moisture to the levels required in this experiment, it was necessary to inject additional water vapor. A schematic of the system used for this purpose is shown in Figure 12. Liquid distilled water is supplied under pressure from a reservoir tank, filtered, metered through a flat plate orifice, vaporized in a series of heat exchangers and then injected into the carrier air stream. A stainless steel supply tank with a capacity of about two gallons was used. The supply pressure varied between 105 and 160 psig. and was obtained from a bottle of compressed nitrogen. Two sizes of metering orifice were used, .005 and .010 in. diameter, to provide water mass fractions in the ranges $.002 < \omega_0 < .008$ and $.008 < \omega_0 < .02$ respectively. They were made by drilling the appropriately sized hole in a disc of

.005 in. steel shim stock. These were calibrated in the manner described by Dawson ⁽¹²⁾, yielding curves of \dot{m}_{water} versus $P_1 - P_2$, the pressure difference across the orifice. The pressures before and after the orifice, P_1 and P_2 , were measured with the Statham pressure transducer described above, using a network of valves to isolate the various pressures.

Before the water could be combined with the carrier air, it had to be vaporized and superheated to a point where it would not re-condense during mixing. Four heat exchangers, connected in series, were used for this purpose:

- A three foot counterflow-type exchanger, heated by 120-140 psig steam.
- A 15 foot length of 1/4 in. stainless steel tubing wound into a 6 in. diameter coil and wrapped with a 760 watt, 110 volt, electric heating tape. This combination ran at about 350-400°F.
- Two 750 watt, 220 volt, Calrod-type immersion heaters, each wound with 12 feet of 1/4 in. stainless steel tubing. The Calrod units ran at temperatures around 1600-1800°F, quite a bit above their design limit, but proved to be quite reliable.

Following established practice, bleed air was mixed with the metered liquid water to improve vaporization in the heat exchangers. The pressure drop in the carrier air heater provided sufficient bleed air for good heat exchanger performance. The superheated water vapor-bleed air mixture was injected into the two-inch diameter carrier air pipe at a point several feet upstream of the nozzle by a short length of tubing

directed against the pipe wall. Glass view ports were installed at this point, allowing a visual check for complete vaporization. Incomplete vaporization could be detected through wetting of the wall at the injection point. The series of heaters described above proved to be sufficient for water mass fraction up to $\omega_o \approx .02$.

2. Light scattering apparatus

The principal components of a light scattering apparatus are an incident light source, a transducer for measuring the scattered light, associated optical systems for collimating the incident and measured beams and in this case, since angular measurements will be made, a rotating transducer mounting to allow the angle of observation to be changed about a fixed optical axis. Before considering these items in detail, there are some general requirements which affect the overall design and operation of the apparatus.

The application of light scattering theory to this experiment is based on the assumption of a parallel monochromatic incident beam. It is also important that the incident light be quite intense, since the intensity of light scattered by a cloud of particles is several orders of magnitude below that of the incident beam. It is additionally desirable that visible light be used for ease in aligning the various components. These specifications were best met through the use of a continuous gas discharge laser, which had the further advantage of not requiring the additional collimation and filtering needed with conventional light sources.

While the incident light is monochromatic, the multiplier phototube

used to measure the scattered intensity is sensitive over a spectrum of wavelengths. This requires that some provision be made to ensure that only scattered light is being measured. This is typically done either by installing an appropriate interference filter over the face of the phototube or by excluding all outside light from the test area. In the present experiment, it was preferable that the tests be run at night for several reasons. These were the relatively long time required for a series of data runs, the fact that other equipment in the lab disturbed the light scattering apparatus, and the large amount of sound generated by the open nozzle exhaust. It was therefore decided to take the light scattering data under conditions of complete darkness and an interference filter was not used. In addition to all room lights being off, a curtained enclosure, visible in Figure 8, was built around the apparatus. Light emitted from the laser cooling slots and the reflection of the incident beam off the opposite curtain were seen to affect the measurement of the scattered signal. These sources of error were eliminated by attaching a cover to the laser (Figure 8) and by cutting a small hole in the curtain opposite the laser, allowing the incident beam to leave the enclosure.

It soon became apparent that, due to laser intensity fluctuations and the usual stability problems encountered with multiplier phototubes, there was always a certain amount of noise present in the measured signal (Becker, et. al.⁽³⁸⁾ provide a useful treatment of the sources of phototube noise). In addition, there was occasionally some short-term fluctuation in the scattered intensity arising from the condensation process itself. Thus it was desirable to use some measurement technique

which would allow the scattered intensity readings to be filtered or averaged. Compounding the problem is the fact that the flow in the nozzle must remain absolutely steady for the time required to take a full set of data, or conversely, that the light scattering data should be taken as quickly as possible. For these reasons, it was decided to continuously record the scattered light intensity versus angle of observation on an X-Y recorder, thus removing the need to carefully align the apparatus to specific angles. Once a trace of the scattered light intensity was obtained, a representative average line could be drawn and obvious anomalies could be ignored.

(a) Incident light source

A Spectra-Physics Model 130B helium-neon laser was used as the source of incident light. The operating wavelength is $6328\overset{\circ}{\text{A}}$ and the output beam is plane polarized due to Brewster's angle windows at the ends of the gas tube. Output power is specified at 0.3 mw and a beam diameter of about .082 in. was observed at the exit plane of the nozzle. A spherical resonator configuration was used, since it produces a more collimated beam. An optional confocal resonator reduces the noise level and increases the power of the output light, but at the expense of a more divergent beam.

The laser was mounted on an adjustable platform, as shown in Figure 8, to enable the incident beam to be aligned to the fixed orientation of the plane of observation. As mounted, the output beam was polarized in the vertical direction, perpendicular to the observation plane. Since it was desired to take scattered light measurements for both perpendicular

and parallel polarized incident light, a Spectra-Physics Model 310 polarization rotator was mounted on the front of the laser. Rotation of the plane of polarization is achieved by changing the orientation of a half-wave retardation plate.

(b) Multiplier phototube

An RCA type 7265 multiplier phototube was used to measure the scattered light intensity. It is a head-on type, flat face plate design, featuring 14 dynode (or amplification) stages, a focusing electrode for directing photoelectrons onto the first dynode and an accelerating electrode for minimizing space charge effects. It has very low dark current and very short time resolution capability. The semi-transparent photocathode has a multi-alkali (Sb-K-Na-Cs) composition and exhibits an S-20 spectral response curve, covering the range from about 3000 to 7500 angstroms, with the maximum response at approximately 4200\AA . The S-20 curve was the best available for use in the red end of the visible spectrum; its response at 6328\AA is about 40% of the maximum response at 4200\AA . The 7265 is capable of multiplying a small photoelectric current produced at the cathode by a median value of 9.35×10^6 times when operated at a supply voltage of 2400 volts. The output current is a linear function of the exciting illumination under normal operating conditions.

The phototube was powered by a Hewlett-Packard Model 6516A 0-3000vdc regulated power supply. A voltage divider circuit was used to supply the correct voltage to each stage of the phototube, following the schematic provided in the RCA-7265 specification bulletin⁽³⁹⁾. The

current developed by the phototube, proportional to the incident intensity, was measured in terms of the voltage across a $27K\Omega$ load resistor and was recorded on the Y scale of a Hewlett-Packard-Moseley X-Y recorder. For given experimental conditions, the supply voltage was adjusted so that the anode current never exceeded 0.25 ma., as recommended for maximum stability. The phototube was electrostatically shielded by mounting in a grounded metal housing. No attempt was made to further reduce phototube noise (dark current) with magnetic shielding or photocathode cooling.

The phototube, voltage divider elements, and the collimation system for the scattered light were all mounted in a single housing as can be seen in Figure 8. This unit was fitted to the rotating arm by means of an adjustable carriage, thereby permitting adjustment relative to the laser beam and plane of observation. The collimation system for the measurement of the scattered light has three principal elements; a circular aperture to limit the solid angle of observation, a rectangular aperture to limit the scattering volume, and a lense to focus the rectangular aperture at the axis of the rotating arm. With this geometry, the scattering volume is defined by the intersection of the laser beam and the projection of the rectangular aperture. It will be a right circular cylinder when the scattered direction is perpendicular to the incident beam. Further details and dimensions, along with the geometric calculations necessary to compare I_0 and I , the incident and scattered intensity readings, are included in Appendix B. The procedures and equipment used to align the light scattering apparatus are also described in this appendix.

(c) The rotating arm

A central pivot bearing and a rotating arm were designed to position the phototube housing, as shown in Figures 7 and 8. With this arrangement, the scattering volume could be located along an optical axis and hence would not change in focus or position as the angle of observation was varied. The bearing proved to be the critical element, since it must not only precisely determine an axis of rotation, but must be large enough to allow the nozzle to pass through its center. A tapered journal bearing was machined from 6 1/2 in. i.d. x 8 in. o.d. seamless steel tubing. Following cutting of the taper, the two pieces were lapped together, grease retention grooves were cut and a coating of graphite grease was applied to the mating surfaces. It is the design of this part which required a horizontal plane of observation.

The arm for carrying the phototube housing was constructed from a length of aluminum channel. A 20 lb. counterweight was attached to statically balance the rotating assembly about its axis of rotation, thus allowing the grease film to be loaded evenly. The lower part of the bearing was solidly mounted to the apparatus and carried four adjustment screws to align and hold the nozzle along the axis of rotation of the system. In this manner the location of the scattering volume could be fixed at any point in the nozzle exit plane.

Since continuous angular readings were to be made, a 10-turn precision potentiometer-battery combination was used to provide an electrical signal proportional to the angular position of the arm. This signal was used to drive the X-axis of the above mentioned X-Y recorder. The potentiometer was driven at a 16:1 step up ratio with a nylon-core

rubber belt fitted in a groove cut in the outside surface of the upper bearing half.

A four-way adjustable fixture for mounting density or polarization filters was installed on the rotating arm ahead of the phototube, as can be seen in Figure 8.

3. Experimental procedure

For each nozzle length used, the light scattering apparatus was aligned so that the centerline of the nozzle and the optical scattering volume coincided with the axis of rotation of the phototube. A pre-determined series of carrier moisture levels and supply temperatures was used for each nozzle length, and a full set for a given length was generally taken in one night of testing. In preparing for a set of tests, the air compressor and all heat exchangers were allowed sufficient time to reach stable operating conditions, usually about an hour. During this period the laser, phototube, high voltage power supply, and X-Y recorder were warmed up.

To record data for a particular set of operating conditions, the following operations were performed:

- The carrier air pressure and temperatures were adjusted to the desired values.
- The water mass fraction, ω_0 , of the carrier air was measured and the amount of additional water vapor required was determined.
- The water injection apparatus was adjusted to the correct mass flow rate, as measured by the pressure drop across the injection orifice.

- A period of time was allowed to check the stability of the above conditions, during which the polarization setting of the laser, the supply voltage to the phototube and the scale factor of the X-Y recorder were adjusted.
- When a recheck of P_o , T_o and ω_o indicated stable test conditions, the room lights were extinguished and the scattered light intensity was recorded. The arm holding the phototube was manually swept through the desired range of observation angles as steadily as possible. Two traces (forward and backward sweep through angular range) were taken in this manner for each of two incident polarizations, perpendicular and parallel to the plane of observation. When complete, two reference angles were marked on this recording.
- At this point, the values of P_o , T_o and the pressure drop across the injection orifice were recorded and a photograph was taken of the manometer board showing the static pressure profile in the nozzle.
- The lights were again turned off, and the light scattering measurements described above were repeated. In this manner, four traces were recorded for each polarization setting, and their average was used for the determination of particle size. A noticeable difference in the separately recorded data sets usually indicated that something had come out of adjustment, and in this case the entire process was repeated.

The actual recording of the data took on the order of three to five minutes for each set of test conditions. Incident light intensity

measurements were taken for each supply voltage and recorder scale used.

D. Interpretation of Experimental Results

1. Data reduction

Figure 13 shows typical traces of the perpendicular and parallel scattered light intensity as recorded on an X-Y recorder. Two such recordings were made for each set of test conditions, as indicated in the Experimental Procedure. These experimental curves deviate from the expected theoretical shapes due to the $1/\sin \theta$ change in the scattering volume (see Appendix B.1). Two operations are necessary before discrete points can be taken from these experimental traces for use in the estimation of particle size and number distribution. The first is to draw smooth "average" lines through the recordings. This is done by overlaying the two recordings taken at the same conditions on a light plate and visually determining the best fit. The second operation is to divide the X-axis into discrete angular intervals. This is accomplished using two index marks at 30° and 90° which were made during the recording of the data and the fact that the X-displacement is a linear function of angular positions.

With this preparation completed, the scattered intensity is measured by the height of the trace above the base line at a given angle. In this experiment, scattered intensity data were usually read over the range $40^\circ < \theta < 140^\circ$ at 5° intervals. In some cases, where the scattered intensity was low, the measurements taken at backward scattered angles were influenced by reflections of the laser "fringe" off the nozzle body. When this happened, the range of observation

was reduced to $40^\circ < \theta < 110^\circ$. For the estimation of number concentration, the measurement $I_1(90^\circ)$ was taken directly from the above data. Care was taken that the corresponding value of incident intensity, I_{01} , was recorded at the same scale setting.

The values of P_0 , T_0 , mass flow of injected water vapor, and the static pressure profile are measured directly or are obtained from the appropriate calibration chart. The mass fraction of water vapor flowing in the nozzle, defined as the ratio of water vapor to the total mass flow, is calculated by an iterative procedure as outlined in Appendix C.

2. Estimation of experimental error

The maximum accuracy to which condensation behavior can be predicted will be fixed by the uncertainty present in the measurement of the nozzle flow conditions. The pressure and temperature measurements are taken directly and are accurate to within $\pm 1\%$. The mass flow of injected vapor is determined by two pressure measurements from a calibration curve and has a similar accuracy. The calculated value of the total mass fraction, however, depends on a carrier air humidity reading obtained with a cloud-chamber-type dewpointer and the assumption of zero throat boundary layer. As a result, the uncertainty in the absolute value of ω_0 is increased to about 5-10%, with ω_0 tending to be under estimated. The error is reduced when comparisons are made between sets of experimental results, since here the throat boundary layer assumption drops out.

The technique of using various nozzle lengths to investigate

droplet growth depends for its success on the ability to reproduce a given set of experimental conditions. In practice, it proved to be quite difficult to adjust the apparatus to specified values of P_0 , T_0 and ω_0 . This was due both to oversensitive controls and to the fact that the final value of ω_0 could only be estimated as the data was being taken. Such deviation from the intended test conditions shows up in the form of varying incidence behavior, as can be seen in Figures 18 and 19.

In the present study, several size estimates are obtained from the light scattering data. The first of these, the "light scattering average" size, is obtained directly from the measured shape of the angular scattered light intensity curve. The only significant errors which arise are those associated with the drawing of an average line through a fluctuating data trace and the reading of the resulting amplitudes at discrete angles. If a number of independently drawn lines are passed through the same recording of scattered intensity, these lines will be seen to fall inside a certain band. This represents the level of discrimination of the experimental procedure. The maximum expected error, then, is determined by the upper and lower limiting values of size parameter α whose curves just fall inside this band. This procedure is complicated by the fact that the rate of change of slope of the scattered intensity curve increases with α for the size range encountered in this experiment, $0.1 < \alpha < 1.0$. At the upper end of this range, the uncertainty in α was found to be about $\pm 3\%$, while at the smallest sizes measured the error increased to about $\pm 8-10\%$.

The second size estimate obtained from the light scattering data is the upper limiting number average particle size. This value is calculated by the method outlined in section 3(b) of Appendix A. It may be seen from equation A.31 that uncertainty in the values of M' , the concentration of condensed mass (obtained from ω_o), and $\bar{\alpha}$, the light scattering average size, affects the computation. These errors have been estimated above to be about $\pm 10\%$ and $\pm 3-10\%$ respectively. In addition, the error in the measurement of $\frac{I_1(90^\circ)}{I_{01}} \cdot K$, the ratio of scattered to incident intensity, enters A.31. K is a combination of geometric factors which are constant for given experimental conditions (Appendix B.3). For this experiment, the composite error on $\frac{I_1(90^\circ)}{I_{01}} \cdot K$ is estimated to be $\pm 10\%$.

Before the individual errors can be substituted into A.31 to determine the total error in the calculated average size, an estimate must be made of the error in the term $(M' - M'_{\text{visible}})$. This may vary over a wide range. However in the present experiment, M'_{visible} was found to vary between 10-40% of M' ; therefore a conservative estimate can be obtained by assuming M'_{visible} to be half of M' . With this assumption, the maximum error in $(M' - M'_{\text{visible}})$ is given by 2·error on M' + error on M'_{visible} . If the above errors are substituted into A.31, the error level on the calculated value of average size is found to vary from $\pm 16\%$ for the larger values of $\bar{\alpha}$ to $\pm 23\%$ for the smaller sizes. Again, the relative error between sets of measurements will be lower due to the removal of several constant calibration errors.

The minimum value of number average size and the upper limiting maximum size are obtained jointly from a procedure which fits an arbitrary distribution function to the experimental measurements of scattered light intensity and condensate mass (Appendix A.3(c)). Numerical error estimates have a reduced significance because of the strong dependence on the validity of the chosen distribution function, particularly the assumed minimum size. The error due to uncertainty in the input variables alone has been determined by working out the calculation procedure for the limiting errors. The maximum expected variations in M' , $I_1(90^\circ)/I_{01}$ and $I_1(\theta)$ are found to produce a 2-3% variation in average size; this relatively mild effect is due to the fact that the vast majority of the particles are located at the small end of the distribution. The maximum size estimate was found to have about the same level of uncertainty as the upper limiting average size calculated above.

III. THEORETICAL PROGRAM

The work to be described in this section was undertaken in an attempt to establish a theoretical basis for the presence of large condensate particle sizes. This was done by applying a refined calculation technique to existing condensation theory and by examining other mechanisms which may be operating in the supersonic nozzle flow.

As has been indicated, the condensation behavior of water vapor is predicted best by the classical theory. When applied to supersonic flow in a nozzle, condensation theory has three principal parts. These are nucleation theory, which describes the spontaneous formation of stable clusters of molecules from the supersaturated vapor; droplet growth theory, by which these stable clusters increase in size; and compressible flow theory, which accounts for the effect of the released heat of vaporization on the gas flow in the nozzle. In previous applications of the theory, a surface-averaged particle size has been used to facilitate numerical calculations. In the present work, this condition is removed through a modification to the calculation procedure. By dividing the condensate up into a number of groups, different sized drops are allowed to grow at different rates. In this situation, if the average size of a particular group falls below the critical size, due to a changing stability criterion, that group will evaporate and disappear. This mechanism could thus form the basis for a spontaneous "aging" process, whereby the initial distribution tends toward a larger mean size.

When condensation occurs in a supersonic nozzle, a very large number of particles is introduced into the flowing gas. In existing

applications of condensation theory, it is commonly assumed that there is no aggregation into larger sized particles. This is found to be a valid assumption only under certain flow conditions. Two such aggregation mechanisms were investigated in the present study. The first is aggregation by Brownian Motion, in which the condensate particles come together and stick due to kinetic fluctuations. The second mechanism is aggregation by particle slip-collision, in which particles of different size lag an accelerating carrier flow by differing amounts, thus establishing a collision probability.

A. Classical Condensation Theory

The application of condensation theory to a nozzle flow has been worked out in detail by numerous investigators. Since the formulation used in the present study follows directly from these sources, a rigorous development will not be presented. The particular equations used are summarized and the general physical reasoning is indicated. Source references are included where applicable.

1. Nucleation rate

Various methods have been used to derive an expression for the classical nucleation rate. These differ somewhat in detail, but the resulting expressions share the same general form:

$$J = Z \dot{n} (4\pi r^{*2}) n \exp(-\Delta G^*/kT) \quad (3.1)$$

where:

J = no. of nuclei produced per unit volume per unit time

Z = the Zeldovich non-equilibrium factor, which varies by one or two orders of magnitude depending on the particular approximations used in deriving the equation.

\dot{n} = no. of vapor molecules impinging on unit surface area per unit time.

$(4 \pi r^{*2})$ = surface area of a critical sized cluster

n = concentration of vapor molecules

ΔG^* = free energy of formation of a critical sized nucleus

k = Boltzmann's constant

T = temperature at which the clusters form, assumed to be that of the local stream.

In the above, the growing droplet is treated as a generalized molecule in which inter-molecular forces are neglected. If it is assumed that the velocity distribution of the vapor molecules conforms to the kinetic theory of gases, the impingement rate may be written:

$$\dot{n} = \frac{p}{(2\pi m k T)^{1/2}} \quad (3.2)$$

where p is the vapor partial pressure and m is the molecular mass.

The total change in free energy is assumed to be the work of formation of the surface of the droplet plus the isothermal change in state of g^* molecules condensing from vapor to liquid:

$$\Delta G^* = 4\pi r^{*2} \sigma - g^* k T \ln \left(\frac{p}{p_{\infty}} \right) \quad (3.3)$$

where:

σ = surface tension of cluster

g^* = no. of molecules in a critical sized cluster

p_∞ = flat film saturation pressure at temperature T.

This function has a maximum value of

$$\Delta G^* = \frac{4}{3} \pi r^{*2} \sigma$$

at a size

$$r^* = \frac{2\sigma v_L}{kT \ln\left(\frac{p}{p_\infty}\right)} = \frac{2\sigma}{\rho_L R T \ln\left(\frac{p}{p_\infty}\right)} \quad (3.4)$$

where

v_L = volume per molecule of the liquid phase

R = gas constant per unit mass

ρ_L = density of liquid phase

r^* is called the critical radius, and is the most difficult size to form.

Once a droplet reaches this size, it has a 50% probability of growth.

In a steady-state nucleation process, both evaporation and condensation take place simultaneously as the cluster grows. A non-equilibrium but steady-state distribution of cluster sizes up through the critical size is postulated. The process of nucleation is then considered to be a constant net flux of nuclei through a steady distribution of cluster sizes, with the concentration of any particular size remaining fixed. An infinite supply of vapor molecules is assumed, and clusters are considered to be stable when they have reached a size of about $1.3r^*$, where the probability of further growth is approximately unity.

By using this approach, Frenkel⁽⁴⁰⁾ arrives at the following expression for nucleation rate:

$$J = \left(\frac{p}{kT}\right)^2 \frac{m}{\rho_L} \left(\frac{2\sigma}{\pi m}\right)^{1/2} \exp\left(-\frac{4\pi\sigma r^{*2}}{3kT}\right) \quad (3.5)$$

corresponding to a value of

$$Z = \left[\frac{\ln(p/p_\infty)}{6\pi g^*}\right]^{1/2}$$

in equation 3.1. Derivations by Volmer⁽⁴¹⁾, Becker and Döring⁽⁴²⁾, Zeldovich⁽⁴³⁾, Barnard⁽⁴⁴⁾, Yang⁽⁴⁵⁾ and others have resulted in similar expressions (in some cases identical) for the classical nucleation rate, differing only in the factor Z. Although the corresponding numerical values range over two orders of magnitude, the expression for nucleation rate is relatively insensitive to changes in the pre-exponential factor when applied to condensation in a nozzle. It may thus be concluded that there are no significant differences in the classical treatment of the theory.

Lothe and Pound⁽¹⁴⁾ have set forth a revised nucleation rate theory, in which the free energy of formation, as written in equation 3.2, is modified to explicitly take account of the translational and rotational motion of the droplet. When these contributions are expressed as an additional term in the summation, $-kT\ln\Gamma$, the factor Γ may be transferred into the pre-exponential. Γ is commonly referred to as the "gasification factor" and takes on a value of around 10^{17} for water vapor. However, as noted earlier, water vapor obeys the classical derivation.

For a more detailed treatment of nucleation theory, reference may be made to any of the above cited works or to Feder, Russell, Lothe and Pound⁽¹³⁾.

2. Droplet growth

In the usual nozzle condensation process, nucleation ceases before all the vapor present can condense. The nucleated clusters continue to grow by vapor impingement and reaching a size up to an order of magnitude greater than the critical radius.

The growth of a droplet depends on the rate at which condensing molecules enter its surface and on the rate at which energy is transferred between the droplet and the gaseous environment. This energy transfer is accomplished through thermal accommodation of reflected vapor and carrier molecules, and through evaporation of previously condensed molecules. In the statements to follow, the growing droplet is assumed to be spherical, stationary in space, and to be characterized by its temperature and vapor pressure, T_D and p_D . Temperature variation across the droplet is assumed to be negligible. Two accommodation coefficients are defined to describe the droplet-molecule interaction:

ξ = condensation or mass accommodation coefficient = that fraction of the impinging vapor molecules which enter the drop surface; $(1 - \xi)$ are therefore reflected.

α = thermal accommodation coefficient = the fractional temperature change which occurs in the reflected vapor and carrier gas molecules.

$$\alpha = \frac{T_R - T}{T_D - T}$$

If ξ is equal to one, only thermal accommodation with the carrier gas needs to be considered.

In the typical nozzle experiment, the critical radius is several orders of magnitude less than the mean free path; at the completion of the growth process, droplet size is usually less than one mean free path. Under such conditions, kinetic theory may be used to predict the mass and energy fluxes to and from the droplet surface. Using equation 3.2 with the above definition of ξ , the mass flux (per unit area per unit time) into the droplet is

$$\xi\beta = \xi \frac{p}{(2\pi RT)^{1/2}}$$

where p is the vapor partial pressure, T is the local stream temperature and R is the appropriate gas constant. If it is assumed that the rate of evaporation from the droplet is equivalent to the equilibrium rate of condensation at the droplet temperature and pressure, the mass flux evaporating from the droplet is

$$\xi\beta_D = \xi \frac{p_D}{(2\pi R T_D)^{1/2}}$$

p_D is the vapor pressure at the surface of a droplet of radius r , and is related to the flat-film saturation pressure by the Helmholtz equation:

$$\frac{p_D}{(p_\infty)_{T_D}} = \exp \left[\frac{2\sigma}{\rho_L R T_D r} \right] \quad (3.6)$$

The droplet growth rate may be obtained from the expression for net

mass flux:

$$\frac{dr}{dt} = \frac{\xi}{\rho_L} (\beta - \beta_D) \quad (3.7)$$

The energy flux to the droplet is $\beta \cdot KRT$, where $K = [1/(\gamma_{\text{vapor}} - 1) + 1/2]$. Of this, $\xi \beta \cdot KRT$ is added to the drop and $(1 - \xi) \beta \cdot KR[T + \alpha(T_D - T)]$ is reflected, following thermal accommodation. There will be an additional energy flux away from the droplet due to collision and thermal accommodation with the carrier gas molecules, given by $\beta_c K_c R_c \alpha_c (T_D - T)$. Here $\beta_c = P_c / (2\pi R_c T)^{1/2}$, with the subscript c indicating the appropriate values for the carrier gas. Finally, the evaporating mass flux will carry away the energy $\xi \beta_D \cdot KRT_D$. The net rate of energy flux to the droplet, found by summing the above terms, must be equal to the rate of change of its internal energy:

$$\frac{4}{3} \pi r^3 \rho_L c_L \frac{dT_D}{dt} + 4\pi r^2 \frac{dr}{dt} \rho_L U_{fD}$$

where

c_L = specific heat of the condensate

U_{fD} = internal energy at temperature T_D

$$\simeq h_{fD} = \frac{\gamma_{\text{vapor}}}{\gamma_{\text{vapor}} - 1} RT - h_{fg}$$

An order of magnitude analysis indicates that the rate of which energy must be added to change the drop temperature is negligible compared to the rate at which condensing liquid supplies latent heat. The $\frac{dT_D}{dt}$ term in the above may therefore be neglected, allowing the energy conservation equation to be reduced to the form:

$$0 = \xi K \left(1 - \frac{\beta_D T_D}{\beta T}\right) - (1 - \xi) K \alpha \left(\frac{T_D}{T} - 1\right) \quad (3.8)$$

$$- \xi \left(1 - \frac{\beta_D}{\beta}\right) \left(\frac{\gamma}{\gamma-1}\right) (1-U) - \frac{\beta_c}{\beta} K_c \alpha_c \left(\frac{T_D}{T} - 1\right) \frac{\bar{M}_{\text{vapor}}}{\bar{M}_{\text{carrier}}}$$

where

$$U = \frac{\gamma-1}{\gamma} \cdot \frac{h_{fg}}{RT}$$

\bar{M} = molecular weight

For known flow conditions, the droplet temperature and pressure may be obtained from a simultaneous solution of equations 3.6 and 3.8 if a value of the initial radius is assumed. This is commonly taken to be $1.3r^*$, the size corresponding to a growth probability of about one. Once p_D and T_D have been determined, the instantaneous growth depends on the ratio β_D/β or alternatively, on the ratio T_D/T . A growing drop is characterized by a $T_D > T$.

Since equation 3.7 cannot be evaluated for every size of drop, it is usual to calculate the growth on the basis of a surface-averaged droplet size. This type of average is considered to be appropriate in view of the impingement controlled growth mechanism.

3. Gas dynamics

Since the condensation is occurring during expansion in a supersonic nozzle, the release of the heat of vaporization causes a change in flow conditions. This heat addition is experimentally observed by the departure of the static pressure from the non-condensing isentrope.

The effect may be computed if the above nucleation rate and drop growth equations are combined with conventional gas dynamics theory, making use of the following simplifying assumptions:

1. The flow is steady, one-dimensional, inviscid, and exchanges no heat with the surroundings.
2. The vapor and carrier gas are treated as a mixture of perfect gases, the composition of which varies as the condensible component changes phase.
3. The volume of the condensate is negligible compared to its volume as a vapor, allowing it to be ignored in calculating the specific heat of the liquid-vapor-carrier mixture.
4. The boundary layer thickness (and hence the effective area distribution) is negligibly affected by small pressure and temperature changes.

Under these assumptions, the equations governing the gas dynamics are:

continuity

$$\dot{m} = \frac{\rho A u}{1-\mu} \quad (3.9)$$

conservation of momentum

$$-A dP = \dot{m} du \quad (3.10)$$

conservation of energy

$$c_p dT + u du = h_{fg} d\mu \quad (3.11)$$

where

\dot{m} = total mass flow rate = carrier + vapor + condensate

ρ = density of carrier gas-vapor mixture, approximately given by

$$\rho = P/R_{\text{mixture}} T$$

A = cross-sectional flow area

u = local stream velocity

μ = mass fraction of condensed moisture

P = local stream pressure

T = local stream temperature

c_p = specific heat (of carrier gas + vapor mixture) at constant pressure

h_{fg} = heat of vaporization of condensing vapor

By considering the condensation process with respect to variable nozzle position, rather than time, equations 3.9-3.11 may be written in terms of five variables, $P(x)$, $T(x)$, $u(x)$, $\mu(x)$ and $A(x)$. The function $A(x)$ is provided by the effective area distribution of the test nozzle, determined as indicated in Chapter II.

$\mu(x)$ may be obtained from the previously determined relations for nucleation and growth in the following manner. A nucleus of radius r_0 is assumed to form at nozzle position x_0 . At position x , it will have grown to a larger size

$$r = r_0 + \int_{x_0}^x \frac{1}{u} \frac{dr}{dt} dx$$

and its surface area will be

$$4\pi \left(r_0 + \int_{x_0}^x \frac{1}{u} \frac{dr}{dt} dx \right)^2$$

The total number of nuclei formed in a volume $A(x_0)dx_0$ is $J(x_0) A(x_0)dx_0$.

The rate at which liquid is condensed in the volume $A(x)dx$ on these nuclei is

$$\rho_L 4\pi \left(r_0 + \int_{x_0}^x \frac{1}{u} \frac{dr}{dt} dx \right)^2 J(x_0) A(x_0) dx_0 \frac{dr}{dt} \frac{dx}{u}$$

Taking account of the nucleation at x , the expression for the relative rate of formation of condensate along the nozzle is found to be

$$\frac{d\mu}{dx} = \frac{4\pi\rho_L}{\dot{m}} \left[\int_0^x \left(r_0 + \int_{x_0}^x \frac{1}{u} \frac{dr}{dt} dx \right)^2 J(x_0) A(x_0) \frac{1}{u} \frac{dr}{dt} dx_0 + \frac{1}{3} r_0^3 J(x) A(x) \right] \quad (3.12)$$

The term $\frac{dr}{dt}$ is calculated using the surface-averaged radius of the droplets at the particular cross-section.

Equations 3.9-3.12 are rewritten in the following form for use with a Runge-Kutta-Merson numerical integration procedure:

$$dY_1 = 8\pi JA \quad (3.13)$$

$$dY_2 = Y_1 \frac{dr}{dt} + r^* dY_1 \quad (3.14)$$

$$dY_3 = Y_2 \frac{dr}{dt} + JA (4\pi r^{*2}) \quad (3.15)$$

$$dY_4 = \frac{d\mu}{dx} = \frac{\rho_L}{\dot{m}} \left[Y_3 \frac{dr}{dt} + JA \left(\frac{4}{3} \pi r^{*3} \right) \right] \quad (3.16)$$

$$dY_5 = \frac{dP}{dx} = P \frac{\left[\left(\frac{h_{fg}}{c_p T} - \frac{1}{1-\mu} \right) \frac{d\mu}{dx} - \frac{1}{A} \frac{dA}{dx} \right]}{\left[1 - (1-\mu) \left(\frac{\gamma-1}{\gamma} + \frac{1}{\gamma M^2} \right) \right]} \quad (3.17)$$

$$dY_6 = \frac{dT}{dx} = T \left[\frac{(\gamma-1)(1-\mu)}{\gamma} \frac{1}{P} \frac{dP}{dx} + \frac{h_{fg}}{c_p T} \frac{d\mu}{dx} \right] \quad (3.18)$$

$$dY_7 = \frac{dM}{dx} = -M \left[\frac{1-\mu}{\gamma M^2} \frac{1}{P} \frac{dP}{dx} + \frac{1}{2T} \frac{dT}{dx} \right] \quad (3.19)$$

where M is the local Mach number, defined as

$$M = \frac{u}{(\gamma R T)^{1/2}}$$

and the quantities γ , R and c_p apply to the mixture of carrier gas and uncondensed vapor. Y_1 is the total number of droplets, Y_2 is the "total" radius and Y_3 is the "total" surface area. With these variables, a surface averaged radius is easily calculated:

$$\bar{r} = \left(\frac{2Y_3}{Y_1} \right)^{1/2}$$

When equations 3.13-3.19 are applied to a situation where a relatively large amount of condensate forms, it may become necessary to account for changes in the specific heat and molecular weight of the flow. The procedure for doing this has been presented by Dawson⁽¹²⁾.

4. Application of condensation theory

In the usual application of equations 3.13-3.19 to a condensing flow,

uncertainty in the values of Γ , σ , ξ and α exerts a large influence on the predicted results. The problem is considerably reduced in the present case of condensing water vapor, since the general behavior of this substance is well known. By comparing available data with the classical theory, Hill⁽⁵⁾⁽⁶⁾ has shown that agreement is obtained when $\alpha = 1$, $\xi = 0.04$ and σ takes on the appropriate bulk liquid value. The value of unity for α corresponds to the general agreement that there is complete thermal accommodation between a liquid and its vapor. The low value of ξ is taken from measurements made by Alty and MacKay⁽⁴⁶⁾ on water droplets evaporating into a vacuum.

The value assigned to σ is somewhat more arbitrary. There is considerable question concerning the applicability of a flat-film value of surface tension to a cluster containing 50-100 molecules, but various schemes to correct for curvature have failed to agree even on whether σ should be increased or decreased. The problem is complicated by the fact that for condensation of water vapor in an air carrier, nucleation can occur at temperatures below the triple point. Under equilibrium conditions, this would indicate that ice particles are formed, with the requirement that an additional latent heat term be included in the heat addition calculation. But in the case of water, the heat of liquefaction is small compared to the heat of vaporization with the result that the presence of supercooled liquid or solid particles cannot be differentiated in the experimental measurements. However, Duff⁽¹⁷⁾ has found for the condensation of carbon dioxide, where the two latent heats are comparable, that agreement between theory and experiment could only be obtained with the assumption of supercooled liquid drops below the triple point. On

this basis, a value of surface tension corresponding to the supercooled bulk liquid is used here (Jaeger⁽¹⁰⁾ presents an extrapolation procedure for obtaining fluid properties below the triple point).

B. Differential Growth and the Aging Phenomenon

As has been mentioned, it is usual in the application of condensation theory to consider the growth of droplets of surface-averaged size. However, if a distribution of sizes is allowed to exist, there are two possible mechanisms by which growth of the larger particles will be favored.

The first of these is based on the fact that growth rate is dependent on drop radius, as indicated by the factor r in equation 3.6 for the droplet vapor pressure. A rather small effect is expected, since the growth rate $\frac{dr}{dt}$ asymptotically approaches a constant value as droplet size increases (see Hill⁽⁵⁾⁽⁶⁾) in the free-molecule regime.

The second mechanism is expected to be more influential. As nucleation is coming to a halt, there is an abrupt increase in the size of the critical radius. The possibility arises that it will exceed the size of a portion of the growing drops, thereby causing them to evaporate. This will return vapor to the system, which can then condense on the larger drops. The net effect will thus be an increase in size of the drops at the high end of the distribution at the expense of those at the lower end.

These mechanisms were investigated theoretically by dividing the nucleating drops into a number of groups, each having a certain droplet concentration and surface averaged size. The procedure used was to

rewrite the first four of equations 3.13-3.19 for each group:

$$\begin{aligned}
 dY_{n_1} &= 8\pi JA \\
 dY_{n_2} &= Y_{n_1} \left(\frac{dr}{dt}\right)_n + r^* dY_{n_1} \\
 dY_{n_3} &= Y_{n_2} \left(\frac{dr}{dt}\right)_n + JA (4\pi r^{*2}) \\
 dY_{n_4} &= \frac{F_L}{\dot{m}} \left[Y_{n_3} \left(\frac{dr}{dt}\right)_n + JA \left(\frac{4}{3}\pi r^{*3}\right) \right] \\
 dY_{(n+1)_1} &= 8\pi JA \\
 dY_{(n+1)_2} &= Y_{(n+1)_1} \left(\frac{dr}{dt}\right)_{n+1} + r^* dY_{(n+1)_1} \\
 &\quad \text{etc}
 \end{aligned} \tag{3.20}$$

where the subscript n , $n + 1$, etc., identifies the particular group.

Equations 3.17-3.19 were applied in the same manner as before. The variable μ now represents the total moisture condensed and is determined by

$$\mu = Y_{n_4} + Y_{(n+1)_4} + Y_{(n+2)_4} + \dots$$

where the summation is carried out over all groups. The groups are initiated during the nucleation phase through the use of a dual criterion, which is experimentally determined in the following manner. A surface-averaged calculation is allowed to run to the completion of nucleation, and the time and total number of condensate particles are recorded. These values are divided by a factor N , set equal to 10 in this study, and the calculation procedure is restarted. A new group is then established whenever the elapsed time or the particle concentration of the present group exceeds the appropriate limit. By this technique, a maximum of 19 groups are possible, assuming that there is no radical

change in the nucleation behavior due to differential drop growth-evaporation. In practice, between 10-15 groups were typically obtained.

The results for the condensation of water vapor in an air carrier stream indicate that the effect is much smaller than anticipated. Two distribution curves are shown in Figure 14, representing typical results for the range of water concentrations used in this study ($.005 < \omega_0 < .015$). Typical group radius growth curves are shown in Figure 15. Note that while there was a size spread of up to a factor of 10, the vast majority of the condensed mass is located within a relatively narrow range. This may be seen from Figure 14, where the very large and very small sizes do not appear.

The absence of a significant effect is due to the behavior of the critical radius. As shown in Figure 15, r^* rises only briefly, signalling the end of nucleation, and then drops off again as the stream temperature falls. Thus whenever a group with a sufficiently large amount of condensate does fall below r^* , evaporation is quite slow. A series of runs was made with 100 times the negative growth rate, but the overall distribution was not significantly affected.

It was observed that the concentration of larger droplets increased as the point of incidence was moved down the nozzle (corresponding to a milder pressure gradient and a longer nucleation period) and as the mass fraction of water vapor was increased. Although in no case was the mass significant by itself, this behavior was found to agree qualitatively with the experiment measurements. This would suggest an influence on the operation of some other mechanism.

In the condensation of pure steam, the critical radius would be

expected to remain high following nucleation due to an essentially infinite supply of vapor. Under such conditions, the aging phenomenon should be more apparent. An application of the present calculation scheme to a typical superheated steam flow, as presented in Figure 16, shows that this is indeed the case.

C. Brownian Coagulation

With the incidence of nucleation, a large number of condensate particles are introduced into the nozzle flow. If their number is sufficiently large, there is the possibility of agglomeration arising from contact between the particles. This mechanism is usually neglected in the treatment of nozzle condensation, primarily because of the short residence times involved. To estimate the magnitude of the effect, a calculation of the coagulation due to Brownian motion (thermal fluctuation) is incorporated into the surface-averaged droplet form of condensation theory (equations 3.13-3.19).

Since the mean free path of the nozzle flow is on the order of 10^{-5} cm, versus initial droplet sizes of around 10^{-6} cm., it is appropriate to apply the collision rate obtained from kinetic theory. Following the development contained in Appendix D, the rate of change of particle concentration is expressed in the form

$$\frac{dN}{dt} = - \left(\frac{48kT}{\rho_L} \right)^{1/2} \bar{r}^{1/2} N^2 \quad (3.21)$$

where

N = particle concentration = no./unit volume

t = time

k = Boltzmann's constant

T = absolute temperature

ρ_L = droplet density

\bar{r} = surface-averaged particle size

This equation corresponds to a 100% probability that two droplets stick together on contact. If agglomeration occurs in only a fraction of the collisions, equation 3.21 is modified by multiplying dN/dt by the appropriate fraction. For each integration step in the numerical procedure for solving equations 3.13-3.14, a value of ΔN is calculated using 3.21 and the current values of \bar{r} , N , T , and Δt . N is then reduced by ΔN and the average droplet radius is increased so that the total condensed mass is conserved. The integration then proceeds to the next step with the revised variables Y_1 , Y_2 and Y_3 , where equation 3.21 is again applied.

The application of the coagulation rate for uniform particle size to the surface averaged condensation theory ignores both the initial size distribution due to a changing critical radius (Figure 14) and any tendency for a distribution to develop as Brownian coagulation progresses. This is shown in Appendix D.4 to provide an overestimate of the actual coagulation rate when working in the free-molecule regime. However, detailed application of equation D.1 to an expected distribution is not practical, particularly since a more detailed approach should also include the spontaneous distribution change mechanism described in the previous section. A full statistical treatment of the condensation phenomenon will be very complicated indeed.

In the present study, with the assumption of a 100% sticking probability, the surface-averaged particle size was found to increase by a factor of from 2.5 to 4 (depending on ω_0) for a nozzle residence time of approximately 0.5 msec. This increase is too large to be neglected, although it will decrease proportionately if the probability of sticking is reduced. In the experiments of Wegener and Stein⁽¹⁹⁾⁽²⁰⁾, the assumption of negligible Brownian coagulation is justified primarily due to the lower pressures employed. For similar values of ω_0 and T_0 , they measured droplet concentrations approximately an order of magnitude lower than expected in the present study; since Brownian coagulation is proportional to N^2 , the mechanism theoretically has 100 times smaller effect.

D. Coagulation due to Directed Motion

Due to the small size of the droplets predicted by condensation theory, it is usually assumed that there is no slip relative to the accelerating nozzle flow. However, if there is relative motion between the condensate droplets and the carrier gas, the presence of a distribution of sizes allows a particle slip-collision-coagulation mechanism to operate. By this mechanism, larger droplets would react more slowly to a change in stream velocity and be overtaken by the smaller droplets.

To investigate this probability, the calculation procedure detailed in Appendix E was applied. It was found that for the maximum velocity gradient available in the test nozzle and for the maximum expected particle size (as indicated by the light scattering measurements), there was completely negligible slip between the particles and the carrier flow.

Thus the mechanism is inoperative. An order of magnitude analysis indicates that a droplet radius of around 10 microns (10^{-3} cm.) is needed for the effect to become significant.

However, it was noticed that the average particle size increased with passage through the conical shock at the nozzle exit (increased scattered light intensity). The abrupt velocity gradient associated with the shock will make its presence felt in equation E.5 mainly through a reduction in the value of Δx . That coagulation should occur rather than droplet breakup is shown by the value of the Weber number, given by

$$We = \frac{\rho_g (u_g - u_D)^2 r_D}{\sigma_D} \quad (3.22)$$

where

ρ_g = gas density after shock

$u_g - u_D$ = velocity difference between droplet and carrier gas; taken to be the velocity gradient across the shock

r_D = droplet radius

σ_D = surface tension of liquid condensate droplet

For Weber numbers greater than approximately 10, droplet breakup is likely; in the present study, this number had a value on the order of 0.2.

There is also the possibility that high intensity turbulence is responsible for coagulation between particles of different size. Such turbulence may exist in the conical exit shock or any oblique shocks which

may be set up by the abrupt pressure rise at the incidence of nucleation. Here again, larger particles would tend to lag smaller ones in response to a velocity fluctuation. However, Crowe, Willoughby, et.al.⁽⁴⁷⁾ present the calculated result that particles as large as 1000\AA in diameter will be able to follow fluctuations of up to 20,000 cycles per second with little or no lag. Based on this conclusion and the fact that relatively few particles of this size range are expected in the condensing flow, the mechanism is presumed to have an insignificant effect.

A third mechanism for coagulation due to directed motion between droplets has been proposed by Steinberger, et. al.⁽⁴⁸⁾ in which two spheres move relative to a fluid along their common centerline. The second sphere will experience a reduced drag force and will, after a sufficient time, contact the leading sphere. This mechanism, however, cannot operate here due to the absence of relative motion between the droplets and the carrier flow.

IV. PRESENTATION AND DISCUSSION OF RESULTS

As has been indicated earlier, light scattering measurements were taken at five nozzle lengths (12.5, 10.5, 8.5, 6.5, and 4.5 in. from the throat) for several incidence conditions at each of three vapor mass fractions ($\omega_o = .005, .010$ and $.015$). For fixed values of P_o and ω_o , the point of incidence of nucleation is moved down the nozzle (to lower values of $(\frac{P}{P_o})_i$) by raising T_o .

Prior to discussing any theoretical predictions, the applicability of classical condensation theory should be checked. Figure 17 shows the incidence data obtained by estimating the point of departure of the experimental curves of P/P_o versus A/A^* from the non-condensing nozzle isentrope. Accuracy is limited by the fact that the static pressure taps were spaced 1/2 in. apart. Since a conical nozzle was used, the local expansion ratio varied with position along the nozzle. The dashed lines indicate the incidence behavior predicted by classical condensation theory for the limiting expansion ratios; the line closer to the saturation line corresponds to the minimum value of $(\frac{P}{P_o})_i$. When one considers the accuracy to which incidence could be determined from the experimental measurements, it may be concluded from Figure 17 that there is general agreement with the classical theory.

Figure 18(a,b,c) shows the limiting values of maximum and average droplet size as obtained from the light scattering measurements. The surface averaged radius predicted from classical condensation theory is also shown. The three parts (a,b,c) correspond to nominal vapor mass fractions of .005, .010 and .015 respectively. Droplet radius is

plotted against the pressure ratio at incidence, as determined from the experimental curves of P/P_0 versus A/A^* described above. The horizontal scatter reflects the experimenter's inability to exactly reproduce the flow conditions at the five nozzle lengths. $(\frac{P}{P_0})_i$ is used as the incidence parameter because it was found to clearly represent differing incidence behavior (P_0 is approximately constant for all runs). Daum and Gyarmathy⁽⁸⁾ suggest the use of the parameter $(-\frac{1}{2} \frac{dP}{dt})_i$ for this purpose; in the present study, the two parameters provide about the same spacing of incidence points. However, the factor $\frac{dP}{dt}$ depends on the local flow temperature (local flow velocity) and is therefore somewhat less universal than the simpler measurement of $(\frac{P}{P_0})_i$. If it is desired, $(-\frac{1}{2} \frac{dP}{dt})_i$ may be obtained from $(\frac{P}{P_0})_i$ and the curve of A/A^* versus distance along the nozzle (Figure 11). An attempt was made to correlate the incidence behavior using values of $(\frac{d \ln J}{dx})_i$ or $(\frac{d \ln J}{dt})_i$ calculated using equation 3.5. Aside from the fact that an arbitrary combination of experimental measurements has uncertain validity, the resulting values were found to provide poor separation of different test conditions.

For each nominal incidence point in Figure 18, the particular values of maximum and number average size corresponding to the different nozzle lengths are indicated by the set of five symbols. The lower limiting maximum size is the only purely experimental measurement, being equal to the light scattering average size $\bar{\alpha}$. The upper limiting value of number average size indicates the largest size at which the mass unaccounted for in the measurement of $\bar{\alpha}$ can be positioned and still be within the error level (10% on $I_1(90^\circ)/I_{01}$). The upper limit on maximum

size and the lower limit on number average size were obtained simultaneously by fitting an inverse power law distribution curve to the light scattering measurements and the total mass constraint, assuming the minimum size to be that predicted from surface averaged condensation theory. As has been mentioned earlier, the actual average droplet size may reside anywhere between the limits, but it is known that the concentration at maximum size will decrease as α is increased away from the lower limit $\bar{\alpha}$ (see Chapter II.B.3, Figure 3(a)). For given values of ω_0 , $(\frac{P}{P_0})_i$ and nozzle length, a size range is defined by the vertical distance between similarly shaped symbols.

From Figure 18 it may be concluded that, within the indicated limits:

1. The maximum droplet size is at least a factor of 10 larger than that predicted by the surface averaged condensation theory.
2. The number average droplet size may be as much as five times larger than predicted by surface averaged condensation theory. The lower limit on average size is 1.3 times larger than predicted by the surface averaged theory. However, this value depends strongly on the initial distribution size (assumed equal to the average droplet size predicted by surface averaged condensation theory) and is therefore somewhat arbitrary.
3. There is a general tendency for the maximum droplet size to increase as the point of incidence moves down the nozzle corresponding to a smaller pressure gradient and longer nucleation time. The opposite behavior is predicted by surface averaged condensation theory. The maximum size also increases with increasing values of ω_0 , as is predicted

by the theory.

4. Maximum size decreases slightly as the observation point is moved closer to the nucleation zone, although this effect is small compared to the difference between the maximum droplet size and the surface averaged theory. The only significant deviation shows up for $\omega_0 = .005$, low $(\frac{P}{P_0})_i$ and short nozzle length. In this case, comparison with condensation theory indicates that a portion of the vapor has not yet condensed (the nucleation zone is located in the interval 2.5-3.5 in. from the throat), making the average size estimates invalid. The fact that the maximum size remains high indicates that the growth to large sizes occurs during or very shortly after nucleation.

Figure 19 (a,b,c) compares values of droplet concentration (no./cm³) obtained from the light scattering measurements (concentration in a delta distribution at $\bar{\alpha}$) with the total concentration predicted by the surface averaged condensation theory for the same conditions as Figure 18 (a,b,c). It should be noted that there will be a general increase in concentration as the measuring station is moved closer to the throat due to the reduction in flow area (higher static pressure). This effect is shown by the increase in the total concentration obtained from the surface averaged theory; this version of condensation theory contains no mechanism for reducing the total number of droplets present in the nozzle. It should also be noted that if a continuous, monotonically decreasing, number distribution is physically called for, the concentration calculated at α can at best be only a rough estimate of the population near the maximum size limit (Figure 3(a)).

From Figure 19 it may be concluded that:

1. The number concentration in the vicinity of the maximum size is about 3-3 1/2 orders of magnitude less than the total droplet concentration predicted from surface averaged condensation theory.

2. There is a general tendency for the number concentration at maximum size to decrease as the point of incidence moves away from the throat. The points which deviate from this trend (Figure 19(a)) again correspond to $\omega_o = .005$, low $(\frac{P}{P_o})_i$ and short nozzle length and reflect the low values of $\bar{\alpha}$ shown in Figure 18(a). For these conditions, condensation theory indicates that nucleation has ceased but that there is still a significant amount of vapor present. This would seem to indicate that the larger droplets develop following nucleation but before the vapor supply is exhausted. Such a mechanism would require an unexpectedly large radius dependence in the droplet growth process but might be explained by an increasing value of ξ as the droplet grows.

Figure 20(a-j) compares experimental values of droplet size plotted versus distance from the throat with a number of theoretical predictions for each nominal vapor mass fraction and point of incidence. The data points shown are the light scattering average size and the limits of the number average size. The theoretically predicted droplet sizes are

- (i) surface averaged radius from the surface averaged theory (Chapter III.A)
- (ii) maximum group radius obtained from condensation theory with differential growth (III.B)
- (iii) surface averaged radius from the theory (i) with Brownian

coagulation applied on an average-size basis (III.C)

It may be immediately observed that the size increase due to Brownian coagulation does not become significant until some time after the incidence of nucleation. This is due to the concentration dependence of the mechanism; nucleation must be virtually complete before a sufficient concentration of droplets is present. If the ultimate concentration were an order of magnitude lower, Brownian coagulation would be negligible. It also may be observed that the maximum group size rises quickly, even though the bulk of nucleation is delayed to a point further down the nozzle. This group appears to grow quickly as long as there is vapor present. The bump in the surface average radius for incidence at lower pressure gradients reflects the changing nucleation criterion, r^* . The critical radius is large for the initially formed nuclei and then drops quickly; the average radius rises as the early droplets grow, falls as nucleation at smaller sizes overpowers the average, and rises again as nucleation ceases and the existing droplets grow.

The following conclusions may be drawn from Figures 20(a-j):

1. The theoretically predicted maximum group size is approximately two to three times larger than predicted by surface averaged condensation theory. The maximum group radius tends to be proportionately smaller at the higher values of $\left(\frac{P}{P_0}\right)_i$ where the vapor is exhausted more quickly. This mechanism, considered by itself, is unable to account for the large sizes which are measured experimentally. The theoretically predicted maximum size group typically contains about 1% of the total mass, while

the fraction of mass responsible for the scattered intensity (at $\bar{\alpha}$) is typically 10-40%. This mechanism does however provide the correct qualitative behavior, with the vast majority of the droplets located at some small size and the larger droplets contained in a rapidly diminishing tail.

2. Brownian coagulation theory applied on an average size basis (shown in Appendix D to provide an over-estimate of the effect) results in a 2.5-4 factor increase in average size. The effect is larger for points of incidence closer to the throat due primarily to the longer residence time. No conclusion can be reached concerning agreement with the experimentally determined average size due to the level of uncertainty on the upper limiting average size. Since this limit depends on the experimental error in the determination of $\frac{I_1(90^\circ)}{I_{01}}$, it would seem possible to verify the effect of Brownian coagulation by reducing this error. This is particularly true for incidence close to the throat where the theoretical prediction and limiting average size are quite close. However, it should be remembered that the upper limiting average size (equal to the maximum placement of the "missing" mass, α') is proportional to (error)^{1/3} (see Appendix A.3(b)) so that a substantial improvement is required.

3. The behavior of the experimental values of $\bar{\alpha}$ versus distance from the throat agrees qualitatively with the average size increase due to Brownian coagulation. This would indicate that the mechanism responsible for the formation of the larger droplets is likewise dependent on droplet concentration.

The fact that both the differential growth (or differential nucleation) and the Brownian coagulation mechanisms are in qualitative agreement with the measurements of maximum droplet size appears to indicate that the two mechanisms are inter-dependent and should be combined into a single calculation scheme. This is very difficult however, due to the fact that a varying distribution function is involved.

As mentioned in Chapter II.B.3, a description of concentration versus droplet size for the large end of the distribution is obtainable from the distribution curve fitted to the light scattering data and total mass constraint for each case. Even when α_{\min} , the assumed minimum size, is incorrect, the behavior at the upper end is not greatly affected. Rather than plot a series of distribution curves, the values of α_{\min} , α_{\max} , h and n which specify the distribution are tabulated in Appendix F. As far as the general behavior is concerned, the set of curves (4) in Figure 3(a,b,c) and the curves in Figure 6 are representative. In addition, the experimental values of scattered light intensity, static pressure ratio and initial flow conditions (P_o , T_o , ω_o) are tabulated.

V. CONCLUSIONS

The conclusions drawn from the present study may be divided into three groups, as follows.

A. Application of Light Scattering Theory

When the total mass concentration is known, and the maximum value of size parameter is greater than $\alpha = 0.2-0.3$, a considerable improvement is available over the usual application of light scattering theory.

First, a simple, reliable check can be made for the presence of a distribution of sizes. And second, once a distribution is known to be present, the light scattering measurements together with the total mass constraint provide distinct limits on the number average and maximum droplet sizes. One of these, the upper limit on number average size, is dependent on the experimental error associated with measuring the ratio of scattered to incident intensity.

In the present study, where the light scattering average droplet size was found to lie in the range $.01 < \alpha < 1.0$ (scattered intensity is \sim proportional to r^6), the assumption of a continuous distribution resulted in the specification of a sharply peaked, exponential-like decay from some initial size. Since only a fraction of the mass was found to be responsible for the major part of the scattered intensity, there is a region at the lower end of the distribution (roughly defined by the limits on number average size) in which, even for negligible error, the details are obscured.

Maximum droplet size was found to increase with decreasing pressure

gradient at incidence and with increasing vapor mass fraction. Droplet size was not seen to decrease proportionately as the point of observation was moved closer to the throat. The mass concentration in the vicinity of the maximum size is estimated to be between about 10 and 40% of the total, with the amount tending to be larger for increased vapor mass fraction and reduced pressure gradient at incidence. More detailed information concerning mass and number distribution is available from the inverse power law distribution which has been fitted to each set of experimental measurements.

B. Condensation Theory and Coagulation Mechanisms

A modification to the usual surface-averaged-radius formulation of classical condensation theory permitted the initiation and growth of a theoretical size distribution arising from a varying nucleation criterion and a differential growth rate. The predicted distribution is very sharply peaked, with the larger sizes being contained in a rapidly diminishing tail; the resulting number average size is virtually identical to that obtained from the surface-averaged condensation theory. Negligible coarsening, in which larger droplets are spontaneously formed, was predicted for the case of water vapor condensing in an air carrier.

An application of Brownian coagulation theory to the surface-averaged condensation theory was able to predict that average droplet size increased by a factor of between 2.5 and 4. The application on an average size basis is shown to over-estimate the effect when a distribution of sizes is present.

A mechanism for coagulation due to droplet slip-collision was

investigated and concluded to be inoperative since negligible relative motion between the droplets and the accelerating carrier flow was predicted. Due to the lack of relative motion, coagulation arising from local turbulence also appears unlikely.

C. Comparison of Theory to Experiment

The experimental measurements indicate that maximum droplet size is at least 10 times larger than predicted by the surfaced-averaged condensation theory. The number concentration in the vicinity of the maximum size is on the order of 10^9 - 10^{10} droplets/cm³ as compared with a theoretically predicted total concentration of around 10^{13} - 10^{14} droplets/cm³.

No conclusion can be made concerning the actual operation of a Brownian coagulation mechanism due to the uncertainty in the determination of number average size. There is, however, qualitative agreement between the behavior of the maximum size versus distance along the nozzle and the predicted average size increase due to Brownian coagulation. In addition, the differential growth mechanism provides a qualitatively correct distribution shape. It would therefore appear that the two mechanisms are interdependent.

The nature of this qualitative agreement, combined with the experimental observation that maximum size does not decline significantly as the nucleation zone is approached, suggests that the larger droplets are formed during the initial stages of condensation. Additionally, some of the measurements (for low vapor mass fraction, low $(\frac{P}{P_0})_i$ and short nozzle length) appear to indicate that this growth occurs following

the completion of nucleation but before the vapor supply is exhausted.

It is to be noted that these results differ from those of Wegener and Stein⁽¹⁹⁾⁽²⁰⁾, who found good agreement between predicted and measured condensate droplet size in a similar study. A possible source of this discrepancy lies in the differing experimental conditions. In particular, the present study employed a nozzle with smaller divergence angle (smaller pressure gradient) and operated at a stagnation pressure of eight atmospheres, versus one atmosphere in the earlier investigation. The increased pressure results in about an order of magnitude increase in droplet concentration, thereby allowing the theoretically predicted Brownian coagulation rate to become significant.

VI. RECOMMENDATIONS FOR FURTHER STUDY

Since it has been shown that the larger size droplets appear during the early stages of condensation, the logical next step is to examine this area in detail, with measurements being taken at much smaller increments of nozzle length right through the nucleation zone.

It is unlikely that the present uncertainty in average size can be overcome solely by reducing the experimental error. The alternative is to make the droplets look bigger by reducing the wavelength of the incident light source. However, once one leaves the visible range for the ultraviolet and below, both the equipment and the experimental techniques increase in complexity.

Shortcomings in the present formulation of condensation theory may be considered to be of two types, errors of omission and errors of incorrect application. In the first category, a more careful estimate of the effect of turbulence, a possible variation in the value of mass accommodation coefficient (ξ) or growth rate with drop radius, and the possibility of a local change in flow area due to boundary layer thickening at the onset point seem ripe for investigation. In the latter category, it is desirable to combine the treatments of differential growth and Brownian coagulation in such a way that distribution information is retained. This, however, is a difficult problem.

REFERENCES

1. Wilson, C.T.R., Phil. Trans. Royal Soc., 192A, 403, 1899.
2. Powell, C.F., Proc. Royal Soc. (London), 119A, 55, 1928.
3. Hirth, J. P. and Pound, G.M., Condensation and Evaporation in Progr. Mat. Sci., 11, 1963.
4. Stodola, A., Steam and Gas Turbines, p. 117, 1034, McGraw-Hill Book Company, Inc., New York, 1927.
5. Hill, P.G., "Homogeneous Nucleation of Supersaturated Water Vapor in Nozzles", Gas Turbine Laboratory Report No. 78, M.I.T., 1965.
6. Hill, P.G., "Condensation of Water Vapour during Supersonic Expansion in Nozzles", J. Fluid Mech., 25, 593-620, 1966.
7. Hill, P.G., Witting, H., and Demetri, E.P., "Condensation of Metal Vapors during Rapid Expansion", Trans. ASME, Ser. C., Journal of Heat Transfer, 85, 303-317, 1963.
8. Daum, F.L. and Gyarmathy, G., "Condensation of Air and Nitrogen in Hypersonic Wind Tunnels", AIAA Journal, 6, 458-465, 1968.
9. Kremmer, M., and Okurounmu, O., "Condensation of Ammonia Vapor during Rapid Expansion", Gas Turbine Laboratory Report No. 79, M.I.T., 1965.
10. Jaeger, H.L., "Condensation of Supersaturated Ammonia and Water Vapor in Supersonic Nozzles", Gas Turbine Laboratory Report No. 86, M.I.T., 1966.
11. Duff, K.M., "Non-Equilibrium Condensation of Carbon Dioxide in Supersonic Nozzles", Gas Turbine Laboratory Report No. 84, M.I.T., 1966.
12. Dawson, D.B., "Condensation of Supersaturated Organic Vapors in a

- Supersonic Nozzle", Gas Turbine Laboratory Report No. 90, M.I.T., 1967.
13. Feder, J, Russell, K.C., Lothe, J., and Pound, G.M., "Homogeneous Nucleation and Growth of Droplets in Vapors", *Adv. in Physics*, 15, 111, 1966.
 14. Lothe, J. and Pound, G.M., "Reconsideration of Nucleation Theory", *J. Chem. Phys.*, 36, 2080-2085, 1962.
 15. Reiss, H., and Katz, J.L., "Resolution of the Translation-Rotation Paradox in the Theory of Irreversible Condensation", *J. Chem. Phys.*, 46, 2496-2499, 1967.
 16. Oswatitsch, K., "Kondensationserscheinungen in Überschalldüsen", *Z. Angew. Math. u. Mech.*, 22, 1-14, 1942.
 17. Duff, K.M., and Hill, P.G., "Condensation of Carbon Dioxide in Supersonic Nozzles", Proceedings of the 1966 Heat Transfer and Fluid Mechanics Institute, Saad, M.A., and Miller, J.A., Editors, p. 268, Stanford University Press, Stanford, 1966.
 18. Thomann, H., "Determination of the Size of Ice Crystals Formed during Condensation of Water in Wind Tunnels and of their Effect on Boundary Layers", FFA Report No. 101 (The Aeronautical Research Institute of Sweden), 1964.
 19. Stein, G.D., and Wegener, P.P., "Experiments on the Number of Particles Formed by Homogeneous Nucleation in the Vapor Phase", *J. Chem. Phys.*, 46, 3685-3686, 1967.
 20. Wegener, P.P. and Stein, G.D., "Light Scattering Experiments and the Theory of Homogeneous Nucleation in Condensing Supersonic Flow", Report No. 10 prepared for contract Nonr-609(47), Department of

- Engineering and Applied Science, Yale University, March 1968.
21. Yellot, J.I., Trans. ASME, 56, 411, 1934.
 22. Yellot, J.I., and Holland, C.K., Trans. ASME, 59, 171, 1937.
 23. Lindhardt, H.D., "Potassium Condensate Droplet Size Determination",
Pub. No. U-3709, Aeronutronic Division, Philco Corporation, 1966.
 24. Winkler, E.M., "Condensation Study by Absorbtion or Scattering of
Light", High Speed Aerodynamics and Jet Propulsion, 9, (Physical
Measurements in Gas Dynamics and Combustion), 287-306, Princeton
University Press, Princeton, 1954.
 25. Durbin, E. J., "Optical Methods Involving Light Scattering for
Measuring Size and Concentration of Condensation Particles in
Supercooled Hypersonic Flow", NACA TN2441, August 1951.
 26. Shapiro, A. H., The Dynamics and Thermodynamics of Compressible
Fluid Flow, Vol. 1, The Ronald Press Company, New York, 1953.
 27. Handbook of Chemistry and Physics, 47th Edition, p. E153, The
Chemical Rubber Company, Cleveland, Ohio, 1966.
 28. Mie, G., "Bieträge zur Optik trüber Medien, speziell Kolloidaler
Metallosungen", Ann. Physik, 25, 377-445, 1908.
 29. Born, M., and Wolf, E., Principles of Optics, 3rd rev. ed., Pergamon
Press, Oxford, 1965.
 30. Erickson, W.D., "Light Scattering; A Technique for Studying Soot
in Flames", Sc.D. Thesis, Dept. of Chem. Eng., M.I.T., 1961.
 31. Lord Rayleigh, "On the Electromagnetic Theory of Light", Phil. Mag.,
12, 81-101, 1881.
 32. Kerker, M., Daby, E., Cohen, G.L., Kratochvil, J.P., and Matijevic, E.,
"Particle Size Distribution in La Mer Sulfur Sols", J. Phys. Chem.,

- 67, 2105-2111, 1963.
33. Kerker, M., Matijevic, E., Espenscheid, W.F., Farone, W.A., and Kitani, S., "Aerosol Studies by Light Scattering; I. Particle Size Distribution by Polarization Ratio Method", *J. Coll. Sci.*, 19, 213-222, 1964.
34. Wallace, T.P. and Kratochvil, J.P., "Size Distribution of Polymer Latexes from Light Scattering Measurements", *Polymer Letters*, 5, 1139-1144, 1967.
35. Heller, W., and Wallach, M.L., "Experimental Investigations on the Light Scattering of Colloidal Spheres; V. Determination of Size Distribution Curves by means of Spectra of the Scattering Ratio", *J. Phys. Chem.*, 67, 2577-2583, 1963.
36. Takahashi, K., and Iwai, S., "Estimation of Size Distribution of Small Aerosol Particles by Light Scattering Measurement", *J. Coll. Int. Sci.*, 23, 113-119, 1967.
- 36a. Lifshitz, I.M., and Slyozov, V.V., "The Kinetics of Precipitation from Supersaturated Solid Solutions", *J. Phys. Chem. Solids*, 19, 35-50, 1961.
37. Keenan, J.H., and Kaye, J., Gas Tables, John Wiley and Sons, Inc., New York, 1948.
38. Becker, H.A., Hottel, H.C., and Williams, G.C., "On the Light-Scatter Technique for the Study of Turbulence and Mixing", *J. Fluid Mech.*, 30, 259-284, 1967.
39. RCA 7265 Multiplier Phototube, Radio Corporation of America, Harrison, New Jersey; September, 1958, with revision 2, September, 1966.

40. Frenkel, J., Kinetic Theory of Liquids, ch. 7, Oxford University Press, Oxford, 1946.
41. Volmer, M., Kinetik der Phasenbildung, ch.4, Steinkopf, Dresden and Leipzig, 1939.
42. Becker, R., and Döring, W., "Kinetische Behandlung der Keimbildung in übersättigten Dämpfen", Ann. der Physik, 24, 719-752, 1935.
43. Zeldovich, J., J. Exp. Theor. Phys. (USSR), 12, 525, 1942.
44. Barnard, A.J., Proc. Royal Soc. (London), 220A, 132, 1953.
45. Yang, W.T., "A Study of Homogeneous Nucleation from Vapor to Droplets", D. Eng. Thesis, Yale University, 1963.
46. Alty, T., and MacKay, C.A., "The Accommodation Coefficient and the Evaporation Coefficient of Water", Proc. Royal Soc. (London), 149A, 104-116, 1935.
47. Crowe, C.T., Willoughby, P.G., et.al., "Dynamics of Two-Phase Flow in Rocket Nozzles", United Technology Center Report No. UTC-2102-FR, 1965.
48. Steinberger, E.H., Pruppacher, H. R., and Neiburger, M., "On the Hydrodynamics of Pairs of Spheres Falling along their Line of Centres in a Viscous Medium", J. Fluid Mech., 34, 809-819, 1968.
49. Gucker, F.T., and Cohn, S.H., "Numerical Evaluation of the Mie Scattering Functions; Table of Angular Functions π_n and τ_n of Orders 1 to 32, at 2.5° Intervals", J. Coll. Sci., 8, 550-574, 1953.
50. Penndorf, R.B., and Goldberg, B., "New Tables of Mie Scattering Functions for Spherical Particles", Geophysical Research Papers No. 45, Part 1, $m = 1.33$, Air Force Cambridge Research Center, 1956.
51. Smoluchowski, M.v., Physik.Z., 17, 557, 1916.
52. Smoluchowski, M.v., Z.Physik. Chem., 92, 129, 1917.

53. Hidy, G.M., "On the Theory of the Coagulation of Noninteracting Particles in Brownian Motion", J. Coll. Sci., 20, 123, 1965.
54. Friedlander, S.K., and Wang., C.S., "The Self-Preserving Particle Size Distribution for Coagulation by Brownian Motion", J. Coll. Int. Sci., 22, 126, 1966.
55. Hidy, G.M., and Brock, J.R., "Some Remarks about the Coagulation of Aerosol Particles by Brownian Motion", J. Coll. Sci., 20, 477, 1965.
56. Fuchs, N.A., The Mechanics of Aerosols, translated by Daisley, R.E., and Fuchs, Marina, Pergamon Press, New York, 1964.
57. Whytlaw-Gray, R., and Patterson, H.S., Smoke: A Study of Aerial Disperse Systems, Arnold, London, 1932.
58. Crowe, C.T., and Willoughby, P.G., "A Mechanism for Particle Growth in a Rocket Nozzle", AIAA Journal, 4, 1677-1678, 1966.
59. Crowe, C.T., and Willoughby, P.G., "A Study of Particle Growth in a Rocket Nozzle", AIAA Journal, 5, 1300-1304, 1967.
60. Crowe, C.T., Willoughby, P.G., et.al., "Investigation of Particle Growth and Ballistic Effects on Solid-Propellant Rockets", United Technology Center Report No. UTC-2128-QT3, 1965.

Appendix A

A.1. Formulation of the Mie angular intensity functions i_1 and i_2 for spheres of arbitrary size.

The following relationships, when combined with equations 2.1-2.3, represent the full Mie solution for the light scattered by a sphere. Using the notation of Gucker and Cohn⁽⁴⁹⁾,

$$i_1 = \left| \sum_{n=1}^{\infty} [a_n \Pi_n(\cos\theta) + b_n T_n(\cos\theta)] \right|^2 \quad (\text{A.1})$$

$$i_2 = \left| \sum_{n=1}^{\infty} [b_n \Pi_n(\cos\theta) + a_n T_n(\cos\theta)] \right|^2 \quad (\text{A.2})$$

Here a_n and b_n , called the scattering coefficients, are complex numbers and are functions only of the particle size and its index of refraction. Π_n and T_n are augmented angular functions which depend only on θ , the angle of observation.

If $\alpha = \frac{2\pi r}{\lambda}$ as before, and $\beta = m\alpha$, the scattering coefficients take the form:

$$a_n = \frac{S_n'(\beta) S_n(\alpha) - m S_n'(\alpha) S_n(\beta)}{S_n'(\beta) \phi_n(\alpha) - m \phi_n'(\alpha) S_n(\beta)} \quad (\text{A.3})$$

$$b_n = \frac{m S_n'(\beta) S_n(\alpha) - S_n'(\alpha) S_n(\beta)}{m S_n'(\beta) \phi_n(\alpha) - \phi_n'(\alpha) S_n(\beta)}$$

where m is the refractive index of the sphere relative to the surrounding medium and a prime denotes a partial derivative with respect to the argument in parentheses. S_n , C_n and ϕ_n are Riccati-Bessel functions

and are related to the ordinary Bessel functions, J_n , as follows:

$$S_n(z) = \sqrt{(\pi z/2)} J_{n+1/2}(z)$$

$$C_n(\alpha) = (-1)^n \sqrt{(\pi \alpha/2)} J_{-(n+1/2)}(\alpha) \quad (\text{A.4})$$

$$\phi_n(\alpha) = S_n(\alpha) + i C_n(\alpha)$$

where z is replaced by α or β as required in equations A.3 and $i \equiv \sqrt{-1}$.

With θ measured from the forward direction of the incident light as before, the augmented angular functions take the form:

$$\Pi_n(\cos\theta) = F(n) \pi_n(\cos\theta)$$

$$T_n(\cos\theta) = F(n) \tau_n(\cos\theta) \quad (\text{A.5})$$

where

$$F(n) = \frac{(2n+1)}{n(n+1)} \quad (\text{A.6})$$

and

$$\pi_n(\cos\theta) = P_n'(\cos\theta) \quad (\text{A.7})$$

$$\tau_n(\cos\theta) = [\cos\theta P_n'(\cos\theta) - (1 - \cos^2\theta) P_n''(\cos\theta)]$$

Here $P_n'(\cos \theta)$ and $P_n''(\cos \theta)$ are, respectively, the first and second derivatives with respect to $\cos \theta$ of the Legendre polynomial of argument $\cos \theta$ and order n .

A.2. Transformations and calculation procedures used in the evaluation of i_1 and i_2 .

Using the equations for the Mie angular intensity functions as outlined above, it is possible to calculate the theoretical scattered light intensity for any values of r , λ , m and θ . Gucker and Cohn⁽⁴⁹⁾ have developed a technique for transforming these into a form more suitable for direct computation. Beginning with the scattering coefficients, a_n and b_n (equations A.3), it is seen that the term $\phi_n(\alpha)$ is complex-valued and must therefore be separated into its real and imaginary parts for numerical evaluation. Substituting according to equation A.4, the coefficients may be rewritten:

$$a_n = \left[1 + i \frac{S_n'(\beta) C_n(\alpha) - m C_n'(\alpha) S_n(\beta)}{S_n'(\beta) S_n(\alpha) - m S_n'(\alpha) S_n(\beta)} \right]^{-1}$$

$$= [1 + i G_n(\alpha, \beta)]^{-1} \quad (\text{A.8})$$

$$b_n = \left[1 + i \frac{m S_n'(\beta) C_n(\alpha) - C_n'(\alpha) S_n(\beta)}{m S_n'(\beta) S_n(\alpha) - S_n'(\alpha) S_n(\beta)} \right]^{-1}$$

$$= [1 + i H_n(\alpha, \beta)]^{-1} \quad (\text{A.9})$$

The derivatives of the Bessel functions are eliminated by introducing the relation between the derivatives and the functions themselves:

$$\begin{aligned}\frac{S_n'(z)}{S_n(z)} &= \frac{S_{n-1}(z)}{S_n(z)} - \frac{n}{z} \\ \frac{C_n'(\alpha)}{C_n(\alpha)} &= \frac{C_{n-1}(\alpha)}{C_n(\alpha)} - \frac{n}{\alpha}\end{aligned}\tag{A.10}$$

where again z represents the argument α or β as required. Eliminating $S_n'(z)$ and $C_n'(\alpha)$ in equation A.9 yields

$$H_n(\alpha, \beta) = \frac{m R_n(\beta) C_n(\alpha) - C_{n-1}(\alpha)}{m R_n(\beta) S_n(\alpha) - S_{n-1}(\alpha)}\tag{A.11}$$

where

$$R_n(\beta) = \frac{S_{n-1}(\beta)}{S_n(\beta)}\tag{A.12}$$

Gucker and Cohn⁽⁴⁹⁾ give a recursion formula for evaluating $R_n(\beta)$ when m and hence β are complex. Further steps in the evaluation of this recursion formula are given by Erickson⁽³⁰⁾ in Appendix C of his paper. However, m is real in the present study and $R_n(\beta)$ may be evaluated directly from equation A.12 with no difficulty. Furthermore $H_n(\alpha, \beta)$ is real, allowing b_n to be easily split into its real and imaginary parts:

$$b_n = b_n^r + i b_n^i = \frac{1 + i H_n}{1 + H_n^2}\tag{A.13}$$

Thus

$$b_n^r = \frac{1}{1 + H_n^2} \quad (\text{A.14})$$

$$b_n^i = \frac{-H_n}{1 + H_n^2} \quad (\text{A.15})$$

In a similar fashion, $S_n'(z)$ and $C_n'(\alpha)$ may be eliminated from equation A.8, resulting in

$$G_n(\alpha, \beta) = \frac{W_n(\beta) C_n(\alpha) - C_{n-1}(\alpha)}{W_n(\beta) S_n(\alpha) - S_{n-1}(\alpha)} \quad (\text{A.16})$$

where

$$W_n(\beta) = \frac{1}{m} R_n(\beta) + \frac{n}{\alpha} \left(1 - \frac{1}{m^2}\right) \quad (\text{A.17})$$

Reducing a_n to its real and imaginary components yields as above

$$a_n^r = \frac{1}{1 + G_n^2} \quad (\text{A.18})$$

$$a_n^i = \frac{-G_n}{1 + G_n^2} \quad (\text{A.19})$$

The calculation of the quantities $H_n(\alpha, \beta)$ and $G_n(\alpha, \beta)$ in the above equations requires the numerical evaluation of $S_n(z)$ and $C_n(\alpha)$ from equations A.4. The required values of J_n may be obtained from tables or may be calculated directly, as was done here in the interests of increased accuracy and reduced card punching. The following Bessel

function recursion formula and initial values were used:

$$J_{n+1/2}(z) = \frac{2n-1}{z} J_{n-1/2}(z) - J_{n-3/2}(z)$$

$$J_{1/2}(z) = \sqrt{\frac{2}{\pi z}} \sin z \quad (\text{A.20})$$

$$J_{-1/2}(z) = \sqrt{\frac{2}{\pi z}} \cos z$$

To evaluate $\pi_n(\cos \theta)$ and $\tau_n(\cos \theta)$, as given by equations A.7, the recursion formulae given by Gucker and Cohn⁽⁴⁹⁾ were applied:

$$\pi_n(\cos \theta) = \frac{n}{\sin^2 \theta} [P_{n-1}(\cos \theta) - \cos \theta P_n(\cos \theta)]$$

$$\tau_n(\cos \theta) = n(n + \frac{1}{\sin^2 \theta}) P_n(\cos \theta) - \frac{\cos \theta}{\sin^2 \theta} P_{n-1}(\cos \theta) \quad (\text{A.21})$$

These, together with the general recursion formula for Legendre polynomials:

$$(n+1)P_{n+1}(\cos \theta) - (2n+1)\cos \theta P_n(\cos \theta) + n P_{n-1}(\cos \theta) = 0 \quad (\text{A.22})$$

results in the following initial values and recursion formulae from which numerical values of $\pi_n(\cos \theta)$ and $\tau_n(\cos \theta)$ may be calculated:

$$\pi_1(\cos \theta) = 1$$

$$\pi_2(\cos \theta) = 3 \cos \theta$$

$$D\pi_1(\cos \theta) = 0$$

$$D\pi_2(\cos \theta) = 3 \quad (\text{A.23})$$

$$\tau_1(\cos \theta) = \cos \theta$$

$$\tau_2(\cos \theta) = 3(2 \cos^2 \theta - 1)$$

and for $3 \leq n < \infty$,

$$\begin{aligned}\Pi_n(\cos\theta) &= \cos\theta\left(\frac{2n-1}{n-1}\right)\Pi_{n-1}(\cos\theta) - \frac{n}{n-1}\Pi_{n-2}(\cos\theta) \\ D\Pi_n(\cos\theta) &= (2n-1)\Pi_{n-1}(\cos\theta) + D\Pi_{n-2}(\cos\theta)\end{aligned}\tag{A.23}$$

cont.

$$\zeta_n(\cos\theta) = \cos\theta \Pi_n(\cos\theta) - (1 - \cos^2\theta) D\Pi_n(\cos\theta)$$

At this point, all elements appearing in the general equations for i_1 and i_2 have been reduced to a form suitable for direct computation. Since the scattering coefficients a_n and b_n contain both real and imaginary terms, it is necessary to rewrite equations A.1 and A.2 in the form:

$$\begin{aligned}i_1(\alpha, \theta) &= \left[\sum a_n^r(\alpha, \beta) \Pi_n(\cos\theta) + \sum b_n^r(\alpha, \beta) T_n(\cos\theta) \right]^2 \\ &+ \left[\sum a_n^i(\alpha, \beta) \Pi_n(\cos\theta) + \sum b_n^i(\alpha, \beta) T_n(\cos\theta) \right]^2\end{aligned}\tag{A.24}$$

$$\begin{aligned}i_2(\alpha, \theta) &= \left[\sum a_n^r(\alpha, \beta) T_n(\cos\theta) + \sum b_n^r(\alpha, \beta) \Pi_n(\cos\theta) \right]^2 \\ &+ \left[\sum a_n^i(\alpha, \beta) T_n(\cos\theta) + \sum b_n^i(\alpha, \beta) \Pi_n(\cos\theta) \right]^2\end{aligned}\tag{A.25}$$

where again $\beta = m\alpha$.

These equations form the basis of a computer subroutine which calculates the theoretical scattered light intensity for specified values of m and α at a fixed number of discrete angular intervals. Since the angular functions, $\Pi_n(\cos\theta)$ and $T_n(\cos\theta)$, are dependent only on the angle of observation, these factors are calculated for order $n=1-25$ and stored on the first pass through the subroutine. The number of terms to be included in equations A.24 and A.25 is determined

by the point at which the $(n+1)$ th term falls below some specified fraction of the n th term. The accuracy of the computation scheme was checked by comparing the calculated values with previously published results. Although no tables of $i_1(\alpha, \theta)$ and $i_2(\alpha, \theta)$ for $m=1.33$ (spherical scattering geometry) could be located, the calculated values of $r_n(\cos \theta)$ and $\tau_n(\cos \theta)$ agreed with those given by Gucker and Cohn⁽⁴⁹⁾ and the calculated values of a_n^r , a_n^i , b_n^r and b_n^i coincided with those obtained by Penndorf and Goldberg⁽⁵⁰⁾.

A.3. The estimation of particle size and size distribution

(a) Light scattering average size

An estimate of scattering particle size may be obtained from the shape (slope) of the experimental curves of scattered intensity versus angle of observation if the particle size is sufficiently large. When a distribution of sizes is present, this estimate becomes the light scattering average size, $\bar{\alpha}$. A computer program was written to compare the normalized experimental curves with corresponding families of normalized theoretical curves. An outline of its operation follows.

1. Specify discrete angles of observation at which comparison is to be made, θ_1, θ_2 , etc., by $\theta_{\min}, \theta_{\max}, \Delta\theta$. Also specify index of refraction, m , wavelength of incident light, λ , and an initial size for the iteration procedure, α_{\min} .

2. Read experimental scattered intensity measurements for perpendicular and parallel incident polarization at the above specified angles of observation:

$$I_1(\theta), I_2(\theta) \Big|_{\theta=\theta_1, \theta_2, \dots}$$

Only relative intensity measurements (with constant but unknown incident intensity) are needed for the estimation of particle size.

3. Correct $I_1(\theta)$, $I_2(\theta)$ for $1/\sin\theta$ change in scattering volume (Appendix B.1); correct for change in phototube sensitivity with incident polarization (Appendix B.2).

4. Normalize by dividing $I_1(\theta)$, $I_2(\theta)$ by $I_1(90^\circ)$.

5. For the specified values of α_{\min} and angular range θ_1 , θ_2 , etc., calculate the theoretical scattered intensities $i_1(\alpha_{\min}, \theta)$, $i_2(\alpha_{\min}, \theta)$ $\Big|_{\theta=\theta_1, \theta_2, \dots}$ in the manner indicated in section A.2. Normalize by dividing through by $i_1(\alpha_{\min}, 90^\circ)$.

6. Calculate the root-mean-square deviation between $I_1(\theta)$ and $i_1(\alpha_{\min}, \theta)$ and between $I_2(\theta)$ and $i_2(\alpha_{\min}, \theta)$ using the relation

$$\begin{aligned} \text{rms}_1 = & \left\{ \left[I_1'(\theta_1) - i_1'(\alpha_{\min}, \theta_1) \right]^2 \right. \\ & \left. + \left[I_1'(\theta_2) - i_1'(\alpha_{\min}, \theta_2) \right]^2 + \dots \right\}^{1/2} \end{aligned} \quad (\text{A.26})$$

and similarly for rms_2 . Primes denote the normalized values.

7. Change α_{\min} by progressively smaller intervals, returning to steps 5 and 6 for each value of α , until the root-mean-square deviation for the perpendicular component, rms_1 , is minimized. The iteration continues until a specified minimum step size is reached, with the final value of α being taken as the "best fit" between theory and

experiment.

The iteration is performed only on rms_1 , although rms_2 is calculated for each step. This is due to the fact that in some cases, especially where the scattered intensities were low (low condensate mass fractions), the best fit for $I_1(\theta)$ and $I_2(\theta)$ occurred at different values of α . It was decided to use only the perpendicular component $I_1(\theta)$ to estimate the light scattering average size since it is of higher intensity than the corresponding parallel component, thereby being less influenced by stray light and phototube noise. This is particularly true in the region around 90° , as is shown by Figure 21. The determination of rms_2 then serves as a check on the result obtained from the minimum value of rms_1 .

(b) Upper limiting average size for a delta distribution at $\bar{\alpha}$.

A value of the mass contained in a delta distribution located at size $\bar{\alpha}$ (estimated in (a) above) may be calculated directly from equation 2.8 and the experimental measurement of $I_1(90^\circ)/I_{01}$ = ratio of scattered to incident intensity.

$$N_{\text{visible}} = \frac{I_1(90^\circ)}{I_{01}} \cdot \frac{1}{i_1(\bar{\alpha}, 90^\circ)} \cdot K \quad (\text{A.27})$$

where

$$N_{\text{visible}} = \text{particle concentration at } \bar{\alpha} \text{ responsible for} \\ \text{scattered intensity} = \text{no./cm}^3$$

K = a combination of geometric factors which are constant for a given scattering geometry (Appendix B.3)

$$M'_{\text{visible}} = N_{\text{visible}} \cdot \frac{\lambda^3 \bar{\alpha}^3}{6\pi^2} \quad (\text{A.28})$$

where

$$M'_{\text{visible}} = \text{mass concentration responsible for scattered intensity} = \text{gm/cm}^3$$

Therefore the mass not accounted for by the scattered light is $(M' - M'_{\text{visible}})$, where M' is the experimental value of total mass of condensate in gm/cm^3 . If this value is determined in some other way, as was the case for the five non-delta distributions in chapter II.B, the computation scheme is entered at this point.

Let the size α' correspond to the placement of a delta function containing mass $(M' - M'_{\text{visible}})$. This "missing" mass is located in such a way that its total scattered intensity is equal to the error level on $I_1(90^\circ)/I_{01}$, in this case 10%. Thus the number concentration in the delta function at α' is given by

$$N_{\text{delta}} = (.10) \cdot \frac{I_1(90^\circ)}{I_{01}} \cdot \frac{1}{i_1(\alpha', 90^\circ)} \cdot K \quad (\text{A.29})$$

and by

$$N_{\text{delta}} = \frac{6(M' - M'_{\text{visible}}) \pi^2}{\lambda^3 \alpha'^3} \quad (\text{A.30})$$

where $I_1(90^\circ)/I_{01}$ is the ratio of scattered to incident intensity which appears in equation A.27. A.29 and A.30 may be equated, yielding the result

$$\frac{\alpha'^3}{i_1(\alpha', 90^\circ)} = \frac{6(M' - M'_{\text{visible}}) \pi^2 I_{01}}{\lambda^3 (.10) I_1(90^\circ) K} \quad (\text{A.31})$$

All factors appearing in the right side of A.31 are known; therefore α may be obtained from a plot of $\alpha^3/i_1(\alpha, 90^\circ)$ versus α .

With α' , N_{delta} may be calculated from A.29 and the number average size may be easily determined. In the present study, N_{delta} was always about two orders of magnitude greater than N_{visible} . When this is the case, α' is a good estimate of the upper limiting number average size. As can be seen from equation A.31, α' will depend on the assumed error level; since $i_1(\alpha, 90^\circ)$ varies approximately as α^6 for the present size range, α' will change with (error level)^{1/3}.

(c) Particle size distribution

As described in Chapter II.B.3, an estimate of the number average and maximum particle sizes is obtained by fitting an arbitrarily chosen inverse power law distribution curve to the experimental light scattering and total mass measurements. A family of absolute distribution functions (units of number of particles/cm³) of the form:

$$p(\alpha) = h \left(\frac{1}{\alpha^n} - \frac{1}{\alpha_{\text{max}}^n} \right) \quad (\text{A.32})$$

is assumed. With the addition of a minimum size limit, the distribution is specified by values of the exponent n and the maximum size α_{max} . The advantage of this type of distribution, as compared to an exponential or Gaussian function, is that it may be mathematically integrated within

finite limits.

Particular values of n and α_{\max} are determined when the following three equations are simultaneously satisfied.

M' = experimental value of total mass of condensate = mass/cm³

$$M' = \frac{\rho \lambda^3}{6\pi^2} \int \alpha^3 p(\alpha) d\alpha \quad (\text{A.33})$$

$I_1'(\theta)|_{\theta=\theta_1, \theta_2, \text{etc.}}$ = normalized curve of scattered intensity versus angle of observation.

$$I_1'(\theta) = \frac{\int i_1(\alpha, \theta) p(\alpha) d\alpha}{\int i_1(\alpha, 90^\circ) p(\alpha) d\alpha} \Big|_{\theta = \theta_1, \theta_2, \dots} \quad (\text{A.34})$$

$I_1(90^\circ)/I_{01}$ = measured ratio of scattered to incident intensity

$$\frac{I_1(90^\circ)}{I_{01}} = K \int i_1(\alpha, 90^\circ) p(\alpha) d\alpha \quad (\text{A.35})$$

where K is as defined in A.3(b) above.

A computer program was written to perform the calculations indicated by equations A.33-A.35 for a series of values of n and α_{\max} . An outline of the procedure follows.

1. Specify values of m , λ and angular range as in program (a). Specify a value of α_{\min} = starting point for the family of distribution curves to be generated.
2. Read experimental values of M' (total mass/cm³) and I_{01} (incident intensity); read values of $I_1(\theta)$ as in program (a).
3. Normalize $I_1(\theta)$; correct for $1/\sin \theta$.
4. Calculate and print $I_1(90^\circ)/I_{01}|_{\text{experimental}}$.

5. Calculate an array of $i_1(\alpha, \theta)$ for the specified angular intervals and a specified range of size parameter, $\alpha_{\min}, \alpha_{\max}, \Delta\alpha$.

6. Calculate the corresponding array of the integrated quantities:

$$\text{INTI}(\alpha, \theta) = \int_{\alpha_{\min}}^{\alpha} i_1(\alpha, \theta) d\alpha$$

using a procedure for numerical integration. By interpolating within this table, the integrals in equations A.34 and A.35 may be evaluated for any α without further recourse to numerical techniques.

7. Set up a two-dimensional array, $n_{\min}, n_{\max}, \Delta n; \alpha_{\max \min}, \alpha_{\max \max}, \Delta\alpha_{\max}$.

8. Proceed through the n, α_{\max} lattice point by point, making the following computations for each set of values of n and α_{\max} :

- determine h in equation A.32 by satisfying equation A.33.

- with h , calculate $I_1(90^\circ)/I_{01}|_{\text{theor.}}$ from equation A.35.

- with h , calculate $I_1'(\theta)|_{\text{theor.}}$ from equation A.34;

calculate rms_1 between $I_1'(\theta)|_{\text{theor.}}$ and $I_1'(\theta)|_{\text{exp.}}$ in the manner indicated in program (a).

- calculate the number average size for the distribution n, α_{\max} .

9. Set up an output array with coordinates n, α_{\max} ; at each lattice point n, α_{\max} print the values of $I_1(90^\circ)/I_{01}|_{\text{theor.}}$, rms_1 and average size obtained in step 8.

Two curves are then drawn by hand on the printed n, α_{\max} array:

- those values of n, α_{\max} which obey the mass constraint and which satisfy the condition

$$\frac{I_1(90^\circ)}{I_{01}} \Big|_{\text{theor.}} = \frac{I_1(90^\circ)}{I_{01}} \Big|_{\text{exp.}}$$

- those values of n , α_{\max} which obey the mass constraint and which best fit the shape of the scattered intensity versus angle curve (rms_1 is minimized). If one is sufficiently clever in choosing the n and α_{\max} ranges, the two curves will intersect. The coordinates of the point of intersection, along with the assumed value of α_{\min} , fixes the distribution which fits the experimental data.

A number of cases were checked by hand calculation to insure that the program was working properly.

Appendix B

B.1. Scattering geometry

A schematic of the scattering geometry is shown in Figure 22(a), looking down the vertical axis of rotation. This arrangement results in a cylindrical scattering volume, as shown in Figure 22(b). Here h and w are the dimensions of the rectangular aperture when projected to the system axis. As can be seen, the scattering volume is a right circular cylinder when the angle of observation is 90° , but is a cylindrical prism at other angles. Since the dimension w does not change with angle, the scattering volume has a minimum size at 90° and increases with $1/\sin \theta$ as the angle moves away from 90° . Thus it is necessary to correct the scattered intensity measurements to a uniform scattering volume by multiplying by the appropriate value of $\sin \theta$.

The dimensions of the optical system used to measure the scattered and incident light intensity are given in Figure 23. The solid angle limiting aperture fixes the divergence of the measured scattered signal; its size is a compromise between resolution of detail and signal intensity. The present 0.186 in. diameter aperture corresponds to a plane divergence angle of 0.7° . A rectangular aperture, formed by two crossed slits, is positioned ahead of the phototube. It determines the length of the cylindrical scattering volume and together with the lens and solid angle aperture, fixes its location at the system axis of rotation. The height of the rectangular aperture is .025 in., resulting in a maximum scattering volume height of .098 in. (dimension h in Figure 22 (b)). This is somewhat larger than the laser beam diameter of .082 in.,

thus allowing the vertical position of the phototube to vary slightly without altering the scattering geometry. The width of the rectangular aperture is .005 in., producing a scattering volume width of .020 in. (dimension w in Figure 22(b)). A larger value results in a greater measured intensity, but at the same time averages out any local variations. In the present experiment, the maximum aperture width was limited by the necessity that the scattering volume fit inside the conical supersonic test region at low angles of observation. Since only one wavelength of light was to be used in this experiment, a simple plano-convex lens was used to focus the rectangular aperture at the system axis. Two .20 in. light stops were installed as shown to prevent outside light from reaching the photocathode via internal reflection.

B.2. Photomultiplier calibration

Although no absolute intensity measurements were taken, it was necessary to compare relative measurements taken at differing polarizations both with each other and with the corresponding measurements of incident intensity. The photocathode surface of the phototube was found to exhibit a different sensitivity for the two incident polarizations used. For a fixed level of incident intensity, the ratio of response for perpendicular and parallel incident polarization was measured to be $I_{\perp}/I_{\parallel} = 0.9387$. Thus in order to compare the experimental measurements of perpendicular and parallel scattered light, the parallel readings must be multiplied by this factor.

No filters were used when taking actual scattering data, but it was necessary to reduce the laser intensity in order to measure the level of incident light. This was done with three no. 6 glass density

filters of the type used in welding face masks, mounted at the location indicated in Figure 23. The calibration process involved the finding and marking of a suitably sized area where the attenuation was uniform, and care was taken to use this area when recording intensity measurements. The filters proved to be only negligibly dependent on incident polarization and very stable over a period of time.

B.3. The comparison of scattered to incident intensity

In the present experiment, an integrated form of the general Mie light scattering equations,

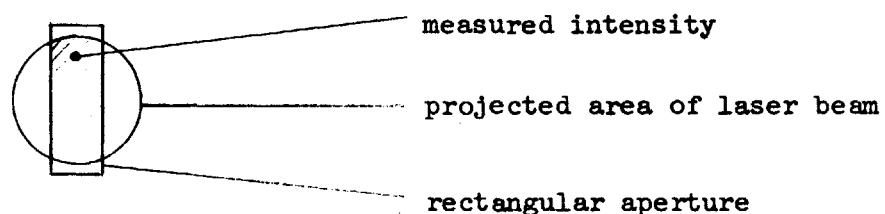
$$\int p(\alpha) i_1(\alpha, 90^\circ) d\alpha = \frac{I_1(90^\circ)}{I_{01}} \cdot \frac{4\pi^2 R^2}{\lambda^2} \quad (\text{B.1})$$

has been applied as part of a scheme for estimating the condensate particle size and number distribution. $p(\alpha)$ is the absolute size distribution, with units of number/unit volume. $I_1(90^\circ)$ and I_{01} are experimental values of the scattered intensity at 90° and the incident intensity, both for perpendicular polarization. They are measured in terms of the voltage drop across a load resistor for a given phototube supply voltage, and will be represented as $e_1(90)$ and e_{01} respectively. Before these relative measurements can be used, they must be expressed in terms of intensity/unit area, as determined from the dimensions shown in Figure 23. This comparison is made at the plane of the limiting aperture, whose distance from the scattering volume enters equation B.1 as R .

For the case of the scattered intensity, $I_1(90)$ is simply the measured signal divided by the area of the limiting aperture:

$$I_1(90^\circ) = \frac{e_1(90)}{\frac{\pi(.186)^2}{4}} = 36.8 \cdot e_1(90) \text{ mv/in}^2 \quad (\text{B.2})$$

The laser beam is of circular cross section with a diameter of .082 in. It would therefore easily pass through the solid angle aperture but, since it was parallel rather than emanating from a point source in the scattering volume, would focus at a point ahead of the rectangular aperture and be truncated by it.



$$A_2 = \text{measured intensity} = (.005)(.0198)$$

$$A_1 = \text{projected area of laser beam} = \frac{\pi}{4} (.0198)^2$$

$$\frac{A_1}{A_2} = 3.08$$

Thus, if f is the filter attenuation when measuring the incident intensity,

$$I_{o1} = e_{o1} \frac{\frac{1}{f_1} \cdot \frac{1}{f_2} \cdot \frac{1}{f_3} \cdot \frac{A_1}{A_2}}{\text{area of laser beam}}$$

$$I_{o_1} = e_{o_1} \frac{(460)(460)(460)(3.08)}{\frac{\pi}{4} (.082)^2}$$

$$= 5.68 \times 10^{10} \cdot e_{o_1} \quad \text{mv/in}^2 \quad (\text{B.3})$$

If equations B.2 and B.3 are inserted in equation B.1, the value of the left-hand side is expressed in terms of the total number of particles in the scattering volume. To normalize this to number/cubic centimeter, the right-hand side of B.1 must be divided by the actual size of the scattering volume.

For an angle of observation of 90° , the scattering volume is the cross-sectional area of the laser beam times the projected width of the rectangular aperture, resulting in a value of $.00170 \text{ cm}^3$. For the present case where:

$$R = 38.23 \text{ cm}$$

$$\frac{2\pi}{\lambda} = 9.93 \times 10^4 \text{ cm}^{-1}$$

and equation B.1 thus reduces to the form:

$$\int -p(\alpha) i_1(\alpha, 90^\circ) d\alpha = 5.50 \times 10^6 \frac{e_1(90)}{e_{o_1}} \quad (\text{B.4})$$

B.4. Alignment procedures

Before light scattering data can be taken, the apparatus must be optically aligned so as to define a plane of observation, perpendicular and parallel polarization directions, and a fixed scattering volume size and location. The following steps constitute the alignment procedure

used with this apparatus.

- The laser mounting bed is adjusted until the incident beam is perpendicular to the system axis, using plexiglass height gauges at each end of the rotating arm. The target shown in Figure 24(a) is then installed in the nozzle exit and the laser is adjusted vertically until the beam is about .020-.030 in. above the exit plane of the nozzle. This allows for thermal expansion of the nozzle and supporting pipe. With this accomplished, the laser beam is adjusted in the plane of observation until it passes through the axis of rotation, as determined by the location of a circular light spot on the target (Figure 24(b)).

- At this point, the phototube is removed from its housing, the target is removed from the nozzle exit, and the rotating arm is positioned to allow the laser beam to enter the phototube housing. The lens is in position but the rectangular aperture is removed. A cross-hair jig, made by scribing and inking two perpendicular lines in a plexiglass disc, is fitted to each end of the housing. The phototube housing is then aligned to the laser beam by centering the rear cross in the shadow formed by the front one, as shown in Figure 25(a). The adjustable angle pointer is set to read 0° on the fixed protractor.

- With this accomplished, the front cross-hair jig is removed and the slits forming the rectangular aperture are installed. The two slits are adjusted until a rectangle of light is centered on the rear cross (Figure 25(b)). The fact that the incident light is coherent gives rise to a series of diffraction lines which are useful in fixing the orientation of the aperture.

- The front cross-hair jig is now removed and the nozzle target is

re-installed. A slide projector is set up behind the rectangular aperture in the position normally occupied by the phototube. An image of the rectangular aperture is thus projected on the target, allowing the focus and the position of the aperture to be checked. The correct position of this image is indicated by the dashed lines in Figure 24(b). This check is repeated at several angles.

- With these operations successfully completed, the target is again removed and the phototube is installed and sealed in its housing. The rotating arm is returned to the zero angle position and three density filters are installed in the filter holder. A piece of polarizing sheet is also installed with a known orientation, and the setting of the polarization rotator is checked. Once this has been accomplished, the filters are removed and the apparatus is ready for use.

Appendix C

Calculation Procedure for Vapor Mass Fraction

The mass fraction of water vapor present in the carrier air stream is defined as

$$\omega_o = \frac{\dot{m}_{\text{vapor}}}{\dot{m}_{\text{mixture}}} = \frac{\dot{m}_{\text{vapor}}}{\dot{m}_{\text{vapor}} + \dot{m}_{\text{carrier}}}$$

In the present case, where the carrier air has an initial moisture level ω_{oi} , this equation takes the form

$$\omega_o = \omega_{oi} + \frac{\dot{m}_{\text{vapor, injected}}}{\dot{m}_{\text{vapor, total}} + \dot{m}_{\text{carrier}}} \quad (\text{C.1})$$

where $\dot{m}_{\text{vapor, injected}}$ and ω_{oi} are experimentally determined quantities.

For a choked nozzle, the mass flow rate may be calculated from the perfect-gas, isentropic flow relation

$$\dot{m} = \frac{A^* P_o}{\sqrt{T_o}} \sqrt{\frac{\gamma}{\bar{R}/\bar{M}} \left(\frac{2}{\gamma+1} \right)^{\frac{\gamma+1}{\gamma-1}}}$$

where

\bar{R} = universal gas constant

\bar{M} = molecular weight

γ = ratio of specific heats

In the case of pure air flow, $\gamma=1.4$ and $\bar{M}=29$, this equation reduces to the form (Shapiro⁽²⁶⁾):

$$\dot{m} = 0.532 \frac{A^* P_0}{\sqrt{T_0}}$$

with A^* in in^2 , P_0 in lb/in^2 and T_0 in $^\circ\text{R}$. The presence of water vapor will affect the mass flow by altering the net values of \bar{M} and r .

$$\bar{M}_{\text{mixture}} = y_0 \bar{M}_{\text{vapor}} + (1 - y_0) \bar{M}_{\text{carrier}} \quad (\text{C.2})$$

$$y_0 = \omega_c \left(\frac{\bar{M}_{\text{mixture}}}{\bar{M}_{\text{vapor}}} \right) \quad (\text{C.3})$$

$$y_{\text{mixture}} = \frac{y_0 \left(\frac{\gamma_{\text{vapor}}}{\gamma_{\text{vapor}} - 1} \right) + (1 - y_0) \left(\frac{\gamma_{\text{carrier}}}{\gamma_{\text{carrier}} - 1} \right)}{y_0 \left(\frac{1}{\gamma_{\text{vapor}} - 1} \right) + (1 - y_0) \left(\frac{1}{\gamma_{\text{carrier}} - 1} \right)}$$

where y_0 is the mole fraction of water vapor present in the mixture. Since γ for water vapor is 1.32, close to the value for air, and since y_0 is very small, variation in y_{mixture} may be neglected. Thus the total mass flow may be written:

$$\dot{m}_{\text{mixture}} = 0.532 \sqrt{\frac{\bar{M}_{\text{mixture}}}{29}} \cdot \frac{A^* P_0}{\sqrt{T_0}} \quad (\text{C.4})$$

The value of A^* is calculated from the geometric throat diameter of .250 in., with no correction being made for displacement thickness. Calculations by Duff⁽¹¹⁾ showed that this assumption results in about a 5-10% underestimate of ω_0 , which is relatively unimportant as far as condensation behavior is concerned. Likewise, the error from this source in the determination of average particle size is small compared to other uncertainties that arise.

An iterative procedure, combining equations C.1 - C.4, was used

to determine ω_0 . \bar{M}_{mixture} was initially set equal to \bar{M}_{carrier} (=29) to get a first approximation of \dot{m}_{mixture} , ω_0 and y_0 . This value of y_0 was used to calculate a new value of \bar{M}_{mixture} and subsequently a new value of \dot{m}_{mixture} , etc., until the values of ω_0 converged. This typically occurred after two or three cycles.

To calculate values of p_i , the local vapor pressure at incidence, and T_i from the observed value of $(P/P_0)_i$, the following equations were used with the iterated value of y_0 :

$$p_i = y_0 \left(\frac{P}{P_0} \right)_i P_0$$

$$T_i = T_0 \left(\frac{T}{T_0} \right)_i = T_0 \left(\frac{P}{P_0} \right)_i^{\frac{\gamma_{\text{mixture}} - 1}{\gamma_{\text{mixture}}}}$$

Appendix D

Brownian Coagulation

According to the model for Brownian (or thermal) coagulation, aerosol particles collide with one another due to Brownian motion and, in a certain fraction of these collisions, stick together. This mechanism causes a reduction in the number of particles present with a corresponding increase in particle size. For the case where a constant probability of sticking is assumed, the problem of estimating the coagulation rate reduces to that of determining an expression for the collision frequency between particles.

In his classical work on this subject, Smoluchowski⁽⁵¹⁾⁽⁵²⁾ derives the following discrete formulation for the rate of concentration change:

$$\frac{d}{dt} (N_k) = \frac{1}{2} \sum_{\substack{j=1 \\ i=k-j}}^{i=k-1} L_{ij} - \sum_{j=1}^{\infty} L_{kj} \quad (D.1)$$

where

N_k = no./unit volume of the kth sized particles

L_{ij} = collision frequency between ith and jth sized particles

Expressions are developed for a discontinuous distribution of particle concentration in various sizes; i.e., there is an equation of the form (D.1) for each particle size. Particles of a particular size are considered to be aggregates consisting of i, j, or k multiples of a unit size. In treating the general case of Brownian coagulation, one is faced with the problem of simultaneously solving a very large number of

the above differential equations. An alternative approach is to approximate the discontinuous distribution by a continuous function. The use of similarity theory permits analytic solution of the resulting integro-differential equation, but only for elementary boundary and initial conditions. Both approaches have been successfully applied to Brownian coagulation in a continuum, where collision frequency is independent of particle size. Hidy⁽⁵³⁾ numerically handled the discrete case and Friedlander and Wang⁽⁵⁴⁾ have treated the continuous case. Both are in essential agreement that a self-preserving size distribution is attained after a suitable time.

In deriving expressions for the collision frequency, the following assumptions are made:

- Encounters between two particles are of primary importance.
- The probability of sticking upon collision is unity.
- The coagulating particles are spherical and are distributed at random in a space larger compared to their total volume.
- The carrier fluid is either stagnant or in uniform motion.
- The only source of relative motion between coagulating particles is that due to thermal (Brownian) fluctuation. Other sources of relative motion such as laminar shearing flow, turbulence and inter-particle forces (potential fields, electric charges, etc.) are all absent.
- There is no addition or removal of mass.

D.1. Collision frequency by continuum theory

The expressions to follow, combined with equation (D.1), comprise the classical Brownian coagulation theory due to Smoluchowski⁽⁵¹⁾⁽⁵²⁾.

In the continuum regime ($Kn \equiv$ particle Knudsen number $\equiv \lambda/r \equiv$ mean free path of carrier fluid/particle radius $= 0$), Fick's law of diffusion is assumed to apply. The flux of aerosol particles to the surface of a given particle is calculated by assuming the particle surfaces to be at zero concentration. This assumption requires that two colliding particles always adhere. Following the presentation by Hidy and Brock⁽⁵⁵⁾, the collision rate for the i th and j th species can be written:

$$L_{ij}^{(c)} = 4\pi M_{ij} D_{ij} R_{ij} N_i N_j \quad (D.2)$$

where

$$M_{ij} = \text{symmetry number}; \quad \begin{array}{ll} M_{ij} = 1/2 & i=j \\ M_{ij} = 1 & i \neq j \end{array}$$

$$D_{ij} = \text{net diffusivity} = (D_i + D_j)$$

$$R_{ij} = \text{collision cross section} = (r_i + r_j)$$

$$N_i, N_j = \text{no./unit volume of } i\text{th, } j\text{th species, respectively.}$$

The diffusivity is given by the Stokes-Einstein relation:

$$D_i = \frac{kT}{6\pi\mu r_i}$$

where

k = Boltzmann's constant

T = absolute temperature

μ = viscosity of carrier fluid

r_i = particle radius

For the case of a homogeneous aerosol where $r_i = r_j$, the collision frequency reduces to:

$$L_{ii}^{(c)} = \frac{4kTN_i^2}{3\mu} \quad (D.3)$$

The lack of any dependence on particle size is of interest; even when a distribution of sizes is present, only the width of the distribution is important (see equation D.10). The combination of equations D.1 and D.3 yields the result for the instantaneous rate of concentration change:

$$\frac{dN_i}{dt} = - \frac{4kTN_i^2}{3\mu} \quad (D.4)$$

Equations D.2-D.4 strictly apply only for $Kn \ll 1$. The classical continuum results can be extended to $Kn = 1$ without serious error with the Cunningham correction factor:

$$D_i = \frac{kT}{6\pi\mu r_i} \left(1 + \frac{A_i \Lambda}{r_i} \right)$$

where

Λ = mean free path of carrier fluid

$A_i = 1.125 + 0.400 \exp(-1.10 r_i/\Lambda)$

D.2. Collision frequency by free molecule theory

If Kn is of the order of 10 or greater, the collision frequency may be evaluated directly from the kinetic theory of dilute gases. Here attention is centered on the probability that a collision will occur between the i th and j th species. A Maxwellian velocity distribution is assumed, with an average particle velocity of:

$$\bar{c} = \sqrt{\frac{8kT}{\pi m}}$$

Following the notation of Hidy and Brock⁽⁵⁵⁾, the resulting collision frequency can be written:

$$L_{ij}^{(f)} = M_{ij} \left[\frac{8\pi kT (m_i + m_j)}{m_i m_j} \right]^{1/2} R_{ij}^2 N_i N_j$$

where

are as above;

m_i, m_j = particulate mass of the i th, j th species, respectively.

If $m_i = \rho \cdot \frac{4}{3} \pi r_i^3$ and density is constant:

$$L_{ij}^{(f)} = M_{ij} \left[\frac{6kT}{\rho} \right]^{1/2} \frac{(r_i^3 + r_j^3)^{1/2} (r_i + r_j)^2}{(r_i r_j)^{3/2}} N_i N_j \quad (D.6)$$

For the case of a homogeneous aerosol where $r_i = r_j$, (D.6) reduces to:

$$L_{ii}^{(f)} = \left[\frac{48kT}{\rho_i} \right]^{1/2} r_i^{1/2} N_i^2 \quad (D.7)$$

The rate of change of concentration is found by combining equations D.1 and D.7. Since only one size is present, the first term of D.1 is zero;

$$\frac{dN_i}{dt} = - \left[\frac{48kT}{\rho_i} \right]^{1/2} r_i^{1/2} N_i^2 \quad (D.8)$$

D.3. The transition zone

While the above expressions are incomplete in their coverage,

they have been experimentally verified within their respective areas of applicability. A number of attempts have been made to extend approximately either of the two derivations over larger ranges of Kn. None have been elegant theoretical successes, largely due to the lack of a quantitative understanding of gas-particle dynamics in the range $0.1 < Kn < 10$. The approach of Fuchs⁽⁵⁶⁾ is useful however. He extended continuum theory by arranging a spherical layer around the absorbing particle where there is a jump in aerosol concentration. The thickness of this layer is of the order of the mean free path of the particles. Fuchs empirically took rarefaction effects into account by forcing his results to agree with the limiting cases at high and low Kn. He proposed that the classical collision rate could be corrected in the form (from Hidy and Brock⁽⁵⁵⁾):

$$L_{ij} = \beta L_{ij}^{(c)} \quad (D.9)$$

Where $L_{ij}^{(c)}$ is expressed by equation D.2 or D.3. The analytic expression for β is quite involved, but its qualitative behavior is exhibited in Figure 26, taken from Hidy and Brock⁽⁵⁵⁾. Of interest are the peaking of β in the region $5 < \Lambda/r < 8$ and the relative behavior of the continuum and free molecule theories.

D.4. Application of the theory

For other than long time intervals in the continuum regime, the full general treatment of equation D.1 is difficult to apply to a given experimental situation. The problem with the discrete case lies in the large number of variables to be handled, while the continuous formulation

is extremely difficult to solve for other than very simple boundary conditions. For this reason, one is led to use the homogeneous rate equations (D.4 and D.8). To do this with confidence, an estimate should be made of the error involved. A polydispersion factor, PDF, is defined to be the factorial change in the coagulation (or collision) rate due to size heterogeneity:

$$\left(\frac{dN}{dt} \right)_{\text{polydisperse}} = \text{PDF} \left(\frac{dN}{dt} \right)_{\text{monodisperse}}$$

This factor is determined by investigating the dependence of collision frequency on particle size.

For the continuum case, equation D.2 may be written:

$$L_{ij}^{(c)} = M_{ij} \frac{2kT}{3\mu} \frac{(r_i + r_j)^2}{r_i r_j} N_i N_j$$

The size dependence term, normalized to equal one when $r_i = r_j$, is the polydispersion factor:

$$\text{PDF}^{(c)}(r_i, r_j) = \frac{(r_i + r_j)^2}{4r_i r_j} \quad (\text{D.10})$$

This is the result obtained by Whytlaw-Gray and Patterson⁽⁵⁷⁾.

Numerical values of D.10 can be combined for any given distribution in the following way:

$$\begin{aligned} \text{PDF} = & (f_1)^2 + (f_2)^2 + \dots + (f_k)^2 + (f_1)(f_2) \text{PDF}(r_1, r_2) + \dots \\ & + (f_i)(f_j) \text{PDF}(r_i, r_j) + \dots + (f_{k-1})(f_k) \text{PDF}(r_{k-1}, r_k) \quad i \neq j \end{aligned}$$

or

$$\text{PDF} = \sum_{i=1}^k \sum_{j=1}^k (f_i)(f_j) \text{PDF}(r_i, r_j) \quad (\text{D.11})$$

where

k = no. of groups, 1, 2, 3 ... k

N = total number of particles present/unit volume;

group i has $f_i N$ particles/unit volume, size r_i .

$\text{PDF}(r_i, r_j) = 1.0$ when $i = j$

As an example $\text{PDF}^{(c)}(1,5) = 1.80$, but when the particles are evenly divided among sizes 1 through 5, $\text{PDF}^{(c)}$ drops to 1.185.

In the free-molecule regime, equation D.6 gives the size dependence directly:

$$\frac{(r_i^3 + r_j^3)^{1/2} (r_i + r_j)^2}{(r_i r_j)^{3/2}} \quad (\text{D.12})$$

Since this represents a net factor of $r^{1/2}$ even for a homogeneous aerosol, an expression for a polydispersion factor cannot be explicitly written. What must be done to substitute the term D.12 for $\text{PDF}(r_i, r_j)$ in equation D.11. This sum must then be "normalized" by dividing by the value of D.12 for a monodisperse system of equal mass and number concentration:

$$4\sqrt{2} \bar{r}^{1/2}$$

where

\bar{r} = mass mean size

$$= (f_1 r_1^3 + f_2 r_2^3 + \dots + f_k r_k^3)^{1/3}$$

Substituting:

$$\text{PDF}^{(f)} = \frac{\sum_{i=1}^k \sum_{j=1}^k (f_i)(f_j) \frac{(r_i^3 + r_j^3)^{1/2} (r_i + r_j)^2}{(r_i r_j)^{3/2}}}{4\sqrt{2} \left(\sum_{i=1}^k f_i r_i^3 \right)^{1/6}} \quad (\text{D.13})$$

For the numerical example above, where the particles are evenly divided by number among sizes 1-5, $\text{PDF}^{(f)}$ has the value 0.755. When the size distribution width is 1-2 (mass=1,10), $\text{PDF}^{(f)}$ has the value 0.877. Thus, in the free molecule regime, heterogeneity in particle size tends to reduce the coagulation rate when compared to the corresponding homogeneous aerosol of mass-mean-size.

From the above it can be seen that the homogeneous coagulation rate equation will, in the continuum case, provide an underestimate and in the free molecule case, overestimate the rate. What to do about the transition zone remains unclear as the polydispersion factor changes direction here. It appears that for reasonably short times and for reasonably narrow distributions, the homogeneous equation may be used

to calculate the net change in particle concentration and the corresponding change in mass-mean-size. For an initially wide distribution but for short times, a value of PDF may be calculated based on the initial distribution and allowed to remain constant.

Appendix E

Coagulation by Slip-Collision

When a supersaturated vapor condenses in a nozzle, a distribution of particle sizes is introduced into the accelerating carrier flow. If it is assumed that there is relative motion between the particles and the carrier, and in particular that there is a velocity lag dependence on particle size, a slip-collision-coagulation mechanism will arise from the relative motion between particles of differing size. In the case of an accelerating flow, the larger particles will react more slowly to a change in stream velocity and will be overtaken by the smaller particles. The reverse can take place with passage through a normal shock; the smaller particles will decelerate rapidly and collide with those of larger size.

Crowe and Willoughby⁽⁵⁸⁾⁽⁵⁹⁾ have provided an analysis of this phenomenon. Following their presentation, the rate at which particles of size 1 collide with a single particle of size 2 is given by

$$\dot{N}_{1 \rightarrow 2} = \pi (r_{p1} + r_{p2})^2 N_1 |u_{p1} - u_{p2}| \quad (\text{E.1})$$

where

$r_{p1,2}$ = particle radii

$u_{p1,2}$ = particle velocities

N_1 = concentration of particles of radius r_{p1} , no./unit volume

$(r_{p1} + r_{p2})$ = collision cross-section

This equation assumes that the particle trajectories are parallel and that inter-particle forces are not active. Crowe, Willoughby, et.al.⁽⁶⁰⁾ show that the interaction of the particle flow fields has an insignificant effect. If it is further assumed that the probability of sticking on contact is unity, equation E.1 also gives the rate of reduction of N_1 due to collision with a single particle of radius r_{p2} . The rate of mass accumulation by particle r_{p2} is then given by

$$\Delta \dot{m}_{1 \rightarrow 2} = \pi (r_{p1} + r_{p2})^2 m_1 N_1 \left| u_{p1} - u_{p2} \right| \quad (\text{E.2})$$

where m_1 is the mass of an individual particle of size r_{p1} .

If Δx is the distance travelled by particles of size n in time Δt , equation E.2 may be generalized to include a multiplicity of particle sizes

$$m_n(x+\Delta x) = m_n(x) + \pi \Delta x \sum_{j=1}^n (r_{pn} + r_{pj})^2 m_j N_j \left| \frac{u_{pj}}{u_{pn}} - 1 \right| \quad (\text{E.3})$$

where $j=1$ represents the smallest particle present. As each collision takes place, the larger particle will increase in size and the number density of the smaller particles will be correspondingly reduced. The change in number concentration is given by

$$N_n(x+\Delta x) = N_n(x) \left[1 - \pi \Delta x \sum_{j>n} (r_{pn} + r_{pj})^2 N_j \right. \\ \left. \cdot \left| \frac{u_{pj}}{u_{pn}} - 1 \right| \frac{A(x) u_{pn}(x)}{A(x+\Delta x) u_{pn}(x+\Delta x)} \right] \quad (\text{E.4})$$

where A is the cross-sectional flow area and the summation is carried out for all sizes larger than n . The term outside the brackets accounts

for the fact that the particle number density is also dependent on the change in flow area and particle velocity.

Successive application of equations E.3 and E.4 provides the variation of particle size and number density with distance along the nozzle. In addition to specification of the area change and particle velocities, it is necessary to know or assume the initial particle size and number distribution. In practice, the calculation procedure is applied to an initial distribution which has been broken down into a number of discrete steps in order to facilitate the numerical treatment.

Crowe and Willoughby⁽⁵⁸⁾⁽⁵⁹⁾ have shown that the chief mechanism responsible for the change in particle velocity is that due to aerodynamic drag (i.e., momentum exchange on coalescence may be neglected). Assuming a constant gas velocity over an incremental size Δx , the change of velocity of a particle of size n is given by

$$\Delta u_{pn} = \left[u_g - u_{pn}(x) \right] \cdot \left\{ 1 - \exp \left[- \frac{3C_D Re \mu \Delta x}{16 \rho_p r_{pn}^2 u_{pn}(x)} \right] \right\} \quad (E.5)$$

where

C_D = particle drag coefficient

Re = Reynold's number of particle relative to gas

u_g = gas velocity

μ = gas viscosity

ρ_p = particle density

Equation E.5 is thus used to determine the particle velocities for insertion into equations E.3 and E.4. If the exponential in E.5 is

consistently negligible, there will be no relative motion between the particles and the carrier and the coagulation mechanism will be inoperative.

An improvised universal drag law has been obtained by Crowe, Willoughby, et. al.⁽⁴⁷⁾ by forcing an empirical curve to satisfy the available data and several proven limiting theories. Rather than present the extremely complicated expression for C_D , the behavior of C_D versus Reynolds and Mach number is shown in Figure 27, taken from the above reference.

Appendix F

Tabulation of Theoretical Distribution Parameters

Tabulation of Experimental Data

All data sets are identified by a number of the form a * b * c with the following possible values:

a.	.005	
	.010	nominal vapor mass fraction
	.015	
b.	1	nominal static pressure ratio at incidence, with
	2	the lower value indicating a higher (P/P_0); (closer
	3	to the throat).
	4	
c.	12.5	
	10.5	distance from throat to plane of observation
	8.5	(nozzle length).
	6.5	
	4.5	

Table F.2. The indicated values of incident light intensity, I_{01} , are as recorded. They have not been corrected for scattering geometry or filter attenuation (see Appendix B).

* note: For the scattered intensity measurements taken at a nozzle length of 12.5 in. (page F.3), the geometric correction factor has a value of 6.33×10^6 rather than 5.5×10^6 due to a change in scattering geometry (see Appendix B.3).

Table F.1. Theoretical Distribution Parameters

RUN IDENT.	α_{\min}	α_{\max}	h (no/cm ³)	n
.005*1*12.5	0.0301	0.60	0.15E10	3.48
.005*2*12.5	0.0274	0.73	0.87E 9	3.66
.005*3*12.5	0.0261	0.90	0.31E 9	4.10
.005*4*12.5	0.0264	0.83	0.45E 9	3.90
.010*1*12.5	0.0498	0.89	0.21E10	3.44
.010*2*12.5	0.0480	0.98	0.38E10	3.06
.010*3*12.5	0.0435	1.09	0.29E10	3.12
.015*1*12.5	0.0654	1.08	0.46E10	3.18
.015*2*12.5	0.0608	1.25	0.32E10	3.32
.015*3*12.5	0.0635	1.30	0.37E10	2.86
.005*1*10.5	0.0301	0.55	0.14E10	3.64
.005*2*10.5	0.0274	0.70	0.11E10	3.62
.005*3*10.5	0.0261	0.84	0.45E 9	4.02
.005*4*10.5	0.0264	0.83	0.44E 9	4.00
.010*1*10.5	0.0498	0.75	0.48E10	3.20
.010*2*10.5	0.0480	0.90	0.64E10	2.74
.010*3*10.5	0.0435	1.04	0.32E10	3.16
.015*1*10.5	0.0654	1.02	0.52E10	3.22
.015*2*10.5	0.0607	1.14	0.41E10	3.28
.015*3*10.5	0.0635	1.35	0.40E10	3.16
.005*1* 8.5	0.0301	0.51	0.16E10	3.62
.005*2* 8.5	0.0274	0.71	0.68E 9	3.94
.005*3* 8.5	0.0261	0.88	0.31E 9	4.18
.005*4* 8.5	0.0263	0.84	0.33E 9	4.16
.010*1* 8.5	0.0498	0.77	0.51E10	3.22
.010*2* 8.5	0.0480	0.90	0.58E10	3.12
.010*3* 8.5	0.0433	0.95	0.34E10	3.30
.015*1* 8.5	0.0645	0.98	0.55E10	3.32
.015*2* 8.5	0.0606	1.17	0.45E10	3.30
.010*3* 8.5	0.0632	1.23	0.37E10	3.44
.005*1* 6.5	0.0301	0.49	0.13E10	3.80
.005*2* 6.5	0.0274	0.73	0.61E 9	4.04
.005*3* 6.5	0.0260	0.59	0.25E10	3.32
.005*4* 6.5	0.0255	0.87	0.24E 9	4.36
.010*1* 6.5	0.0498	0.76	0.20E10	3.90
.010*2* 6.5	0.0479	0.93	0.32E10	3.46
.010*3* 6.5	0.0429	0.92	0.28E10	3.50
.015*1* 6.5	0.0652	0.87	0.73E10	3.30
.015*2* 6.5	0.0602	1.16	0.35E10	3.66
.015*3* 6.5	0.0625	1.08	0.43E10	3.50
.005*1* 4.5	0.0301	0.48	0.10E10	4.00
.005*2* 4.5	0.0273	0.71	0.40E 9	4.30
.005*3* 4.5	0.0252	0.40	0.28E11	2.23
.005*4* 4.5	0.0128	0.56	0.17E10	3.56
.010*1* 4.5	0.0496	0.73	0.50E10	3.53
.010*2* 4.5	0.0474	0.82	0.44E10	3.42
.010*3* 4.5	0.0414	0.87	0.30E10	3.64
.015*1* 4.5	0.0645	0.99	0.62E10	3.46
.015*2* 4.5	0.0591	1.04	0.67E10	3.36
.015*3* 4.5	0.0605	1.06	0.31E10	3.90

Table F.2. Experimental Scattered Light Intensity (millivolts)

Run	.005*1*12.5		.005*2*12.5		.005*3*12.5		.005*4*12.5		.010*1*12.5	
θ	$I_1(\theta)$	$I_2(\theta)$	$I_1(\theta)$	$I_2(\theta)$	$I_1(\theta)$	$I_2(\theta)$	$I_1(\theta)$	$I_2(\theta)$	$I_1(\theta)$	$I_2(\theta)$
40	9.0	5.1	20.0	11.5	20.1	12.4			172.0	99.0
45	8.0	3.9	17.7	8.7	17.8	9.1			154.0	77.0
50	7.2	3.0	16.1	6.5	16.0	6.5			140.0	58.0
55	6.7	2.3	14.9	4.9	14.7	4.8			129.0	43.0
60	6.3	1.6	13.9	3.7	13.7	3.5			121.0	30.0
65	6.0	1.1	13.1	2.8	13.0	2.6	13.3	2.7	114.0	20.0
70	5.8	0.8	12.6	1.9	12.4	1.9	12.7	1.8	111.0	12.0
75	5.6	0.5	12.2	1.2	12.0	1.2	12.2	1.2	107.0	7.0
80	5.5	0.3	11.9	0.7	11.7	0.7	12.0	0.7	104.0	4.0
85	5.4	0.2	11.6	0.4	11.4	0.4	11.5	0.5	101.0	2.0
90	5.3	0.1	11.5	0.3	11.1	0.3	11.3	0.4	98.0	1.0
95	5.3	0.2	11.4	0.4	11.1	0.4	11.1	0.5	96.0	2.0
100	5.3	0.3	11.4	0.6	11.1	0.7	11.1	0.7	94.0	4.0
105	5.3	0.5	11.6	1.1	11.2	1.1	11.3	1.1	95.0	7.0
110	5.4	0.8	11.9	1.6	11.4	1.8	11.6	1.8	96.0	12.0
115			0.0	0.0	0.0	0.0	11.9	2.5	99.0	19.0
120			0.0	0.0	0.0	0.0			103.0	28.0
125			0.0	0.0	0.0	0.0			108.0	39.0
130			0.0	0.0	0.0	0.0			114.0	51.0
135			0.0	0.0	0.0	0.0			123.0	68.0
140			0.0	0.0	0.0	0.0			135.0	89.0
I_{01}	25.0		38.9		38.9		38.9		79.2	

Run	.010*2*12.5		.010*3*12.5		.015*1*12.5		.015*2*12.5		.015*3*12.5	
θ	$I_1(\theta)$	$I_2(\theta)$	$I_1(\theta)$	$I_2(\theta)$	$I_1(\theta)$	$I_2(\theta)$	$I_1(\theta)$	$I_2(\theta)$	$I_1(\theta)$	$I_2(\theta)$
40	217.0	130.0	271.0	165.0	171.0	101.0	220.0	132.0	265.0	157.0
45	198.0	100.0	242.0	127.0	152.0	77.0	198.0	102.0	234.0	121.0
50	179.0	77.0	218.0	93.0	139.0	59.0	179.0	78.0	210.0	91.0
55	165.0	58.0	201.0	69.0	128.0	44.0	164.0	57.0	191.0	67.0
60	153.0	42.0	187.0	48.0	117.0	31.0	149.0	40.0	175.0	47.0
65	143.0	28.0	176.0	33.0	108.0	21.0	138.0	28.0	163.0	33.0
70	135.0	19.0	165.0	22.0	101.0	14.0	128.0	17.0	152.0	22.0
75	129.0	11.0	157.0	12.0	96.0	8.0	121.0	11.0	144.0	13.0
80	124.0	6.0	151.0	7.0	93.0	4.0	114.0	6.0	135.0	7.0
85	121.0	3.0	145.0	3.0	90.0	1.0	111.0	3.0	128.0	3.0
90	119.0	2.0	140.0	1.0	88.0	0.0	107.0	1.0	123.0	1.0
95	117.0	2.0	137.0	2.0	87.0	1.0	105.0	2.0	120.0	2.0
100	115.0	5.0	134.0	5.0	86.0	3.0	104.0	4.0	116.0	4.0
105	113.0	9.0	134.0	9.0	85.0	5.0	103.0	8.0	115.0	8.0
110	112.0	15.0	135.0	16.0	86.0	11.0	104.0	14.0	116.0	14.0
115	114.0	22.0	139.0	26.0	87.0	16.0	105.0	20.0	119.0	21.0
120	119.0	34.0	144.0	37.0	91.0	23.0	109.0	28.0	122.0	30.0
125	127.0	47.0	151.0	51.0	95.0	33.0	112.0	39.0	128.0	41.0
130	137.0	63.0	159.0	69.0	100.0	43.0	119.0	50.0	133.0	55.0
135	151.0	81.0	171.0	91.0	109.0	55.0	127.0	64.0	142.0	70.0
140	168.0	103.0	187.0	117.0	118.0	71.0	139.0	84.0	153.0	88.0
I_{01}	49.9		49.9		20.5		20.5		20.5	

* See note page F.1

Table F.2. Experimental Scattered Light Intensity (millivolts)

Run	.005*1*10.5		.005*2*10.5		.005*3*10.5		.005*4*10.5		.010*1*10.5	
θ	$I_1(\theta)$	$I_2(\theta)$	$I_1(\theta)$	$I_2(\theta)$	$I_1(\theta)$	$I_2(\theta)$	$I_1(\theta)$	$I_2(\theta)$	$I_1(\theta)$	$I_2(\theta)$
40	12.9	7.9	24.0	14.8	25.8	14.7	22.9	14.1	183.0	107.0
45	11.8	6.1	21.7	11.6	22.9	11.5	20.7	11.1	167.0	83.0
50	10.9	4.8	19.9	9.0	20.9	8.7	19.0	8.5	154.0	62.0
55	10.2	3.7	18.5	6.8	19.3	6.4	17.6	6.3	143.0	47.0
60	9.6	2.8	17.3	5.0	18.1	4.6	16.5	4.6	133.0	34.0
65	9.2	2.0	16.3	3.5	17.3	3.2	15.5	3.1	126.0	23.0
70	8.8	1.3	15.7	2.3	16.5	2.0	14.7	2.1	119.0	16.0
75	8.5	1.0	15.2	1.4	16.0	1.3	14.1	1.3	115.0	9.0
80	8.2	0.6	14.8	0.8	15.4	0.8	13.7	0.9	112.0	5.0
85	8.1	0.4	14.5	0.5	15.0	0.5	13.4	0.5	109.0	2.0
90	8.0	0.3	14.3	0.3	14.7	0.4	13.2	0.4	107.0	1.0
95	7.9	0.4	14.1	0.5	14.5	0.5	13.2	0.5	107.0	2.0
100	7.9	0.6	14.1	0.9	14.5	0.8	13.3	0.8	107.0	4.0
105	8.2	0.8	14.1	1.5	14.7	1.5	13.7	1.2	108.0	9.0
110	8.4	1.3	14.5	2.3	15.1	2.2	14.3	2.0	110.0	12.0
115									112.0	20.0
120									116.0	30.0
125									121.0	43.0
130									129.0	57.0
135									142.0	77.0
140									158.0	101.0
I_{01}	38.9		38.9		38.9		38.9		79.2	

Run	.010*2*10.5		.010*3*10.5		.015*1*10.5		.015*2*10.5		.015*3*10.5	
θ	$I_1(\theta)$	$I_2(\theta)$	$I_1(\theta)$	$I_2(\theta)$	$I_1(\theta)$	$I_2(\theta)$	$I_1(\theta)$	$I_2(\theta)$	$I_1(\theta)$	$I_2(\theta)$
40	237.0	142.0	274.0	167.0	179.0	104.0	229.0	136.0	207.0	126.0
45	212.0	109.0	251.0	130.0	161.0	79.0	203.0	103.0	186.0	95.0
50	192.0	84.0	232.0	97.0	145.0	60.0	182.0	79.0	168.0	71.0
55	179.0	63.0	216.0	70.0	132.0	45.0	164.0	57.0	151.0	51.0
60	167.0	46.0	202.0	49.0	122.0	33.0	152.0	41.0	138.0	37.0
65	158.0	32.0	189.0	32.0	115.0	22.0	142.0	28.0	128.0	26.0
70	150.0	20.0	178.0	20.0	108.0	14.0	134.0	17.0	119.0	17.0
75	144.0	12.0	169.0	12.0	103.0	8.0	128.0	10.0	112.0	10.0
80	140.0	6.0	162.0	7.0	101.0	4.0	123.0	5.0	107.0	5.0
85	136.0	3.0	156.0	3.0	97.0	2.0	120.0	2.0	102.0	2.0
90	132.0	1.0	151.0	1.0	95.0	1.0	117.0	1.0	97.0	1.0
95	131.0	2.0	148.0	2.0	94.0	2.0	114.0	1.0	94.0	2.0
100	129.0	5.0	146.0	5.0	94.0	4.0	113.0	4.0	91.0	3.0
105	130.0	9.0	145.0	10.0	93.0	7.0	111.0	8.0	90.0	7.0
110	131.0	16.0	146.0	17.0	93.0	11.0	110.0	13.0	90.0	11.0
115	135.0	24.0	148.0	25.0	95.0	17.0	111.0	19.0	91.0	16.0
120	139.0	35.0	152.0	37.0	98.0	24.0	112.0	28.0	93.0	24.0
125	146.0	46.0	159.0	51.0	101.0	33.0	117.0	39.0	97.0	32.0
130	153.0	62.0	170.0	69.0	107.0	45.0	125.0	51.0	100.0	43.0
135	165.0	82.0	185.0	89.0	116.0	60.0	135.0	67.0	106.0	55.0
140	181.0	105.0	205.0	114.0	128.0	77.0	149.0	87.0	113.0	70.0
I_{01}	49.9		49.9		20.5		20.5		10.5	

Table F.2. Experimental Scattered Light Intensity (millivolts)

Run	.005*1* 8.5		.005*2* 8.5		.005*3* 8.5		.005*4* 8.5		.010*1* 8.5	
θ	$I_1(\theta)$	$I_2(\theta)$	$I_1(\theta)$	$I_2(\theta)$	$I_1(\theta)$	$I_2(\theta)$	$I_1(\theta)$	$I_2(\theta)$	$I_1(\theta)$	$I_2(\theta)$
40	8.2	4.8	23.4	13.3	25.5	15.0	21.9	12.7	168.0	97.0
45	7.4	3.7	21.1	10.2	23.0	11.7	19.9	9.7	150.0	75.0
50	6.7	2.9	19.3	7.8	20.9	8.9	18.1	7.1	136.0	58.0
55	6.2	2.2	17.8	5.9	19.2	6.6	16.8	5.2	126.0	44.0
60	5.8	1.6	16.9	4.4	18.0	4.7	15.7	3.9	119.0	33.0
65	5.5	1.1	16.1	3.1	16.9	3.3	14.9	2.8	112.0	22.0
70	5.3	0.7	15.4	2.1	16.1	2.1	14.1	1.9	108.0	14.0
75	5.2	0.4	14.9	1.3	15.5	1.2	13.5	1.2	105.0	8.0
80	5.1	0.3	14.6	0.7	14.9	0.7	13.1	0.7	102.0	4.0
85	5.0	0.2	14.2	0.3	14.7	0.4	12.8	0.4	101.0	1.0
90	5.0	0.1	13.9	0.2	14.4	0.2	12.7	0.3	97.0	0.0
95	5.0	0.2	13.8	0.3	14.2	0.3	12.5	0.4	97.0	1.0
100	5.0	0.3	14.0	0.6	14.2	0.7	12.5	0.7	98.0	3.0
105	5.1	0.5	14.0	1.1	14.4	1.3	12.7	1.2	98.0	7.0
110	5.2	0.7	14.2	1.9	14.7	2.2	12.9	1.9	98.0	12.0
115									99.0	18.0
120									102.0	27.0
125									107.0	38.0
130									117.0	51.0
135									127.0	67.0
140									143.0	86.0
I_{01}	28.5		44.5		44.5		44.5		58.2	

Run	.010*2* 8.5		.010*3* 8.5		.015*1* 8.5		.015*2* 8.5		.015*3* 8.5	
θ	$I_1(\theta)$	$I_2(\theta)$	$I_1(\theta)$	$I_2(\theta)$	$I_1(\theta)$	$I_2(\theta)$	$I_1(\theta)$	$I_2(\theta)$	$I_1(\theta)$	$I_2(\theta)$
40	299.0	178.0	275.0	165.0	197.0	127.0	313.0	189.0	319.0	193.0
45	268.0	137.0	246.0	125.0	175.0	96.0	281.0	142.0	287.0	150.0
50	243.0	106.0	224.0	94.0	160.0	73.0	254.0	107.0	260.0	111.0
55	224.0	79.0	206.0	70.0	145.0	54.0	233.0	81.0	237.0	82.0
60	209.0	57.0	192.0	51.0	135.0	38.0	216.0	59.0	220.0	59.0
65	196.0	39.0	181.0	36.0	126.0	27.0	201.0	41.0	205.0	40.0
70	186.0	23.0	171.0	23.0	121.0	18.0	188.0	27.0	191.0	26.0
75	178.0	13.0	163.0	13.0	115.0	10.0	179.0	16.0	180.0	15.0
80	171.0	7.0	158.0	7.0	111.0	5.0	172.0	8.0	172.0	8.0
85	167.0	3.0	154.0	2.0	109.0	2.0	166.0	3.0	166.0	3.0
90	164.0	1.0	150.0	1.0	105.0	1.0	161.0	1.0	160.0	1.0
95	162.0	2.0	149.0	2.0	105.0	2.0	157.0	2.0	157.0	2.0
100	161.0	5.0	148.0	6.0	104.0	4.0	154.0	5.0	154.0	5.0
105	162.0	10.0	148.0	10.0	104.0	7.0	152.0	10.0	153.0	10.0
110	165.0	19.0	149.0	17.0	105.0	12.0	152.0	17.0	153.0	16.0
115	169.0	30.0	153.0	26.0	106.0	19.0	154.0	27.0	155.0	25.0
120	174.0	44.0	158.0	38.0	110.0	28.0	157.0	39.0	156.0	36.0
125	183.0	60.0	165.0	55.0	113.0	39.0	162.0	54.0	162.0	51.0
130	194.0	79.0	174.0	72.0	121.0	52.0	171.0	71.0	170.0	66.0
135	207.0	101.0	186.0	93.0	130.0	68.0	183.0	92.0	182.0	87.0
140	225.0	129.0	203.0	120.0	142.0	88.0	199.0	118.0	197.0	113.0
I_{01}	58.2		58.2		23.3		23.3		23.3	

Table F.2. Experimental Scattered Light Intensity (millivolts)

Run	.005*1* 6.5		.005*2* 6.5		.005*3* 6.5		.005*4* 6.5		.010*1* 6.5	
θ	$I_1(\theta)$	$I_2(\theta)$	$I_1(\theta)$	$I_2(\theta)$	$I_1(\theta)$	$I_2(\theta)$	$I_1(\theta)$	$I_2(\theta)$	$I_1(\theta)$	$I_2(\theta)$
40	11.6	6.8	24.6	14.2	27.0	16.6	21.0	12.3	106.5	65.5
45	10.5	5.3	22.3	11.0	24.1	12.7	18.9	9.7	96.0	51.5
50	9.6	4.1	20.4	8.2	22.1	9.5	17.4	7.6	87.5	39.0
55	9.0	3.2	18.8	6.0	20.4	7.0	16.2	5.7	80.5	29.5
60	8.5	2.3	17.6	4.2	19.1	4.9	15.2	4.3	75.5	21.5
65	8.2	1.7	16.7	2.8	18.0	3.3	14.3	3.0	71.5	14.5
70	7.8	1.2	15.9	1.7	17.1	2.0	13.6	2.0	68.0	9.5
75	7.6	0.8	15.4	1.0	16.6	1.1	13.1	1.3	65.5	5.5
80	7.4	0.6	14.9	0.4	16.3	0.6	12.8	0.8	63.5	3.0
85	7.3	0.5	14.6	0.1	16.2	0.2	12.5	0.6	62.5	1.0
90	7.2	0.4	14.5	0.0	16.0	0.0	12.2	0.5	62.0	0.5
95	7.1	0.4	14.4	0.1	16.0	0.2	12.0	0.6	61.5	1.0
100	7.2	0.6	14.5	0.4	16.1	0.6	11.9	0.9	61.5	2.5
105	7.3	0.9	14.6	1.0	16.3	1.3	11.9	1.3	62.0	4.5
110	7.4	1.3	14.9	1.9	16.7	2.3	12.1	1.9	63.0	8.0
115									64.5	12.5
120									67.0	17.5
125									70.0	24.5
130									74.0	32.0
135									80.0	41.5
140									88.0	53.0
I_{01}	44.5		44.5		44.5		44.5		52.5	

Run	.010*2* 6.5		.010*3* 6.5		.015*1* 6.5		.015*2* 6.5		.015*3* 6.5	
θ	$I_1(\theta)$	$I_2(\theta)$	$I_1(\theta)$	$I_2(\theta)$	$I_1(\theta)$	$I_2(\theta)$	$I_1(\theta)$	$I_2(\theta)$	$I_1(\theta)$	$I_2(\theta)$
40	251.0	149.0	217.0	132.0	160.0	103.0	270.0	166.0	244.0	146.0
45	225.0	117.0	196.0	104.0	145.0	79.0	240.0	129.0	219.0	111.0
50	204.0	89.0	178.0	80.0	133.5	58.0	219.0	98.0	199.0	83.0
55	187.0	65.0	164.0	59.0	123.5	43.0	202.0	71.0	182.0	61.0
60	175.0	47.0	154.0	43.0	115.0	30.0	188.0	50.0	168.0	44.0
65	165.0	31.0	145.0	30.0	109.0	20.0	176.0	35.0	157.0	30.0
70	157.0	20.0	138.0	20.0	103.0	13.0	165.0	23.0	149.0	19.0
75	151.0	11.0	131.0	11.0	99.0	8.0	158.0	14.0	142.0	11.0
80	146.0	6.0	127.0	5.0	95.5	4.0	152.0	8.0	136.0	6.0
85	142.0	2.0	124.0	3.0	93.5	2.0	146.0	3.0	132.0	3.0
90	140.0	1.0	122.0	1.0	92.0	1.0	141.0	1.0	129.0	1.0
95	138.0	2.0	120.0	2.0	91.0	2.0	137.0	3.0	127.0	2.0
100	137.0	5.0	120.0	5.0	91.0	4.0	135.0	5.0	126.0	4.0
105	137.0	9.0	121.0	9.0	91.5	7.0	133.0	9.0	125.0	8.0
110	138.0	18.0	121.0	15.0	92.0	11.0	132.0	15.0	126.0	14.0
115	140.0	27.0	124.0	22.0	94.0	17.0	133.0	23.0	127.0	22.0
120	144.0	41.0	127.0	33.0	97.0	23.0	137.0	33.0	129.0	31.0
125	150.0	54.0	133.0	45.0	101.0	32.0	142.0	45.0	134.0	42.0
130	159.0	72.0	140.0	60.0	106.0	44.0	149.0	60.0	141.0	57.0
135	172.0	91.0	151.0	77.0	115.0	58.0	157.0	78.0	151.0	74.0
140	188.0	114.0	166.0	100.0	128.0	77.0	169.0	103.0	167.0	95.0
I_{01}	58.2		58.2		23.3		23.3		23.3	

Table F.2. Experimental Scattered Light Intensity (millivolts)

Run	.005*1* 4.5		.005*2* 4.5		.005*3* 4.5		.005*4* 4.5		.010*1* 4.5	
θ	$I_1(\theta)$	$I_2(\theta)$	$I_1(\theta)$	$I_2(\theta)$	$I_1(\theta)$	$I_2(\theta)$	$I_1(\theta)$	$I_2(\theta)$	$I_1(\theta)$	$I_2(\theta)$
40	18.0	10.6	32.5	21.0	21.6	12.7	19.0	12.5	153.5	89.0
45	16.3	8.2	29.4	16.4	19.6	10.1	17.2	9.7	137.5	68.0
50	15.0	6.2	27.0	12.4	18.0	7.8	15.9	7.4	126.0	52.0
55	13.9	4.7	25.0	9.2	16.5	5.8	14.7	5.6	117.0	39.5
60	13.2	3.5	23.5	6.6	15.5	4.2	13.9	4.0	109.5	29.0
65	12.5	2.4	22.4	4.7	14.8	2.8	13.2	2.8	103.5	20.0
70	12.0	1.6	21.4	3.2	14.3	1.7	12.7	1.7	99.0	13.0
75	11.7	1.0	20.6	2.0	13.9	1.0	12.3	1.0	95.5	7.0
80	11.4	0.6	20.0	1.0	13.6	0.6	12.0	0.5	92.7	4.0
85	11.3	0.3	19.6	0.6	13.4	0.3	11.8	0.3	91.0	1.5
90	11.2	0.2	19.4	0.3	13.3	0.2	11.7	0.2	90.0	0.5
95	11.3	0.3	19.4	0.5	13.3	0.3	11.7	0.3	89.5	1.0
100	11.3	0.6	19.4	0.9	13.3	0.5	11.7	0.5	89.5	3.5
105	11.4	1.0	19.6	1.7	13.5	0.9	11.8	0.9	90.0	6.0
110	11.6	1.6	20.0	2.7	13.8	1.6	12.1	1.5	91.5	11.0
115	12.0	2.4	20.5	3.9	14.3	2.6	12.5	2.3	94.0	17.0
120	12.6	3.4	21.3	5.5	15.0	3.9	12.9	3.3	97.0	25.0
125	13.3	4.7	22.3	7.9	16.0	5.6	13.5	4.5	101.5	35.0
130	14.1	6.4	23.8	10.8	17.1	7.5	14.4	5.8	108.0	47.0
135	15.2	8.0	25.6	14.4	18.4	9.8	15.5	7.5	116.5	61.0
140	16.6	10.3	27.9	18.4	20.0	12.6	17.2	9.7	128.0	78.5
I_{01}	70.9		70.9		46.2		46.2		55.0	

Run	.010*2* 4.5		.010*3* 4.5		.015*1* 4.5		.015*2* 4.5		.015*3* 4.5	
θ	$I_1(\theta)$	$I_2(\theta)$	$I_1(\theta)$	$I_2(\theta)$	$I_1(\theta)$	$I_2(\theta)$	$I_1(\theta)$	$I_2(\theta)$	$I_1(\theta)$	$I_2(\theta)$
40	258.0	152.0	222.0	129.0	260.0	164.0	306.0	183.0	206.0	122.0
45	233.0	117.0	198.0	100.0	232.0	124.0	274.0	143.0	186.0	95.0
50	213.0	90.0	180.0	77.0	211.0	93.0	249.0	108.0	168.0	70.0
55	196.0	67.0	166.0	57.0	195.0	68.0	228.0	81.0	154.5	52.0
60	181.0	50.0	155.0	41.0	182.0	48.0	211.0	58.0	144.0	38.0
65	170.0	34.0	146.5	28.0	171.0	34.0	199.0	41.0	135.0	26.0
70	162.0	22.0	140.0	18.0	162.0	22.0	188.0	27.0	128.0	17.0
75	156.0	13.0	134.5	11.0	155.0	13.0	180.0	17.0	122.0	11.0
80	152.0	7.0	129.5	5.0	150.0	7.0	174.5	8.0	118.0	5.0
85	149.0	3.0	126.5	2.0	146.0	2.0	170.0	3.0	115.0	2.0
90	147.0	1.0	125.0	1.0	142.5	1.0	166.0	2.0	112.0	1.0
95	146.5	2.0	124.5	2.0	140.0	2.0	162.5	3.0	109.5	2.0
100	146.0	6.0	124.0	4.0	139.0	5.0	161.5	5.0	108.0	3.0
105	146.5	11.0	123.5	9.0	138.0	9.0	161.0	10.0	107.0	6.0
110	148.0	17.0	125.0	14.0	139.0	15.0	162.0	17.0	107.5	11.0
115	153.0	27.0	127.5	21.0	142.0	24.0	165.5	26.0	109.0	20.0
120	158.0	40.0	132.0	33.0	146.0	36.0	170.0	37.0	112.0	28.0
125	165.0	56.0	137.0	46.0	151.5	51.0	176.0	52.0	116.0	39.0
130	173.0	74.0	144.0	62.0	159.0	68.0	185.0	71.0	122.0	52.0
135	185.0	97.0	154.0	81.0	170.0	87.0	195.0	95.0	130.0	68.0
140	205.0	124.0	170.0	105.0	182.5	111.0	210.0	125.0	140.0	86.0
I_{01}	61.0		61.0		23.5		23.5		23.5	

Table F.3. Experimental Static Pressure Ratios, Nozzle Flow Conditions

Run	.005*1*12.5	.005*2*12.5	.005*3*12.5	.005*4*12.5	.010*1*12.5
x(in)	p/p ₀	p/p ₀	p/p ₀	p/p ₀	p/p ₀
0.5	0.4181	0.3922	0.3938	0.3957	0.4582
1.0	0.3635	0.3327	0.3315	0.3324	0.3867
1.5	0.3121	0.3055	0.2845	0.2852	0.3282
2.0	0.2715	0.2705	0.2522	0.2508	0.2857
2.5	0.2436	0.2433	0.2385	0.2273	0.2536
3.0	0.2161	0.2165	0.2160	0.2057	0.2278
3.5	0.1994	0.1978	0.1980	0.1926	0.2057
4.0	0.1822	0.1817	0.1819	0.1785	0.1886
4.5	0.1665	0.1661	0.1661	0.1648	0.1729
5.0	0.1531	0.1532	0.1530	0.1526	0.1603
5.5	0.1425	0.1422	0.1428	0.1422	0.1489
6.0	0.1323	0.1324	0.1322	0.1321	0.1390
6.5	0.1233	0.1225	0.1228	0.1227	0.1293
7.0	0.1156	0.1160	0.1167	0.1162	0.1214
7.5	0.1086	0.1092	0.1097	0.1095	0.1144
8.0	0.1019	0.1021	0.1028	0.1027	0.1069
8.5	0.0974	0.0974	0.0981	0.0980	0.1022
9.0	0.0921	0.0922	0.0927	0.0925	0.0962
9.5	0.0866	0.0871	0.0874	0.0876	0.0915
10.0	0.0823	0.0824	0.0827	0.0827	0.0861
10.5	0.0778	0.0785	0.0791	0.0790	0.0822
11.0	0.0742	0.0742	0.0750	0.0749	0.0780
12.0	0.0674	0.0677	0.0682	0.0682	0.0712
P (in Hg)	245.24	244.34	244.64	244.74	241.99
T ₀ (°K)	324.20	342.97	363.30	380.90	341.04
ω ₀	0.0049	0.0049	0.0049	0.0048	0.0107

Run	.010*2*12.5	.010*3*12.5	.015*1*12.5	.015*2*12.5	.015*3*12.5
x(in)	p/p ₀	p/p ₀	p/p ₀	p/p ₀	p/p ₀
0.5	0.3857	0.3891	0.4197	0.3906	0.3899
1.0	0.3330	0.3284	0.3939	0.3434	0.3293
1.5	0.3168	0.2835	0.3365	0.3275	0.2915
2.0	0.2828	0.2511	0.2927	0.2902	0.2781
2.5	0.2530	0.2394	0.2620	0.2601	0.2551
3.0	0.2272	0.2224	0.2348	0.2337	0.2306
3.5	0.2053	0.2043	0.2130	0.2121	0.2102
4.0	0.1883	0.1875	0.1944	0.1940	0.1926
4.5	0.1731	0.1728	0.1797	0.1794	0.1787
5.0	0.1602	0.1598	0.1651	0.1651	0.1645
5.5	0.1481	0.1482	0.1526	0.1526	0.1524
6.0	0.1381	0.1383	0.1417	0.1417	0.1419
6.5	0.1287	0.1283	0.1318	0.1318	0.1318
7.0	0.1210	0.1211	0.1239	0.1238	0.1239
7.5	0.1139	0.1141	0.1175	0.1173	0.1170
8.0	0.1069	0.1067	0.1104	0.1101	0.1095
8.5	0.1020	0.1020	0.1052	0.1050	0.1047
9.0	0.0958	0.0963	0.0991	0.0990	0.0986
9.5	0.0913	0.0914	0.0940	0.0939	0.0936
10.0	0.0860	0.0862	0.0888	0.0889	0.0887
10.5	0.0821	0.0821	0.0846	0.0845	0.0845
11.0	0.0780	0.0784	0.0805	0.0804	0.0806
12.0	0.0710	0.0713	0.0733	0.0732	0.0731
P (in Hg)	243.95	243.87	247.64	347.94	247.34
T ₀ (°K)	361.99	384.87	354.22	368.94	381.07
ω ₀	0.0108	0.0106	0.0151	0.0148	0.0149

Table F.3. Experimental Static Pressure Ratios, Nozzle Flow Conditions

Run	.005*1*10.5	.005*2*10.5	.005*3*10.5	.005*4*10.5	.010*1*10.5
x(in)	p/p ₀	p/p ₀	p/p ₀	p/p ₀	p/p ₀
0.5	0.4277	0.3955	0.3977	0.3968	0.4634
1.0	0.3682	0.3312	0.3300	0.3288	0.3865
1.5	0.3157	0.3066	0.2881	0.2868	0.3306
2.0	0.2759	0.2763	0.2578	0.2545	0.2887
2.5	0.2447	0.2457	0.2382	0.2284	0.2557
3.0	0.2199	0.2211	0.2185	0.2074	0.2293
3.5	0.2019	0.2011	0.2007	0.1921	0.2083
4.0	0.1843	0.1840	0.1840	0.1806	0.1908
4.5	0.1684	0.1691	0.1682	0.1662	0.1750
5.0	0.1554	0.1558	0.1553	0.1543	0.1622
5.5	0.1443	0.1447	0.1443	0.1433	0.1504
6.0	0.1343	0.1343	0.1349	0.1337	0.1394
6.5	0.1244	0.1248	0.1252	0.1241	0.1304
7.0	0.1172	0.1177	0.1179	0.1172	0.1223
7.5	0.1100	0.1105	0.1107	0.1094	0.1150
8.0	0.1035	0.1037	0.1040	0.1033	0.1085
8.5	0.0983	0.0990	0.0995	0.0986	0.1028
9.0	0.0932	0.0935	0.0937	0.0931	0.0967
9.5	0.0878	0.0882	0.0886	0.0884	0.0922
10.0	0.0833	0.0836	0.0843	0.0841	0.0871
10.5					
11.0					
12.0					
P (in Hg)	242.01	244.01	244.41	245.01	245.81
T ₀ (°K)	324.89	344.56	362.32	381.24	340.88
ω	0.0052	0.0051	0.0051	0.0050	0.0102

Run	.010*2*10.5	.010*3*10.5	.015*1*10.5	.015*2*10.5	.015*3*10.5
x(in)	p/p ₀	p/p ₀	p/p ₀	p/p ₀	p/p ₀
0.5	0.3954	0.3980	0.4253	0.3957	0.3961
1.0	0.3330	0.3300	0.3952	0.3494	0.3303
1.5	0.3199	0.2880	0.3381	0.3334	0.2948
2.0	0.2873	0.2580	0.2963	0.2941	0.2819
2.5	0.2563	0.2405	0.2636	0.2621	0.2588
3.0	0.2299	0.2247	0.2377	0.2366	0.2339
3.5	0.2104	0.2074	0.2141	0.2157	0.2143
4.0	0.1916	0.1909	0.1967	0.1973	0.1963
4.5	0.1761	0.1758	0.1812	0.1817	0.1814
5.0	0.1626	0.1625	0.1658	0.1675	0.1675
5.5	0.1502	0.1500	0.1541	0.1552	0.1555
6.0	0.1400	0.1402	0.1436	0.1440	0.1444
6.5	0.1304	0.1304	0.1333	0.1337	0.1344
7.0	0.1228	0.1225	0.1256	0.1258	0.1261
7.5	0.1157	0.1156	0.1188	0.1187	0.1189
8.0	0.1086	0.1082	0.1113	0.1114	0.1116
8.5	0.1033	0.1035	0.1063	0.1068	0.1064
9.0	0.0973	0.0974	0.1002	0.1005	0.1005
9.5	0.0927	0.0929	0.0951	0.0954	0.0952
10.0	0.0878	0.0882	0.0903	0.0908	0.0909
10.5					
11.0					
12.0					
P (in Hg)	245.11	245.00	247.61	246.91	244.81
T ₀ (°K)	362.87	385.21	354.87	368.28	382.02
ω	0.0100	0.0102	0.0151	0.0150	0.0154

Table F.3. Experimental Static Pressure Ratios, Nozzle Flow Conditions

Run	.005*1* 8.5	.005*2* 8.5	.005*3* 8.5	.005*4* 8.5	.010*1* 8.5
x(in)	p/p ₀	p/p ₀	p/p ₀	p/p ₀	p/p ₀
0.5	0.4135	0.3941	0.3955	0.3960	0.4751
1.0	0.3606	0.3305	0.3281	0.3285	0.3886
1.5	0.3105	0.3084	0.2869	0.2870	0.3322
2.0	0.2715	0.2733	0.2561	0.2552	0.2900
2.5	0.2411	0.2429	0.2357	0.2282	0.2569
3.0	0.2167	0.2180	0.2165	0.2068	0.2287
3.5	0.1991	0.1994	0.1990	0.1913	0.2090
4.0	0.1819	0.1828	0.1826	0.1801	0.1910
4.5	0.1660	0.1668	0.1668	0.1655	0.1752
5.0	0.1526	0.1540	0.1539	0.1533	0.1595
5.5	0.1423	0.1428	0.1432	0.1429	0.1501
6.0	0.1319	0.1324	0.1333	0.1325	0.1394
6.5	0.1226	0.1235	0.1237	0.1238	0.1303
7.0	0.1150	0.1161	0.1166	0.1165	0.1222
7.5	0.1084	0.1090	0.1097	0.1095	0.1150
8.0	0.1015	0.1024	0.1029	0.1030	0.1079
8.5					
9.0					
9.5					
10.0					
10.5					
11.0					
12.0					
P (in Hg)	241.88	241.31	240.21	240.81	238.31
T ₀ (°K)	324.78	342.51	363.56	381.92	339.31
ω	0.0048	0.0050	0.0044	0.0046	0.0102

Run	.010*2* 8.5	.010*3* 8.5	.015*1* 8.5	.015*2* 8.5	.015*3* 8.5
x(in)	p/p ₀	p/p ₀	p/p ₀	p/p ₀	p/p ₀
0.5	0.3950	0.3961	0.4019	0.3944	0.3924
1.0	0.3320	0.3303	0.3905	0.3364	0.3287
1.5	0.3175	0.2883	0.3401	0.3279	0.2912
2.0	0.2870	0.2581	0.2976	0.2952	0.2788
2.5	0.2560	0.2380	0.2655	0.2628	0.2579
3.0	0.2301	0.2247	0.2390	0.2377	0.2340
3.5	0.2101	0.2078	0.2174	0.2168	0.2142
4.0	0.1914	0.1911	0.1980	0.1984	0.1961
4.5	0.1764	0.1760	0.1823	0.1827	0.1811
5.0	0.1622	0.1620	0.1680	0.1687	0.1672
5.5	0.1501	0.1499	0.1556	0.1559	0.1551
6.0	0.1401	0.1401	0.1444	0.1448	0.1437
6.5	0.1330	0.1301	0.1345	0.1350	0.1345
7.0	0.1226	0.1228	0.1261	0.1268	0.1262
7.5	0.1155	0.1155	0.1194	0.1197	0.1197
8.0	0.1084	0.1084	0.1121	0.1122	0.1116
8.5					
9.0					
9.5					
10.0					
10.5					
11.0					
12.0					
P (in Hg)	239.91	239.51	237.91	239.01	240.21
T ₀ (°K)	362.08	385.09	354.98	369.34	380.88
ω	0.0098	0.0104	0.0156	0.0153	0.0155

Table F.3. Experimental Static Pressure Ratios, Nozzle Flow Conditions

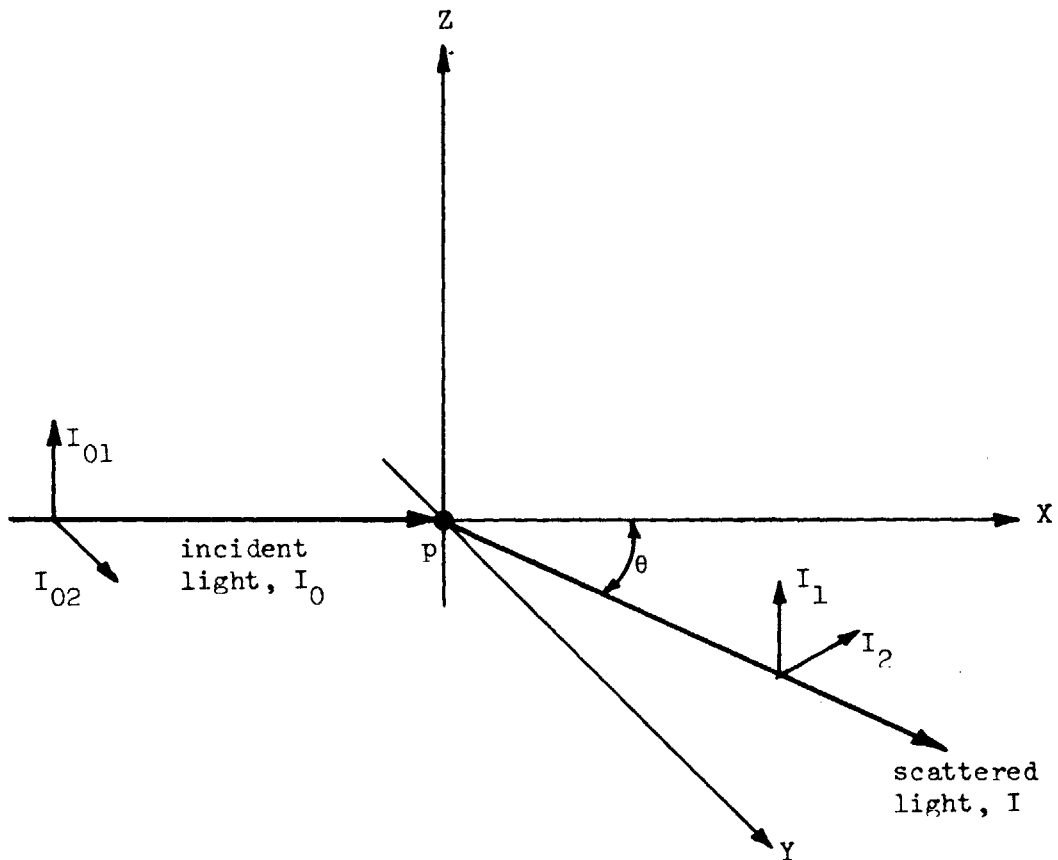
Run	.005*1* 6.5	.005*2* 6.5	.005*3* 6.5	.005*4* 6.5	.010*1* 6.5
x(in)	p/p ₀	p/p ₀	p/p ₀	p/p ₀	p/p ₀
0.5	0.4091	0.3908	0.3908	0.3931	0.4355
1.0	0.3589	0.3306	0.3245	0.3266	0.3827
1.5	0.3094	0.3085	0.2845	0.2844	0.3261
2.0	0.2703	0.2720	0.2539	0.2523	0.2847
2.5	0.2397	0.2414	0.2349	0.2261	0.2528
3.0	0.2163	0.2172	0.2164	0.2068	0.2273
3.5	0.1990	0.1991	0.1987	0.1873	0.2058
4.0	0.1818	0.1824	0.1822	0.1795	0.1897
4.5	0.1655	0.1666	0.1661	0.1650	0.1730
5.0	0.1523	0.1530	0.1532	0.1533	0.1606
5.5	0.1415	0.1432	0.1428	0.1430	0.1485
6.0	0.1316	0.1330	0.1330	0.1319	0.1380
6.5					
7.0					
7.5					
8.0					
8.5					
9.0					
9.5					
10.0					
10.5					
11.0					
12.0					
P ₀ (in Hg)	239.13	239.91	239.91	238.33	236.83
T ₀ (°K)	325.59	341.90	363.52	380.46	341.49
ω ₀	0.0047	0.0047	0.0046	0.0045	0.0098

Run	.010*2* 6.5	.010*3* 6.5	.015*1* 6.5	.015*2* 6.5	.015*3* 6.5
x(in)	p/p ₀	p/p ₀	p/p ₀	p/p ₀	p/p ₀
0.5	0.3914	0.3941	0.4413	0.3917	0.3913
1.0	0.3279	0.3282	0.3950	0.3373	0.3266
1.5	0.3131	0.2853	0.3373	0.3265	0.2905
2.0	0.2839	0.2544	0.2946	0.2918	0.2730
2.5	0.2527	0.2353	0.2618	0.2603	0.2560
3.0	0.2279	0.2226	0.2359	0.2353	0.2325
3.5	0.2081	0.2071	0.2153	0.2147	0.2130
4.0	0.1899	0.1896	0.1963	0.1968	0.1958
4.5	0.1742	0.1745	0.1797	0.1802	0.1795
5.0	0.1603	0.1604	0.1664	0.1667	0.1659
5.5	0.1494	0.1492	0.1536	0.1545	0.1535
6.0	0.1380	0.1387	0.1435	0.1431	0.1432
6.5					
7.0					
7.5					
8.0					
8.5					
9.0					
9.5					
10.0					
10.5					
11.0					
12.0					
P ₀ (in Hg)	237.53	237.73	237.53	237.73	238.63
T ₀ (°K)	362.11	385.09	352.62	368.92	381.28
ω ₀	0.0095	0.0094	0.0151	0.0148	0.0149

Table F.3. Experimental Static Pressure Ratios, Nozzle Flow Conditions

Run	.005*1* 4.5	.005*2* 4.5	.005*3* 4.5	.005*4* 4.5	.010*1* 4.5
x(in)	p/p ₀	p/p ₀	p/p ₀	p/p ₀	p/p ₀
0.5	0.4111	0.3926	0.3899	0.3869	0.4661
1.0	0.3631	0.3299	0.3258	0.3276	0.3855
1.5	0.3122	0.3083	0.2860	0.2852	0.3282
2.0	0.2732	0.2738	0.2559	0.2545	0.2866
2.5	0.2420	0.2424	0.2361	0.2264	0.2541
3.0	0.2182	0.2185	0.2176	0.2080	0.2290
3.5	0.2001	0.2008	0.2001	0.1929	0.2084
4.0	0.1828	0.1836	0.1835	0.1807	0.1905
4.5					
5.0					
5.5					
6.0					
6.5					
7.0					
7.5					
8.0					
8.5					
9.0					
9.5					
10.0					
10.5					
11.0					
12.0					
P (in Hg)	237.41	238.31	237.41	238.31	237.11
T (°K)	325.13	342.97	363.39	380.86	341.26
ω	0.0045	0.0045	0.0045	0.0045	0.0100

Run	.010*2* 4.5	.010*3* 4.5	.015*1* 4.5	.015*2* 4.5	.015*3* 4.5
x(in)	p/p ₀	p/p ₀	p/p ₀	p/p ₀	p/p ₀
0.5	0.3866	0.3869	0.4090	0.3870	0.3859
1.0	0.3360	0.3305	0.3970	0.3412	0.3299
1.5	0.3244	0.2858	0.3406	0.3309	0.2919
2.0	0.2866	0.2560	0.2963	0.2921	0.2825
2.5	0.2549	0.2399	0.2638	0.2615	0.2578
3.0	0.2297	0.2252	0.2386	0.2366	0.2344
3.5	0.2099	0.2073	0.2174	0.2164	0.2142
4.0	0.1918	0.1903	0.1983	0.1983	0.1953
4.5					
5.0					
5.5					
6.0					
6.5					
7.0					
7.5					
8.0					
8.5					
9.0					
9.5					
10.0					
10.5					
11.0					
12.0					
P (in Hg)	238.01	238.31	238.31	237.11	237.41
T (°K)	350.39	384.70	354.22	369.26	387.86
ω	0.0100	0.0098	0.0147	0.0150	0.0149



p = scattering particle

xy = plane of observation, contains the incident and scattered direction vectors.

θ = angle of observation, lies in plane xy and is measured from the forward direction of the incident light.

I_{01} , I_{11} = perpendicular components of the incident and scattered light, respectively; lie in z direction, perpendicular to plane xy .

I_{02} , I_{12} = parallel components of the incident and scattered light; lie in the plane xy and are perpendicular to their respective direction vectors.

Figure 1. Definition of perpendicular and parallel components of scattered and incident light; plane of observation.

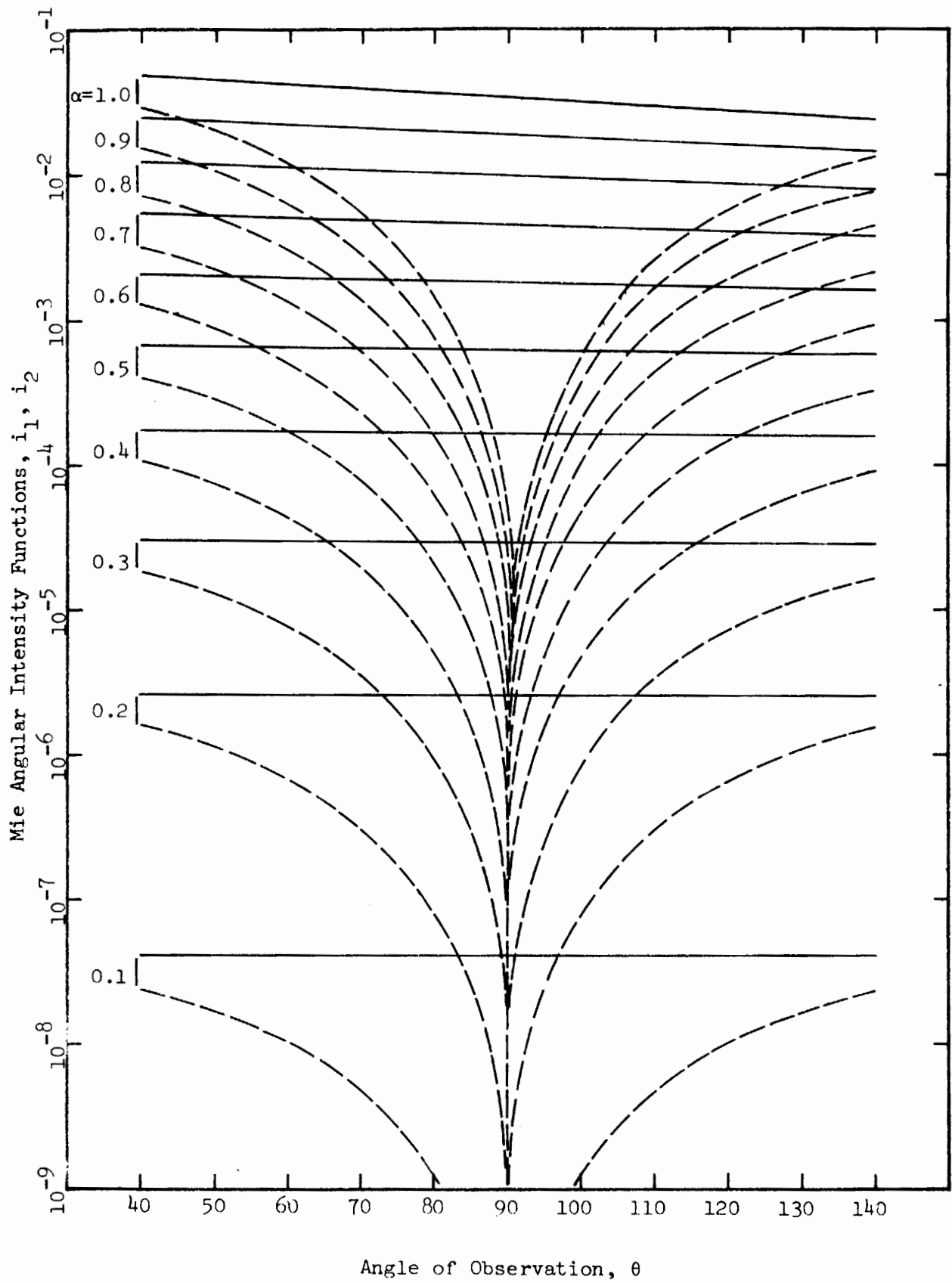


Figure 2(a). Angular intensity functions, i_1, i_2 , vs angle of observation, θ ; $0.1 < \alpha < 1.0$, $m = 1.33$; — perpendicular component, --- parallel component.

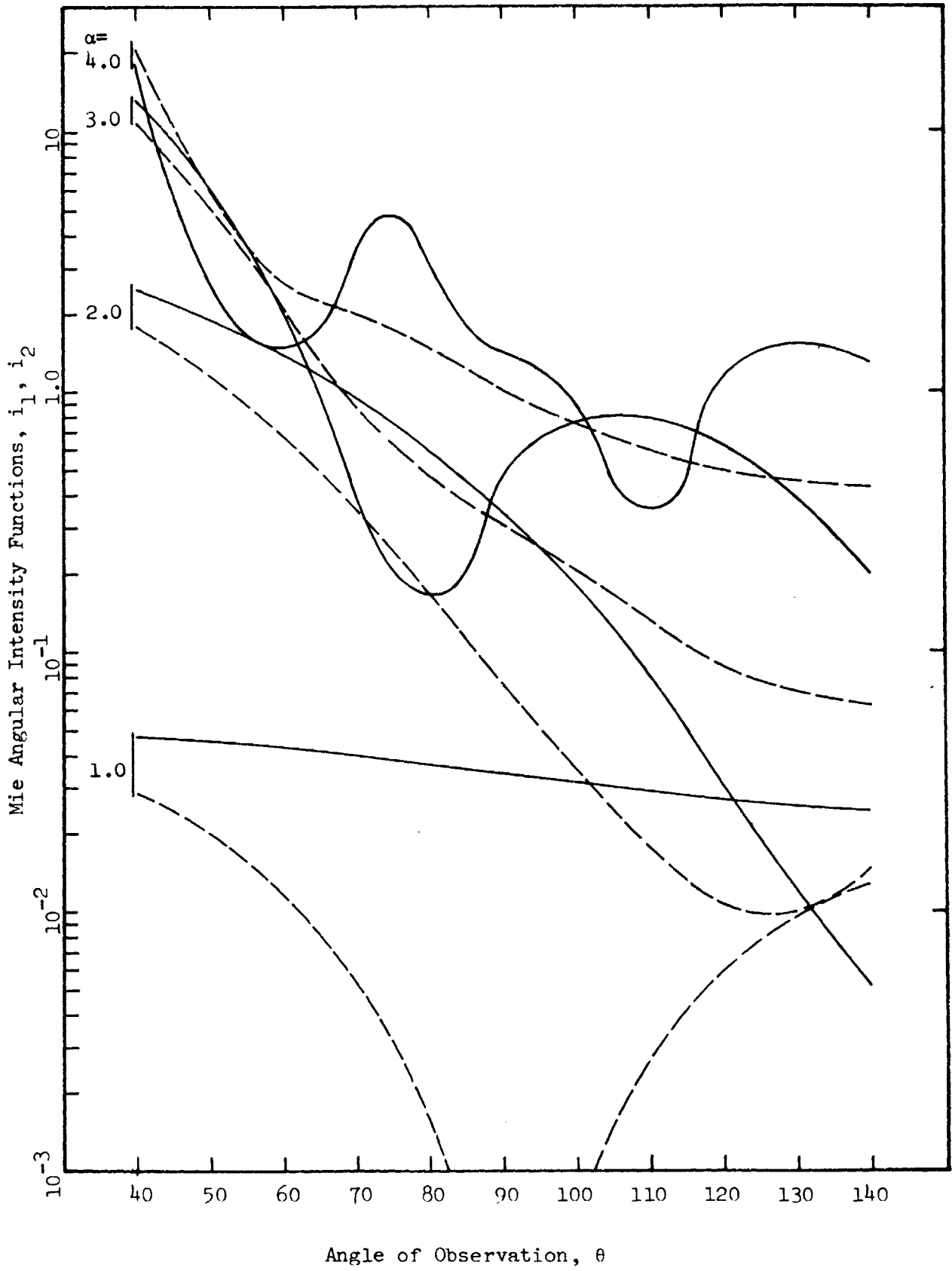


Figure 2(b). Angular intensity functions, i_1, i_2 vs angle of observation
 $1 < \alpha < 4, m = 1.33$ i_1 ———, i_2 - - - -

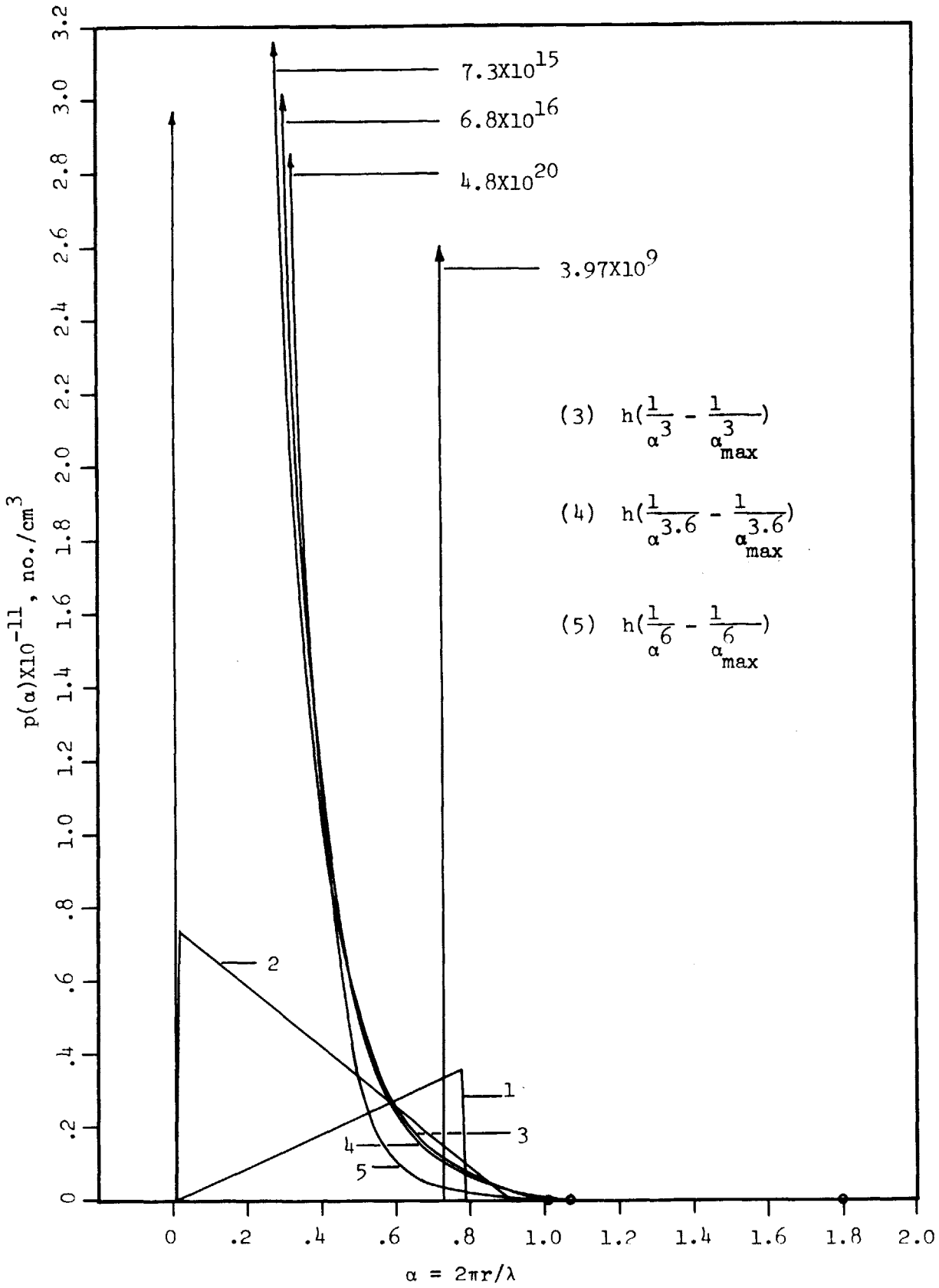


Figure 3(a). Distribution functions, $p(\alpha)$, satisfying light scattering data for $\omega_o = .015$, $(P/P_o)_i = .30$, distance from throat = 4.5 in.

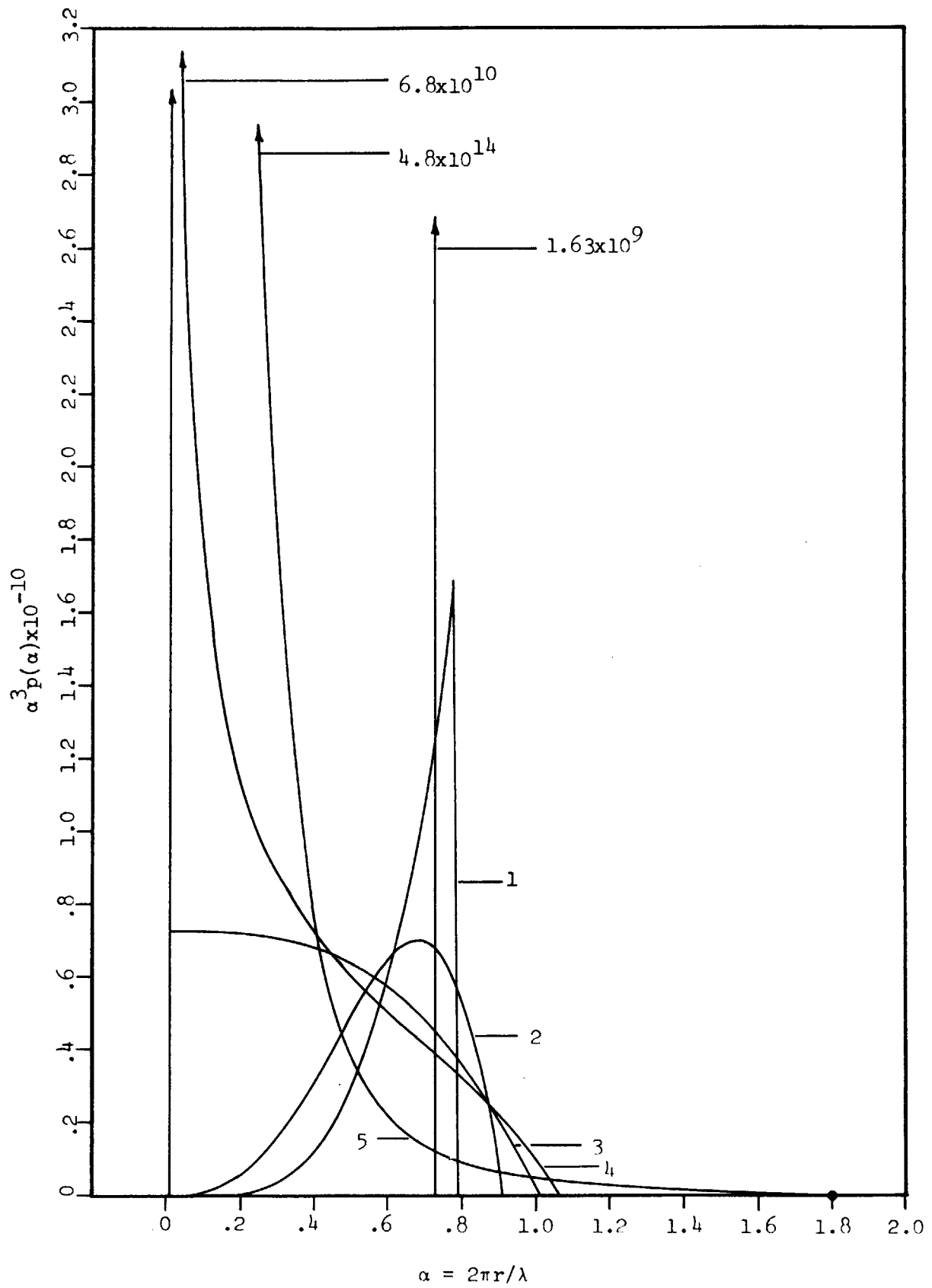


Figure 3(b). Mass distribution, $\alpha^3 p(\alpha)$

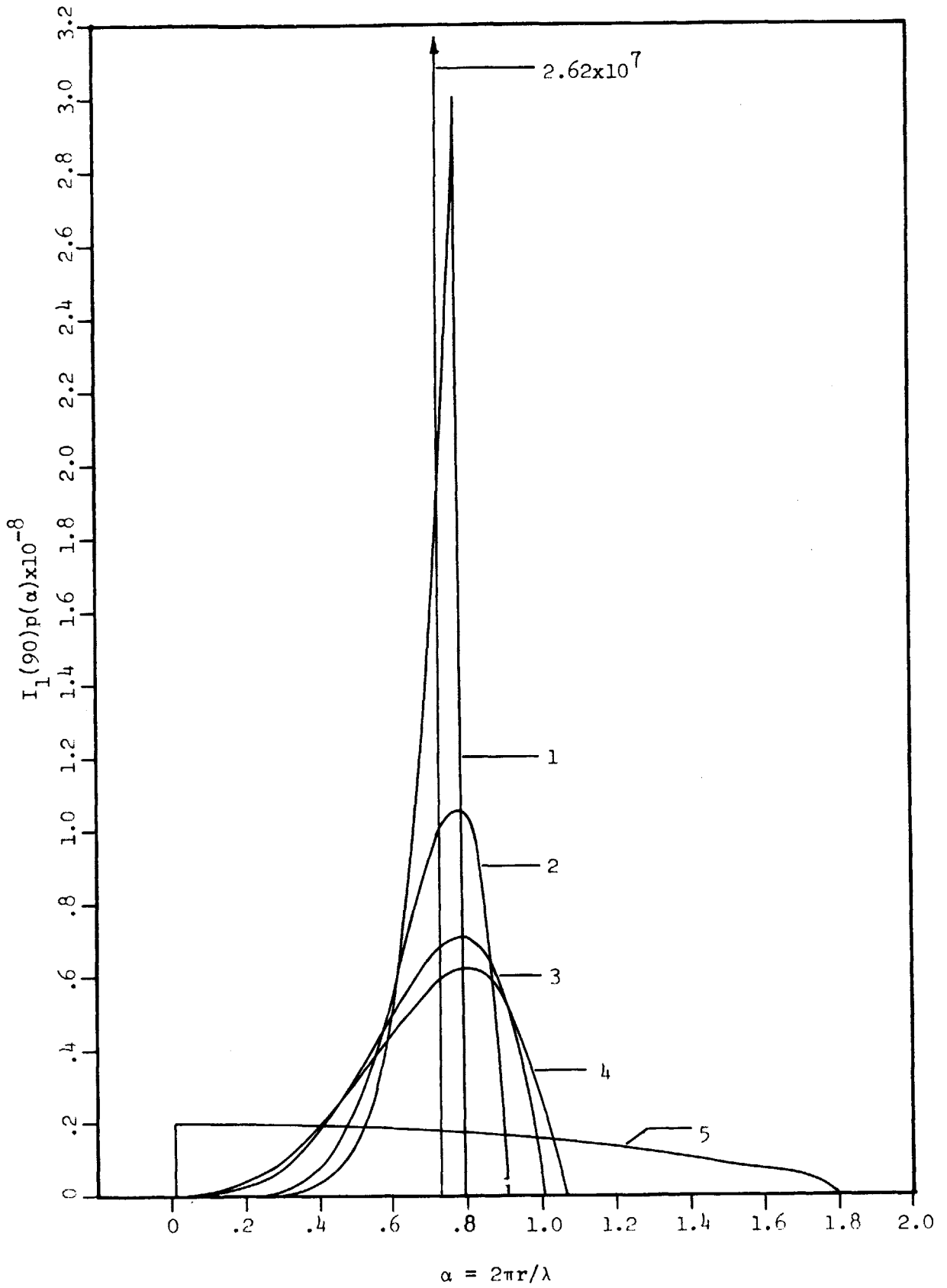


Figure 3(c). Scattered intensity distributions, $I_1(90^\circ)p(\alpha)$

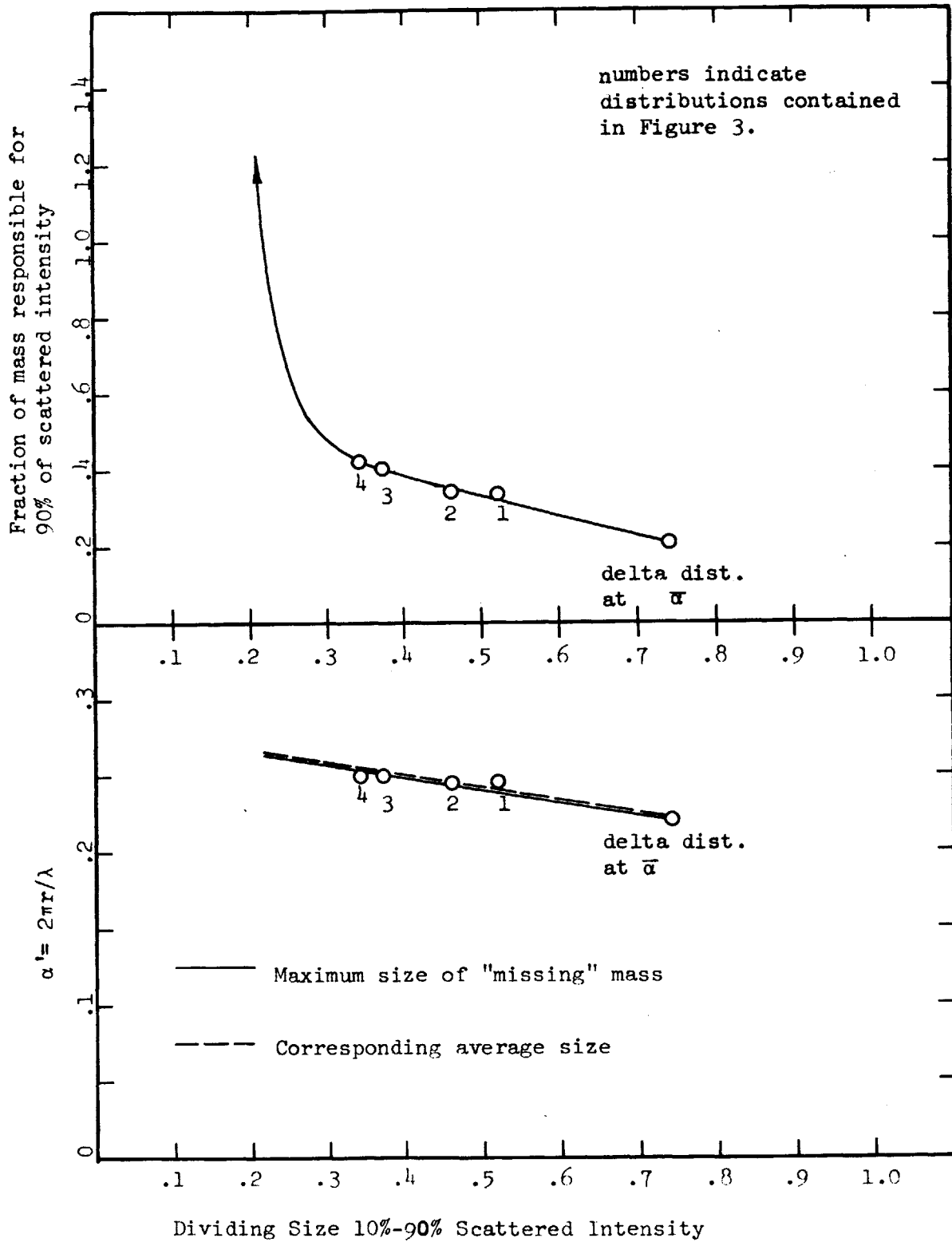


Figure 4. Fraction of mass responsible for 90% of scattered light vs. dividing size, 10-90% scattered intensity

Figure 5. Maximum average size vs. dividing size, 10-90% scattered intensity

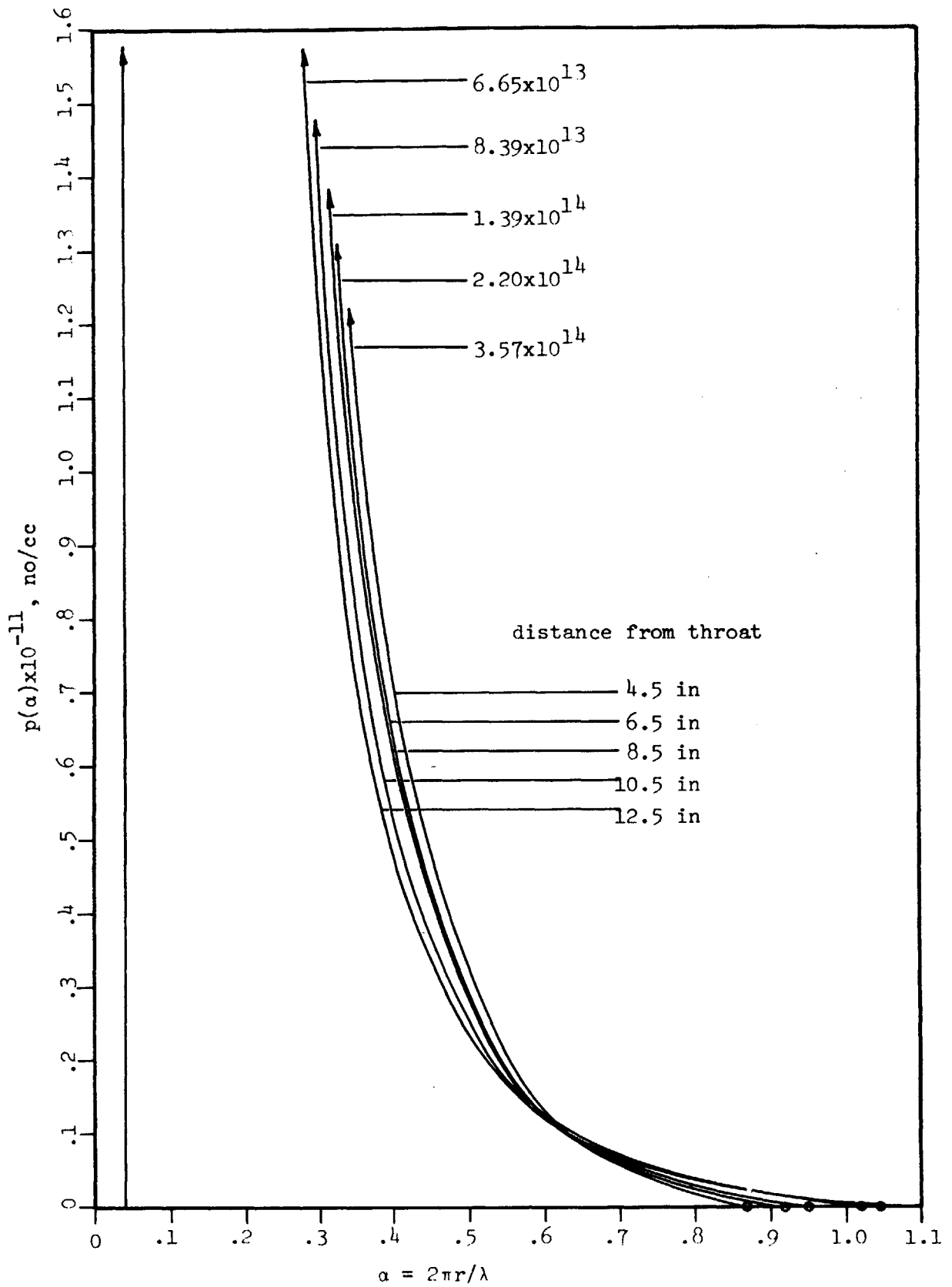


Figure 6. Particle size distribution vs. distance from throat; assumed minimum size of $\alpha=0.04$, $\omega_o = .010$, $(P/P_o)_i = 0.26$

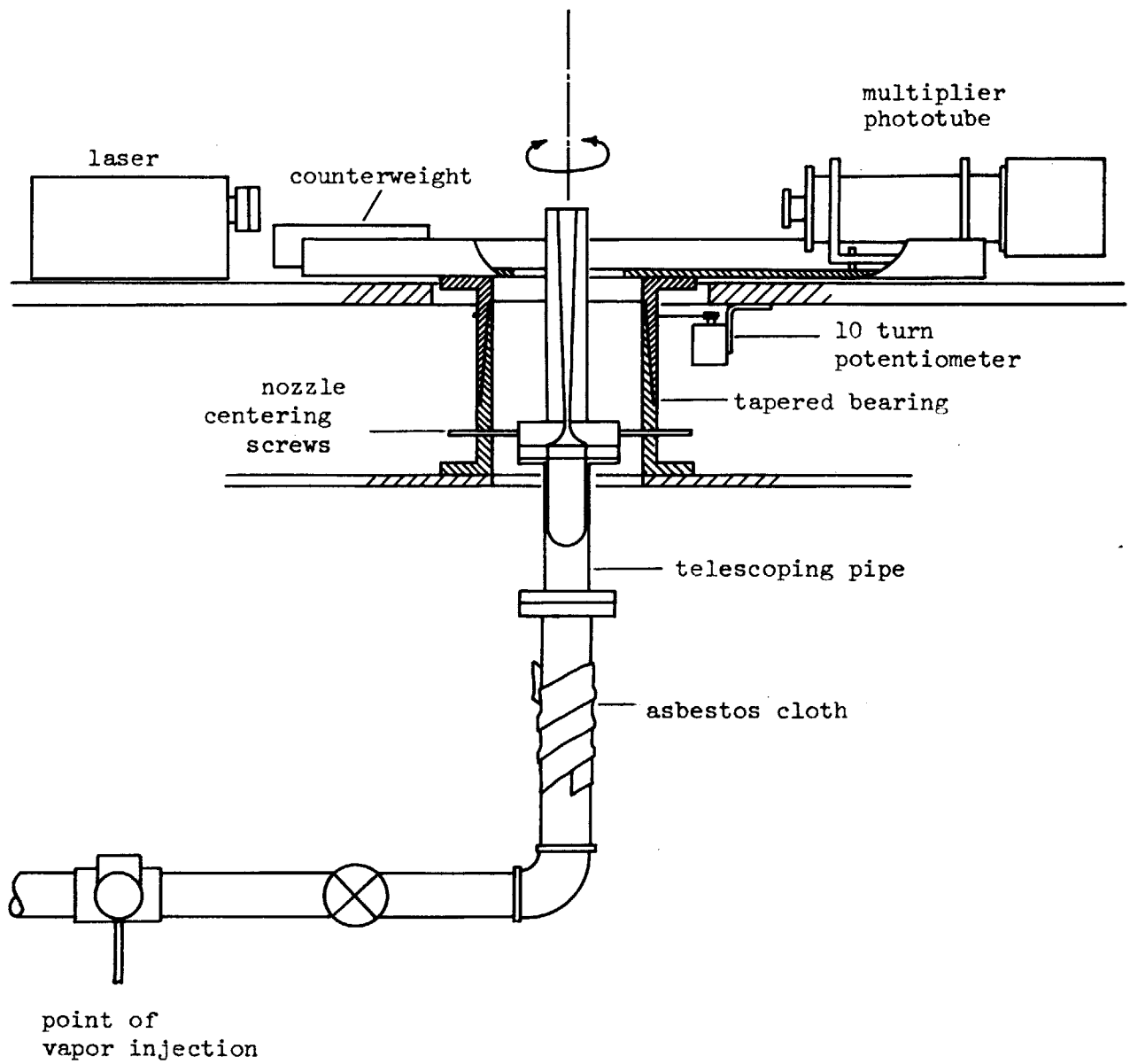


Figure 7. Layout of experimental apparatus (1)

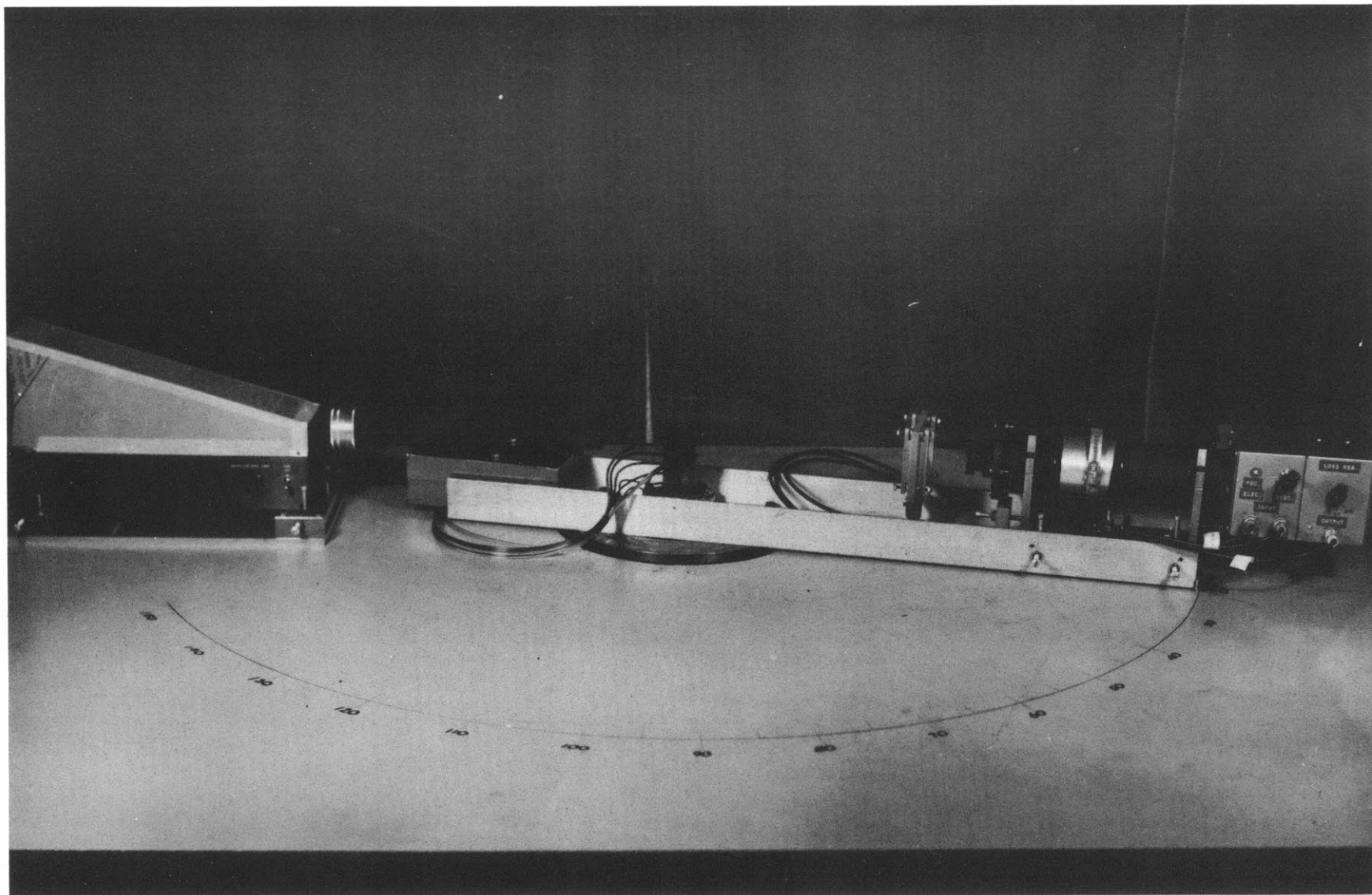


Figure 8. Layout of experimental apparatus(2)

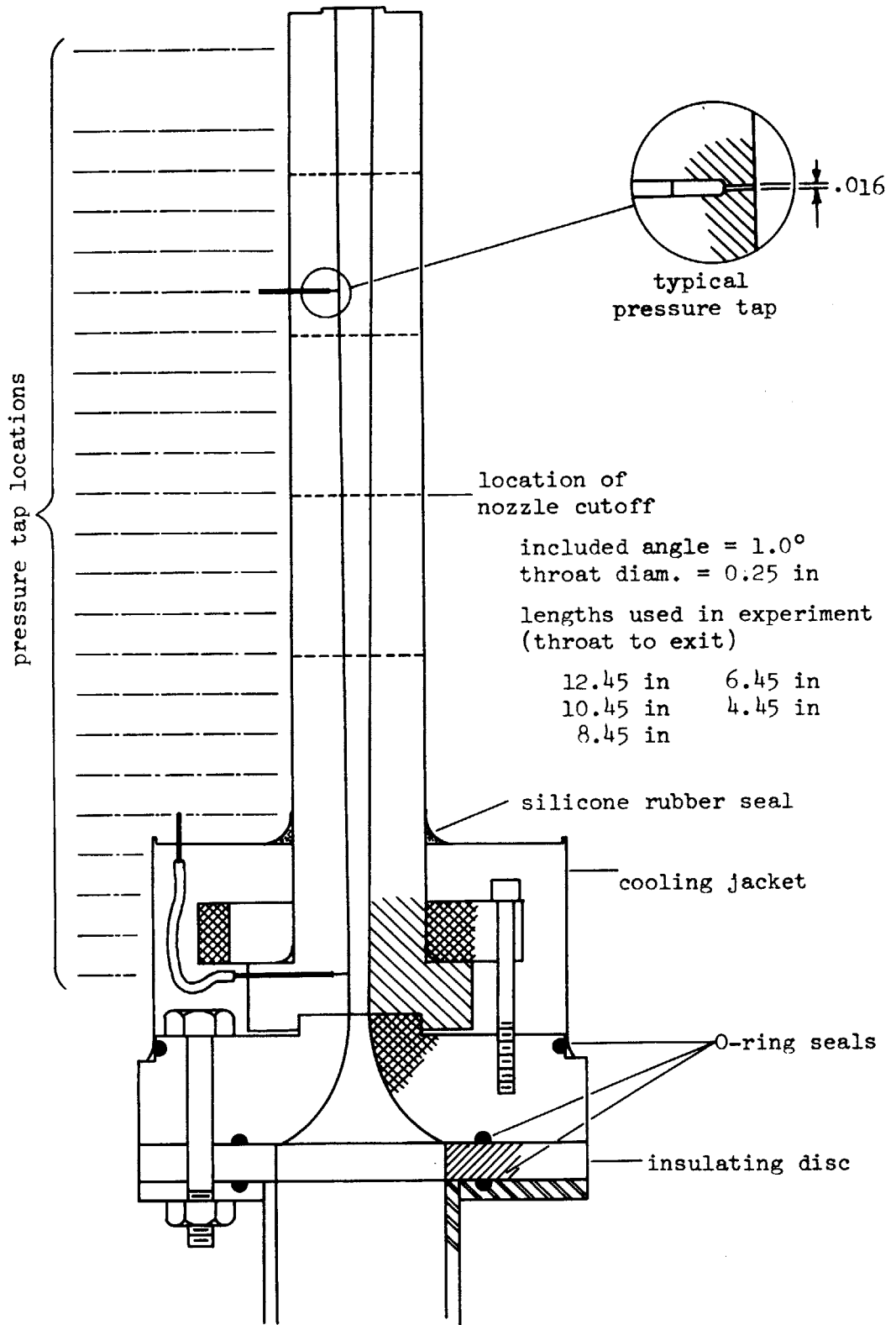


Figure 9. Details of nozzle construction

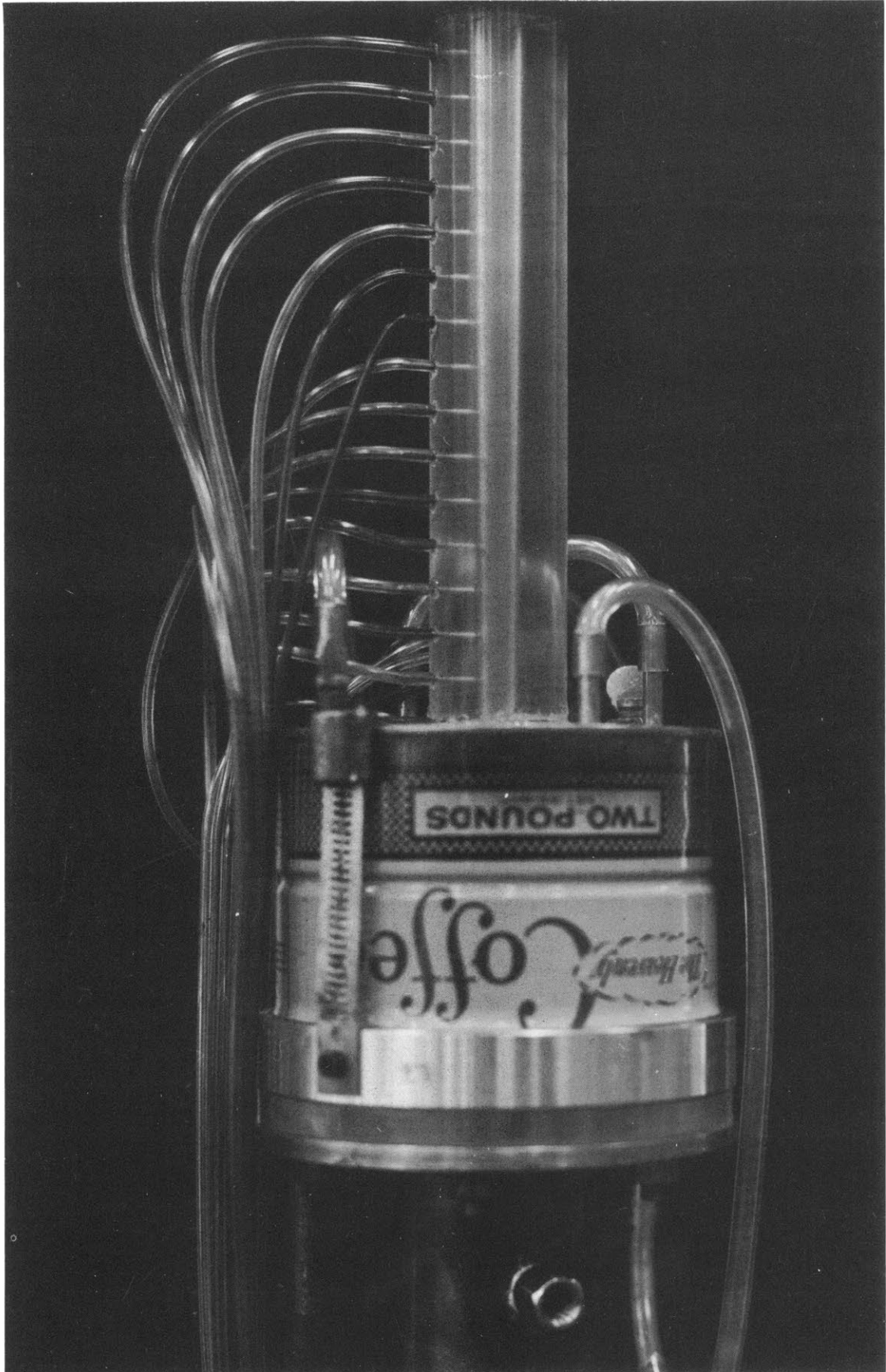


Figure 10. External view of nozzle

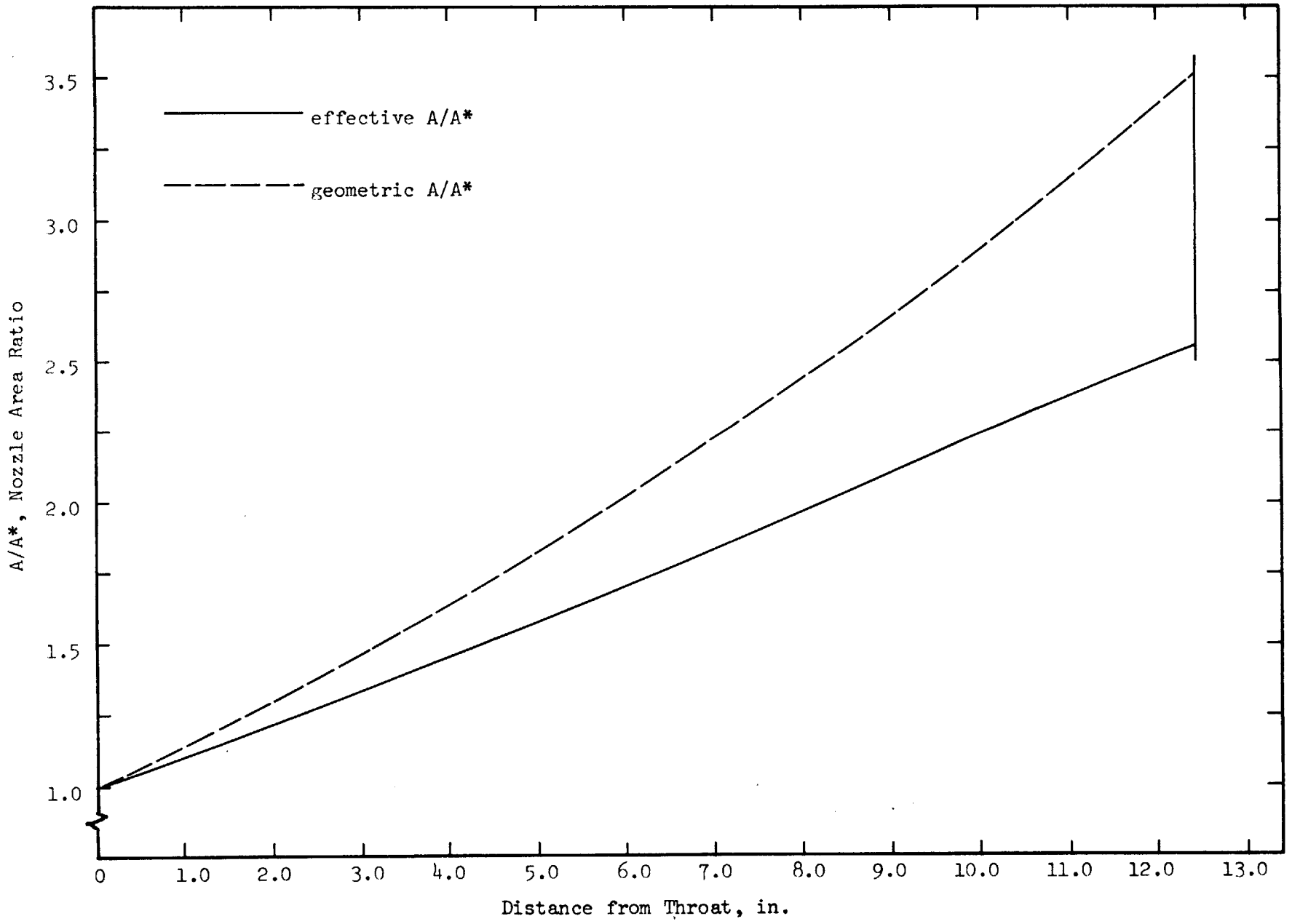


Figure 11. Nozzle area ratio vs. distance from throat

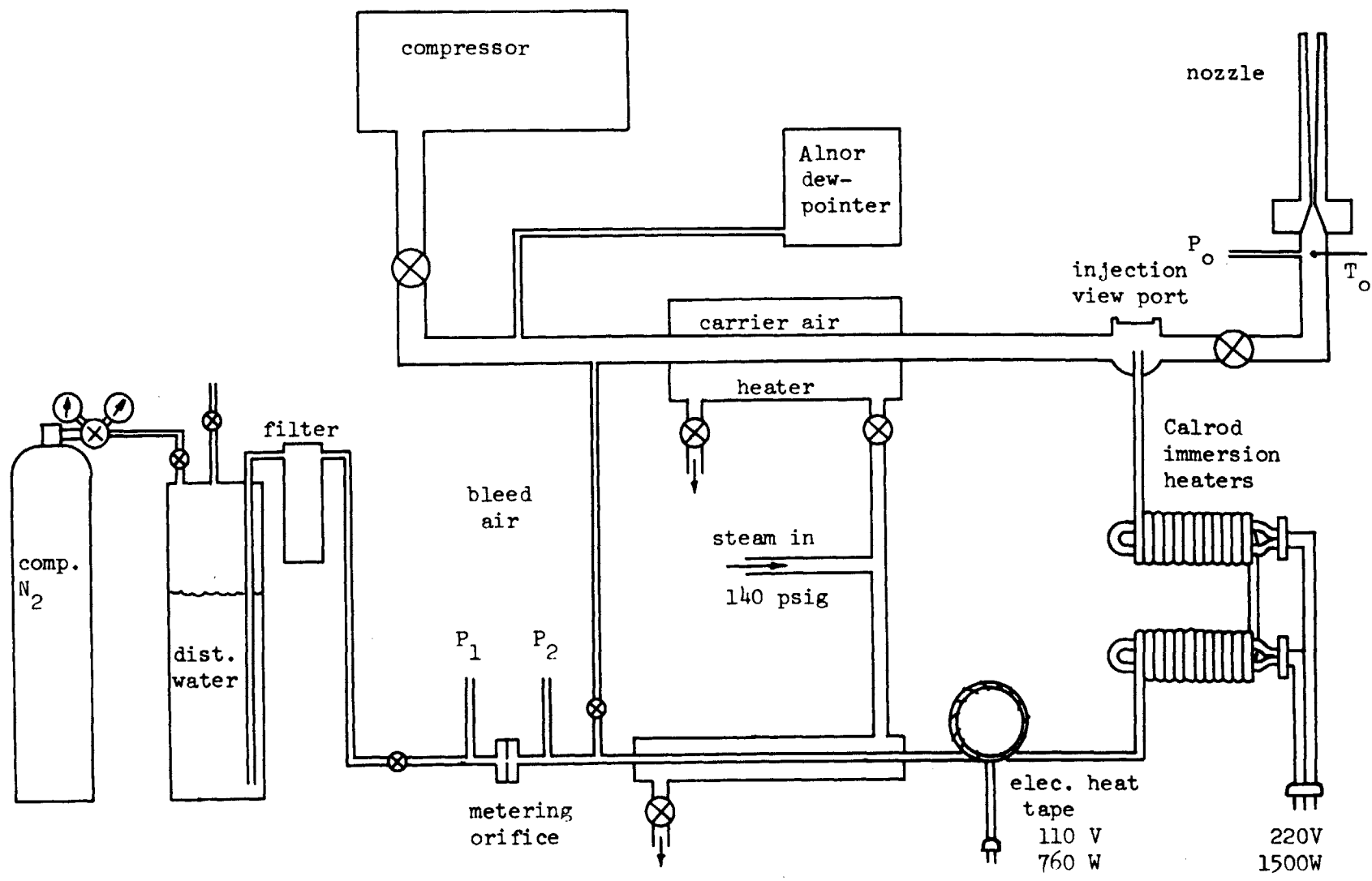


Figure 12. Schematic of vapor injection apparatus

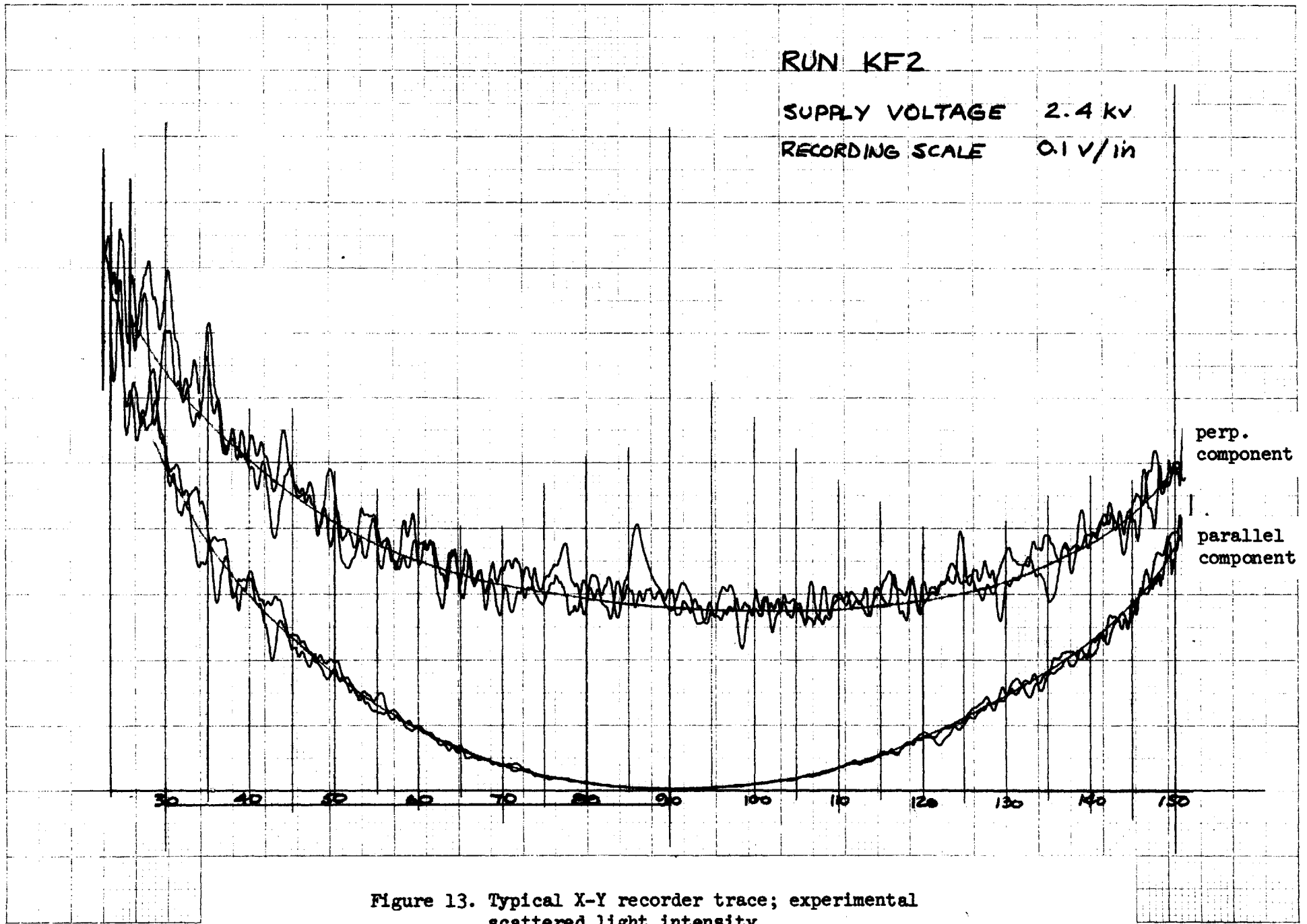


Figure 13. Typical X-Y recorder trace; experimental scattered light intensity

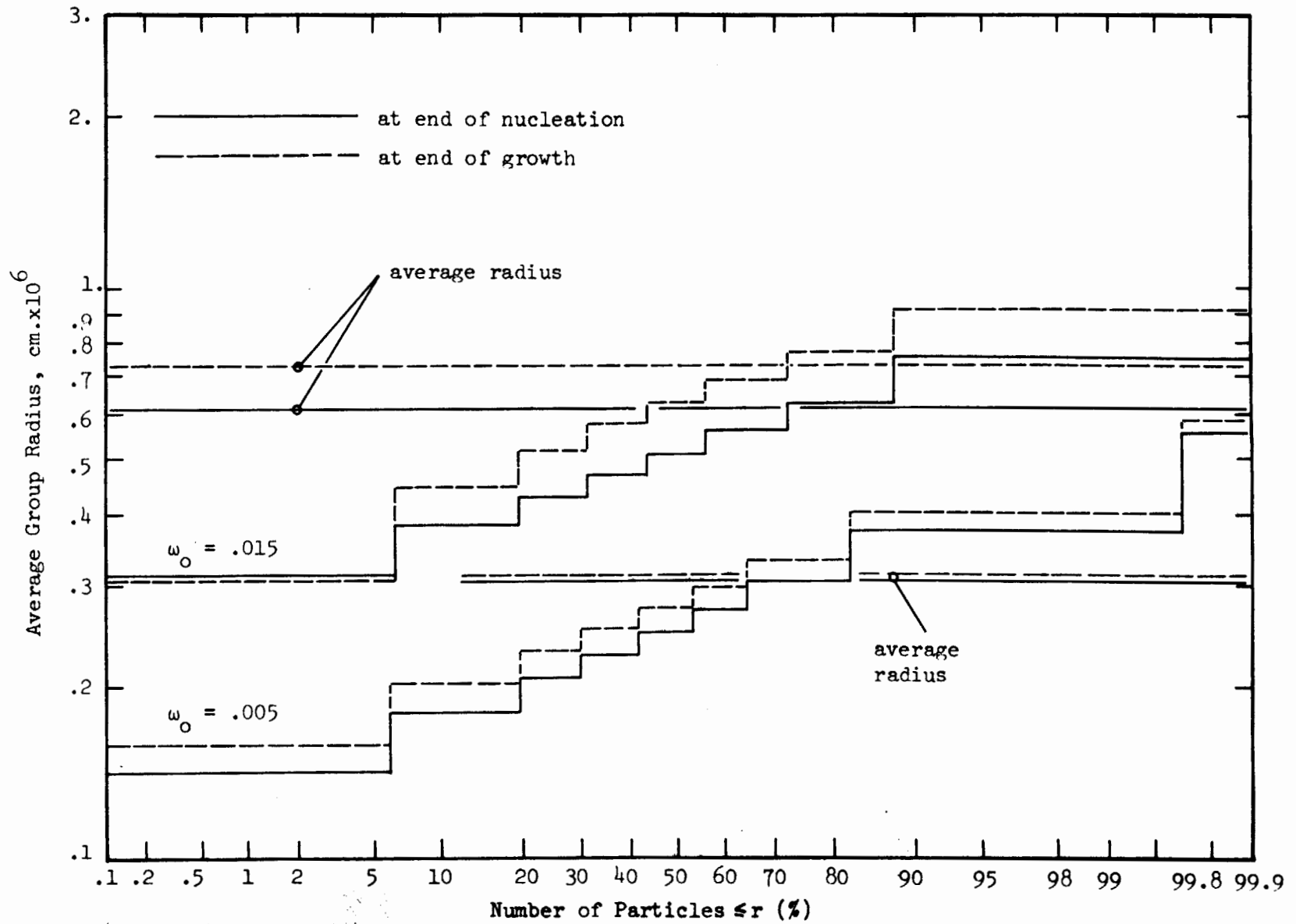


Figure 14. Number of particles $\leq r$ vs. average group radius for water vapor in air

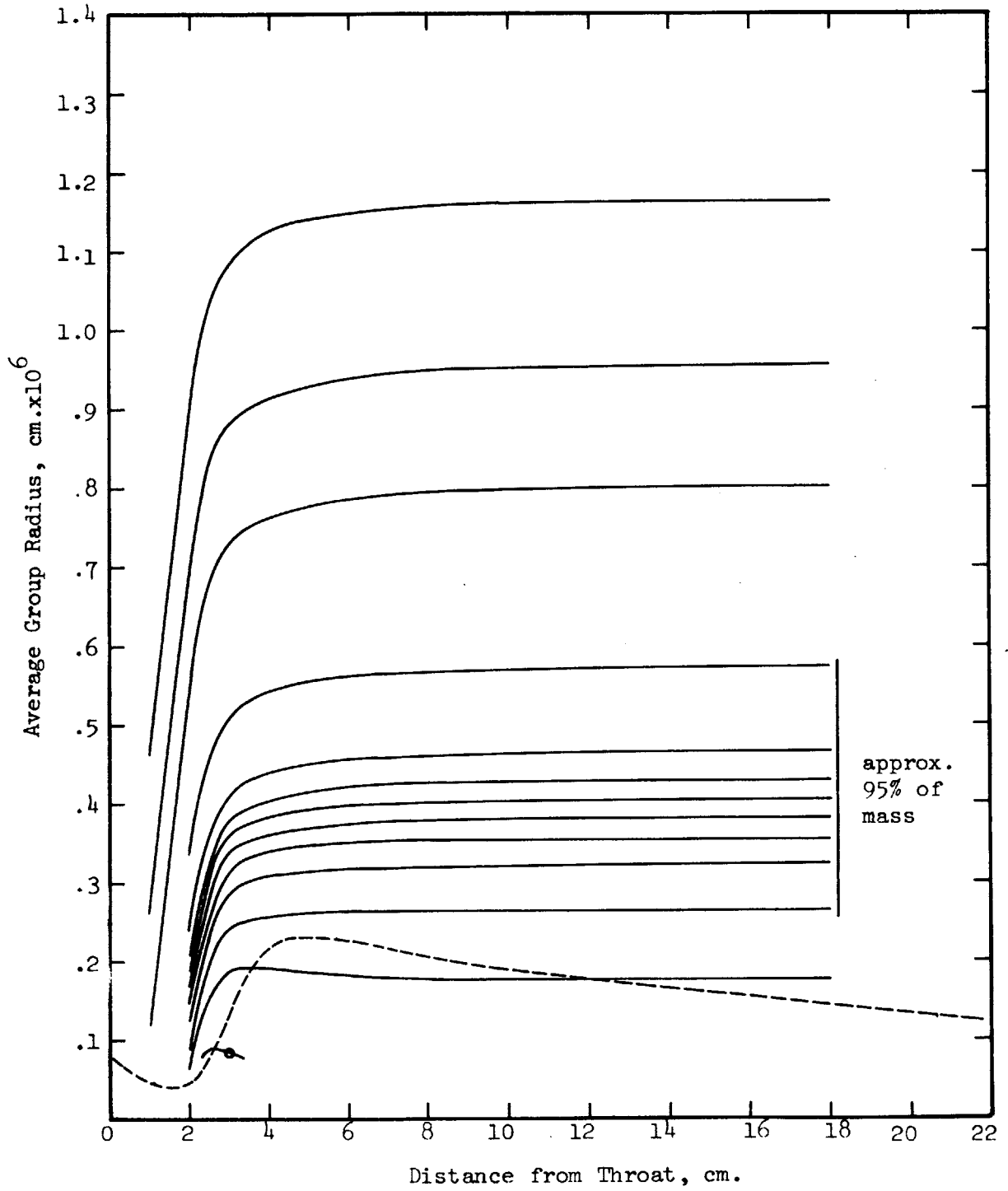


Figure 15. Growth history of group radii and their relation to the critical radius

—— group radius, - - - - - critical radius

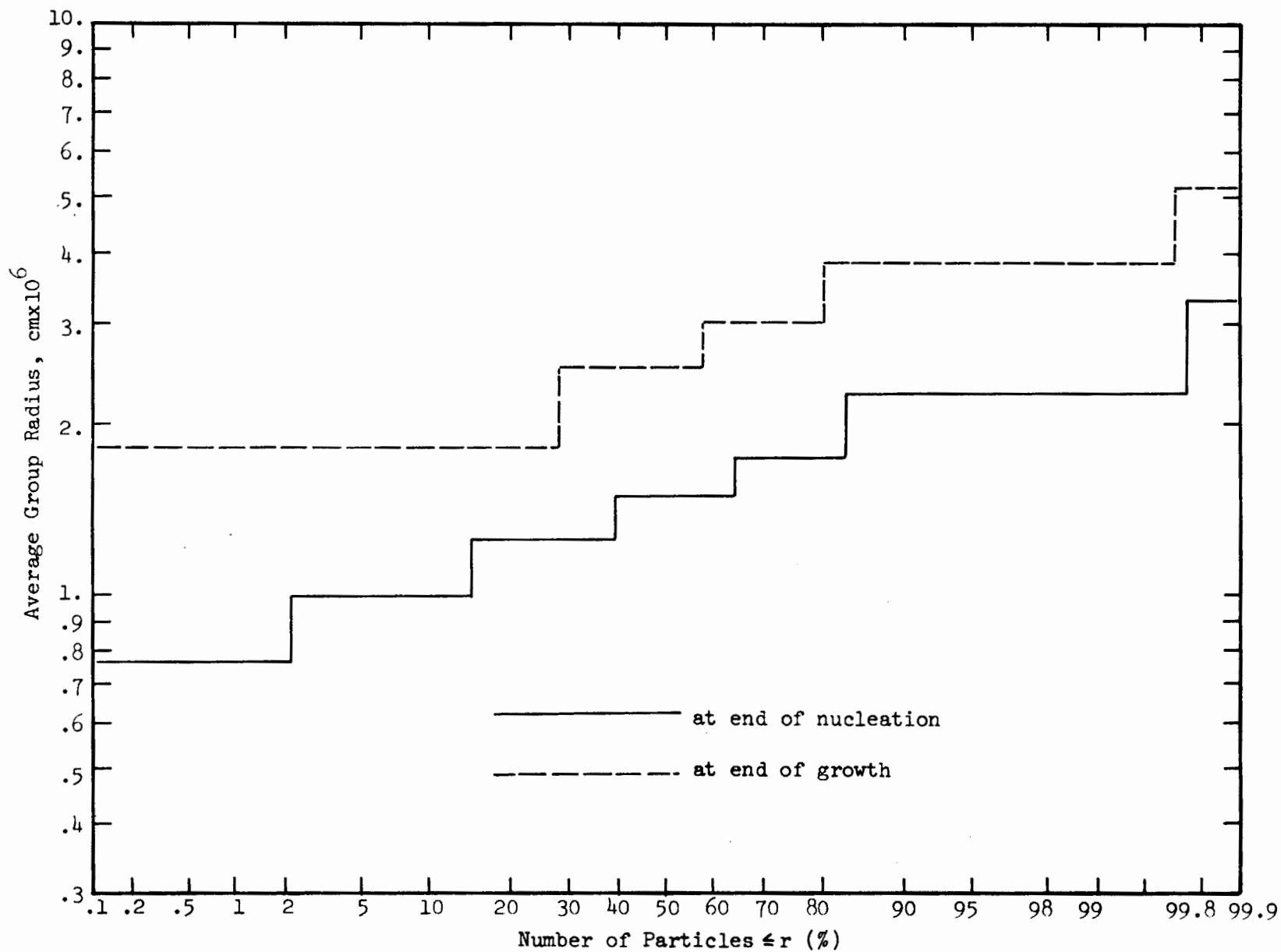


Figure 16. Number of particles $\leq r$ vs. average group radius for pure water vapor

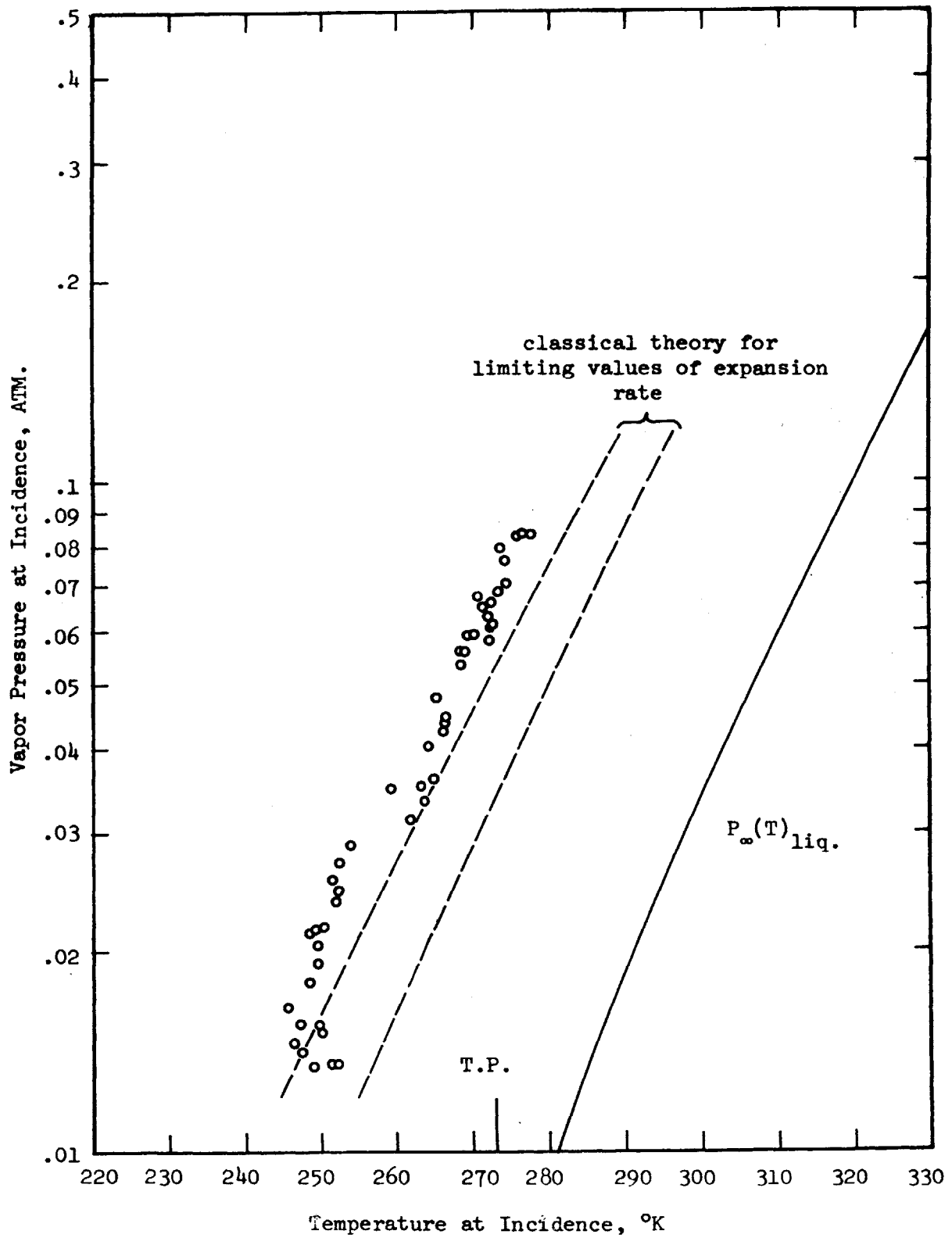


Figure 17. Vapor pressure and temperature at incidence of condensation

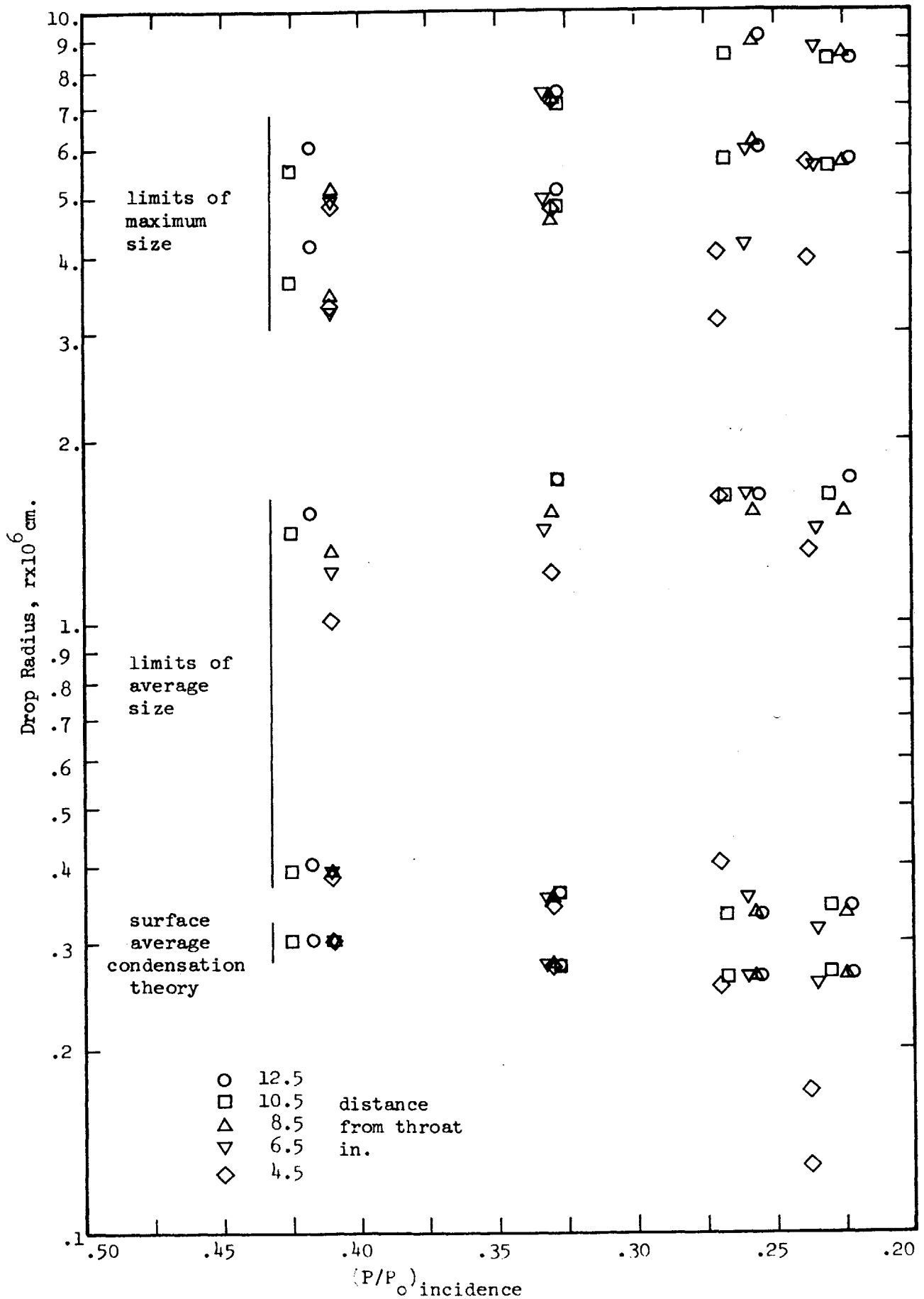


Figure 18(a). Maximum and average droplet size from light scattering measurements; $\omega_0 = .005$.

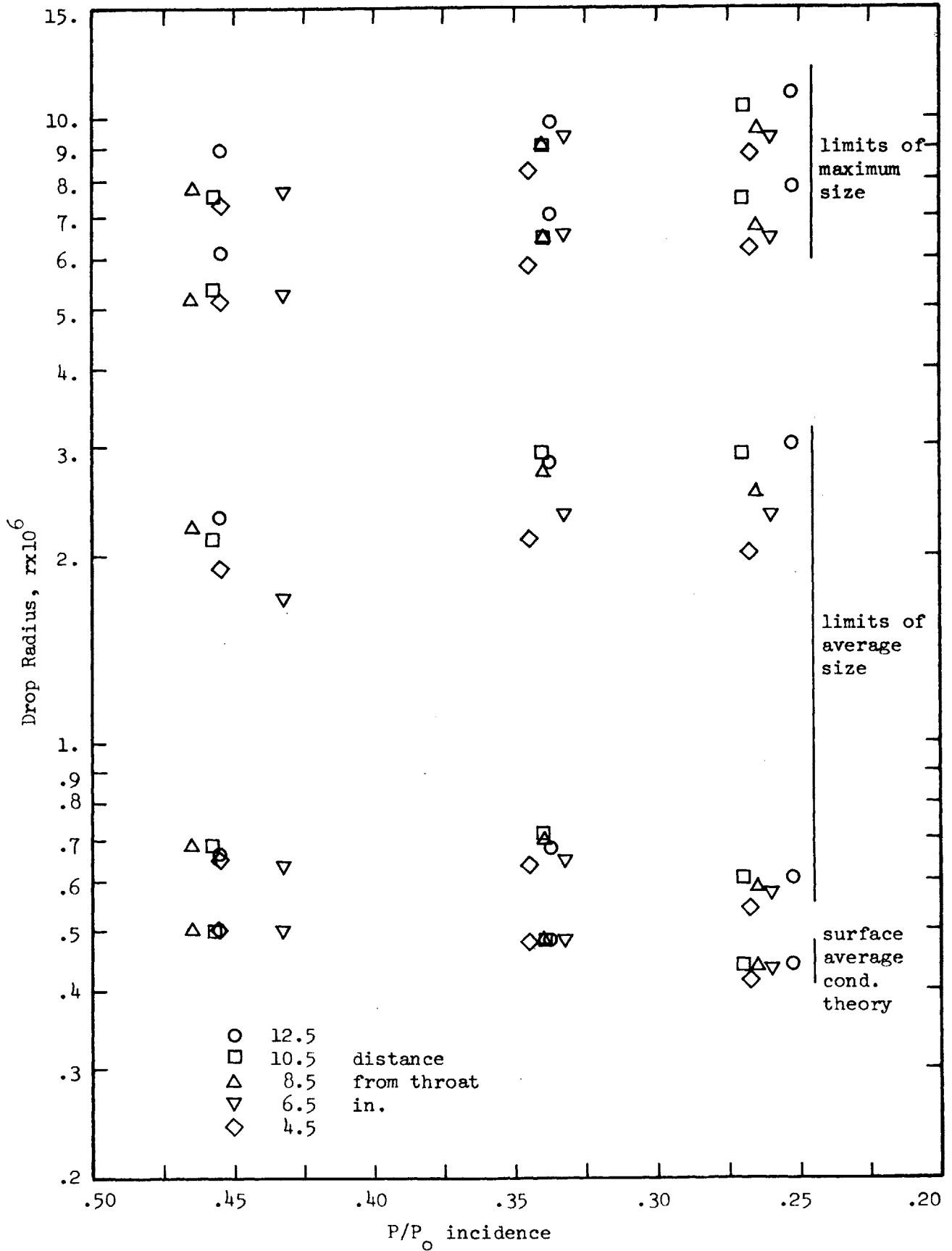


Figure 18(b). Maximum and average droplet size from light scattering measurements; $\omega_0 = .010$

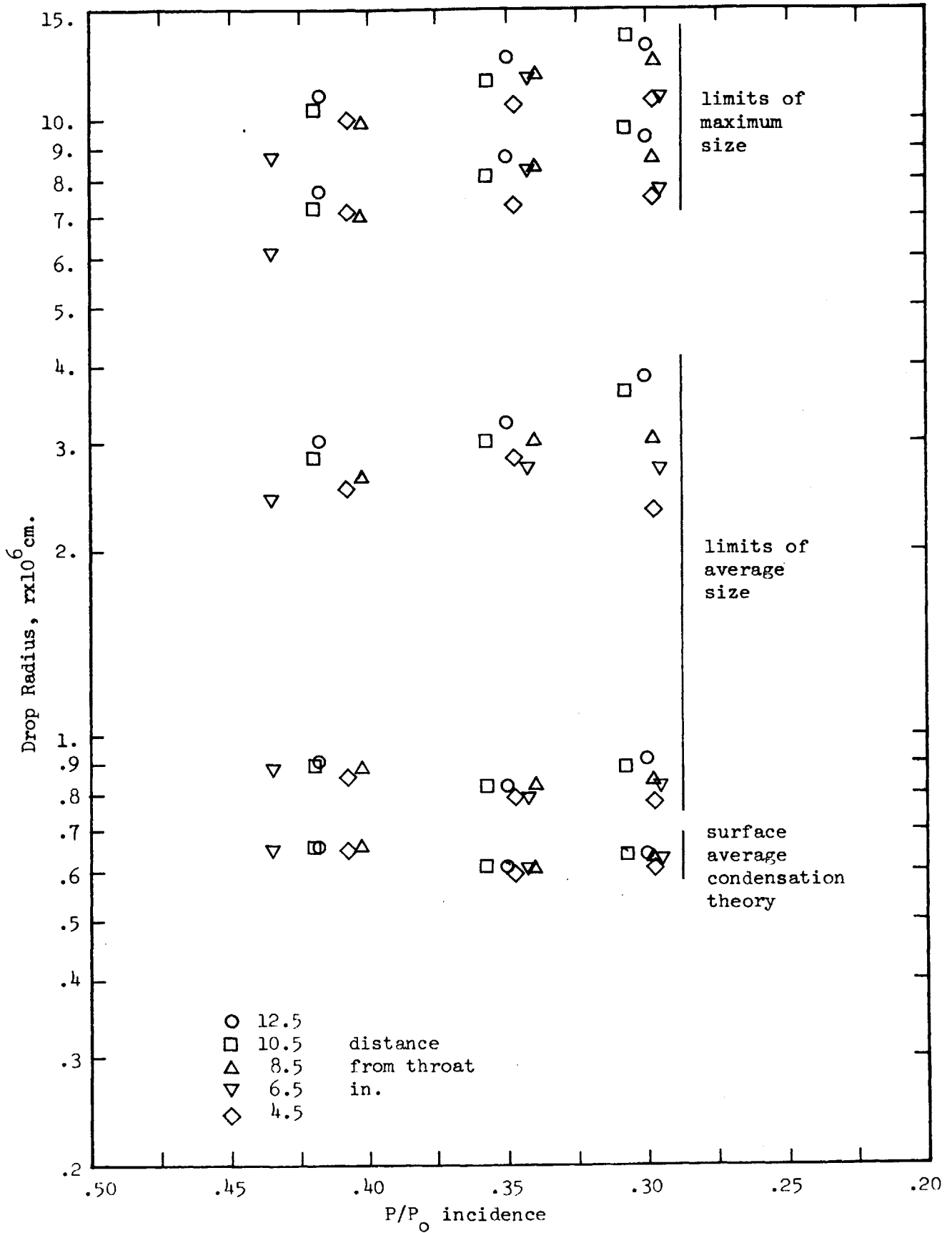
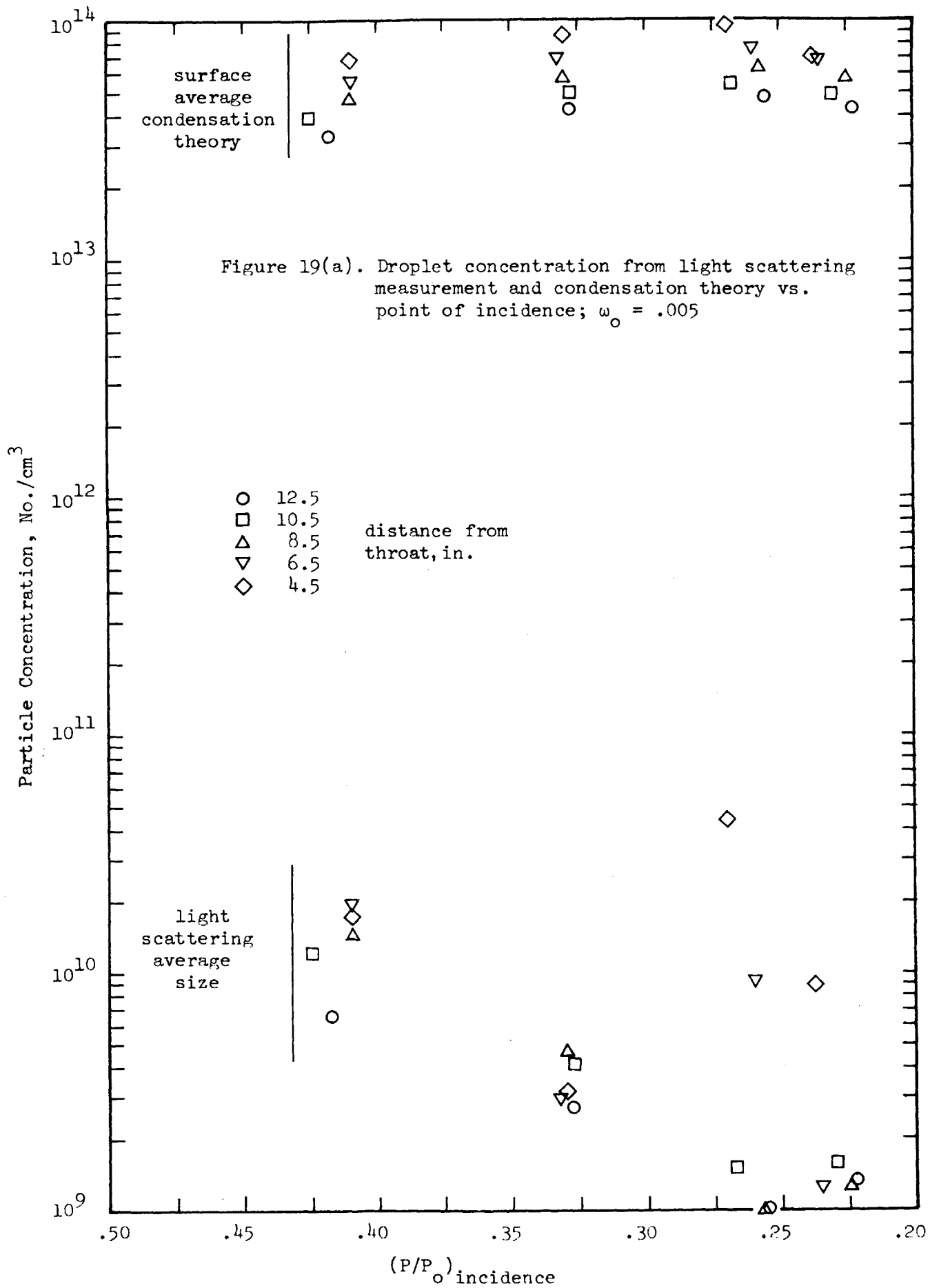
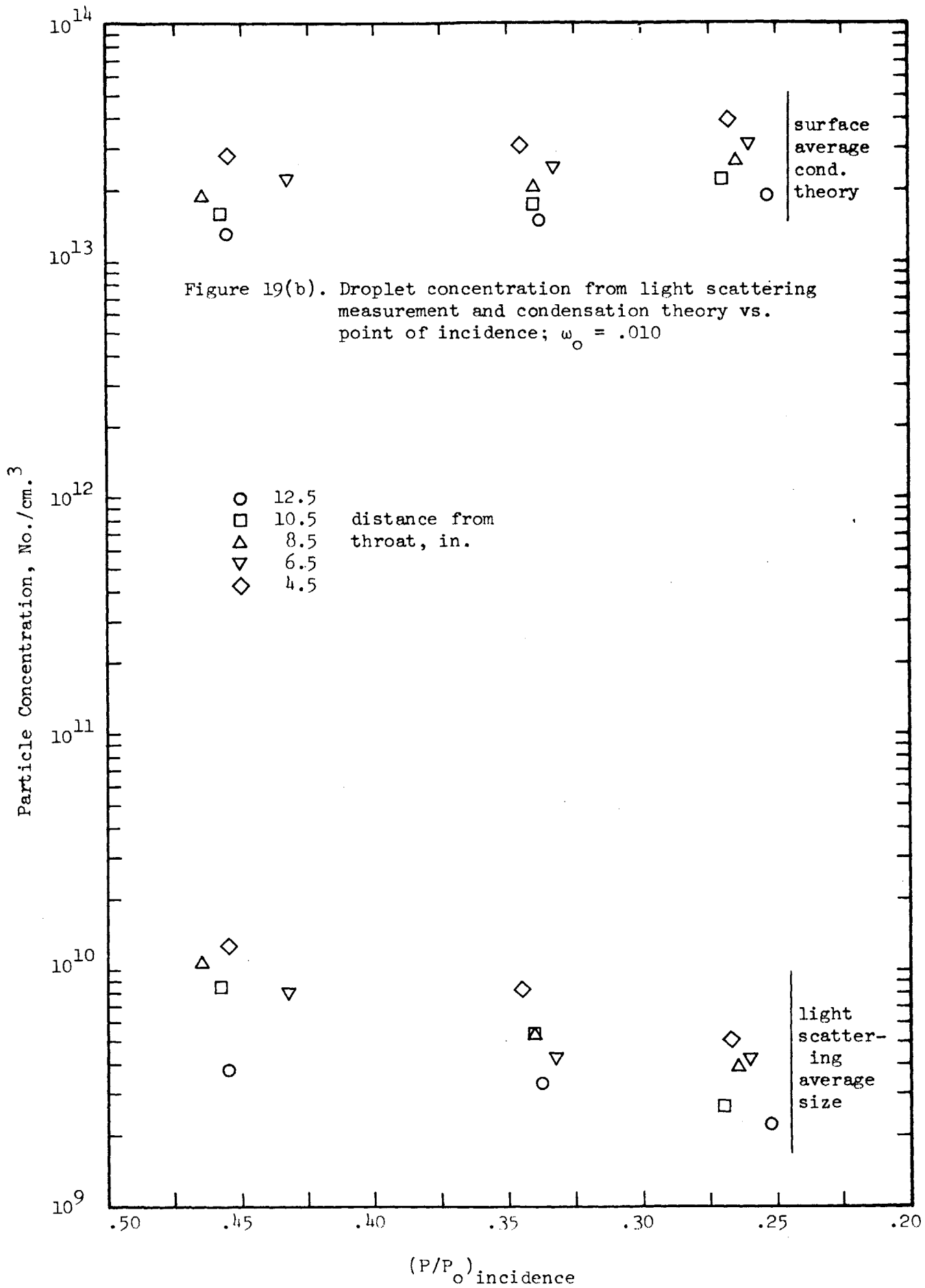
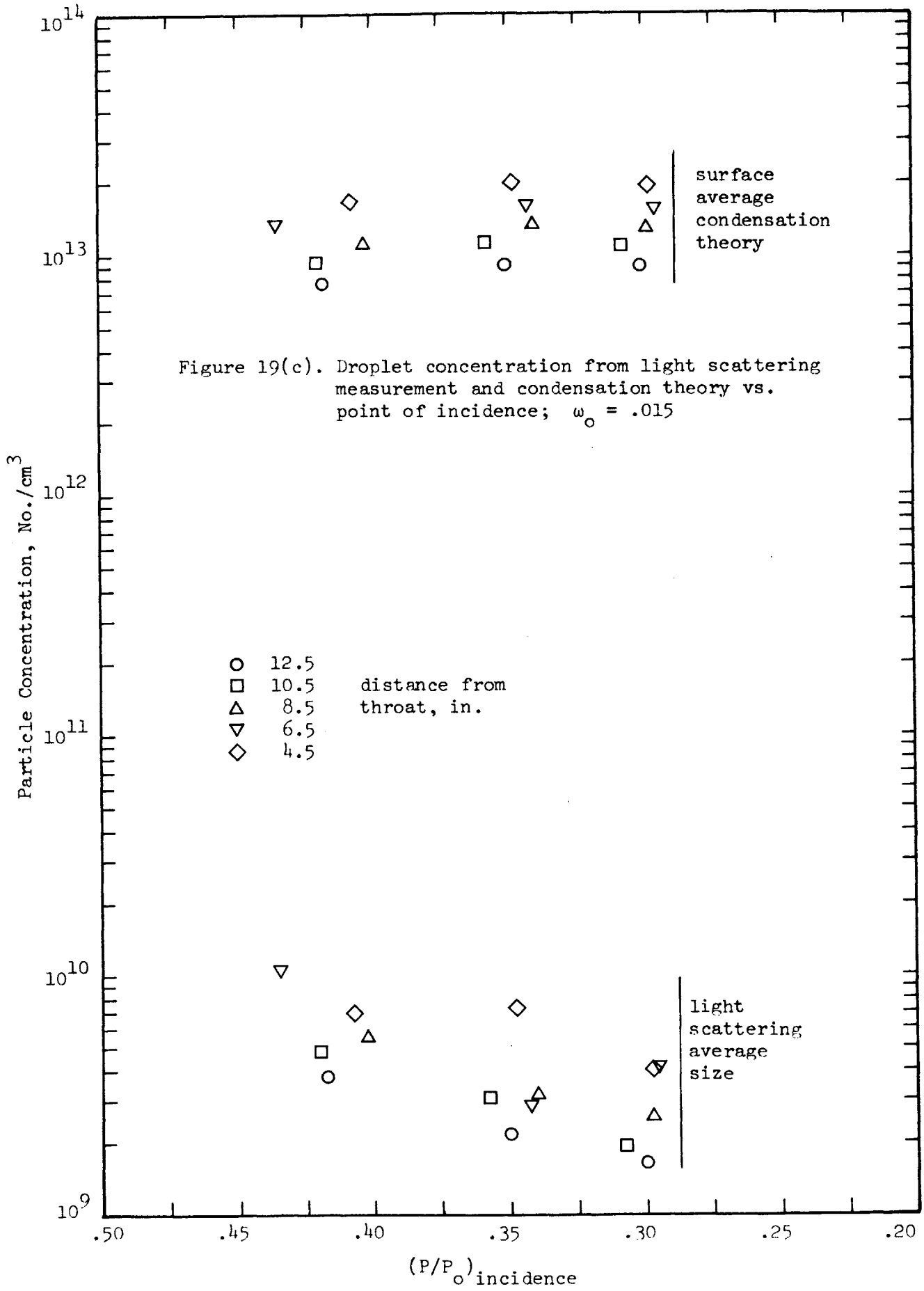


Figure 18(c) Maximum and average droplet size from light scattering measurements; $\omega_0 = .015$







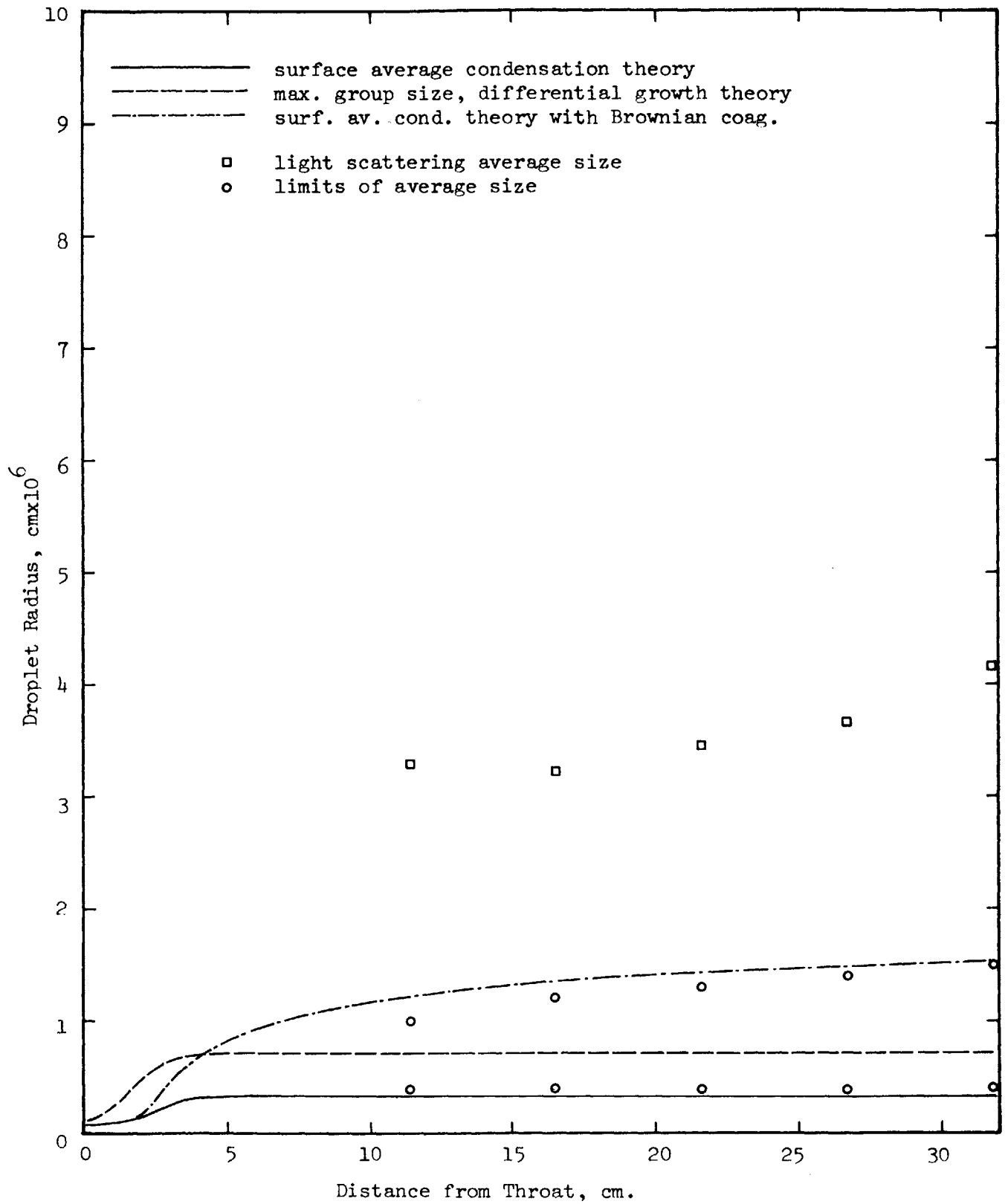


Figure 20(a). Droplet size vs. distance from throat; comparison of theory and experiment, $\omega_o = .005$, $(P/P_o)_i = .42$

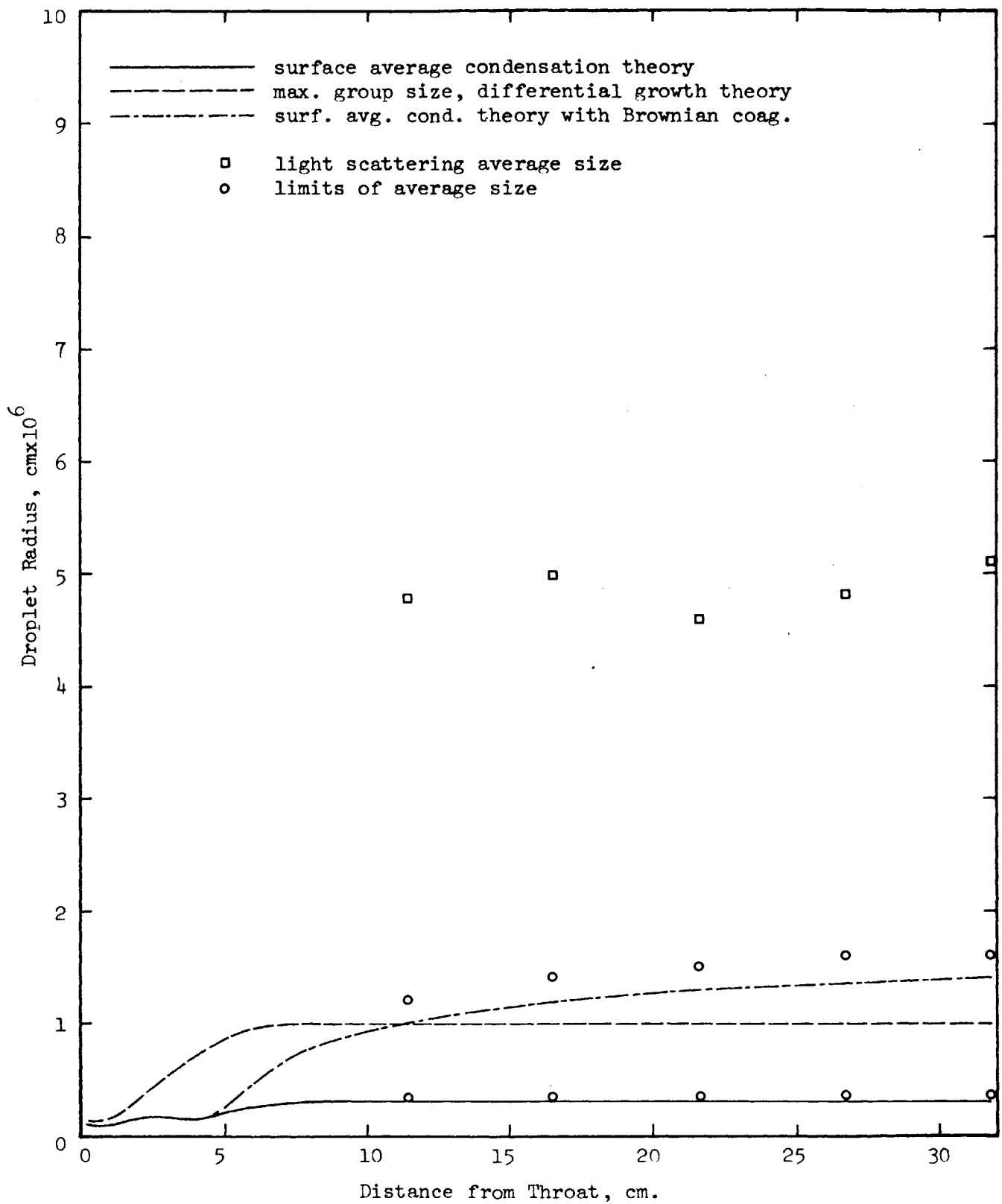


Figure 20(b). Droplet size vs. distance from throat; comparison of theory and experiment, $\omega_o = .005$, $(P/P_o)_i = 0.33$

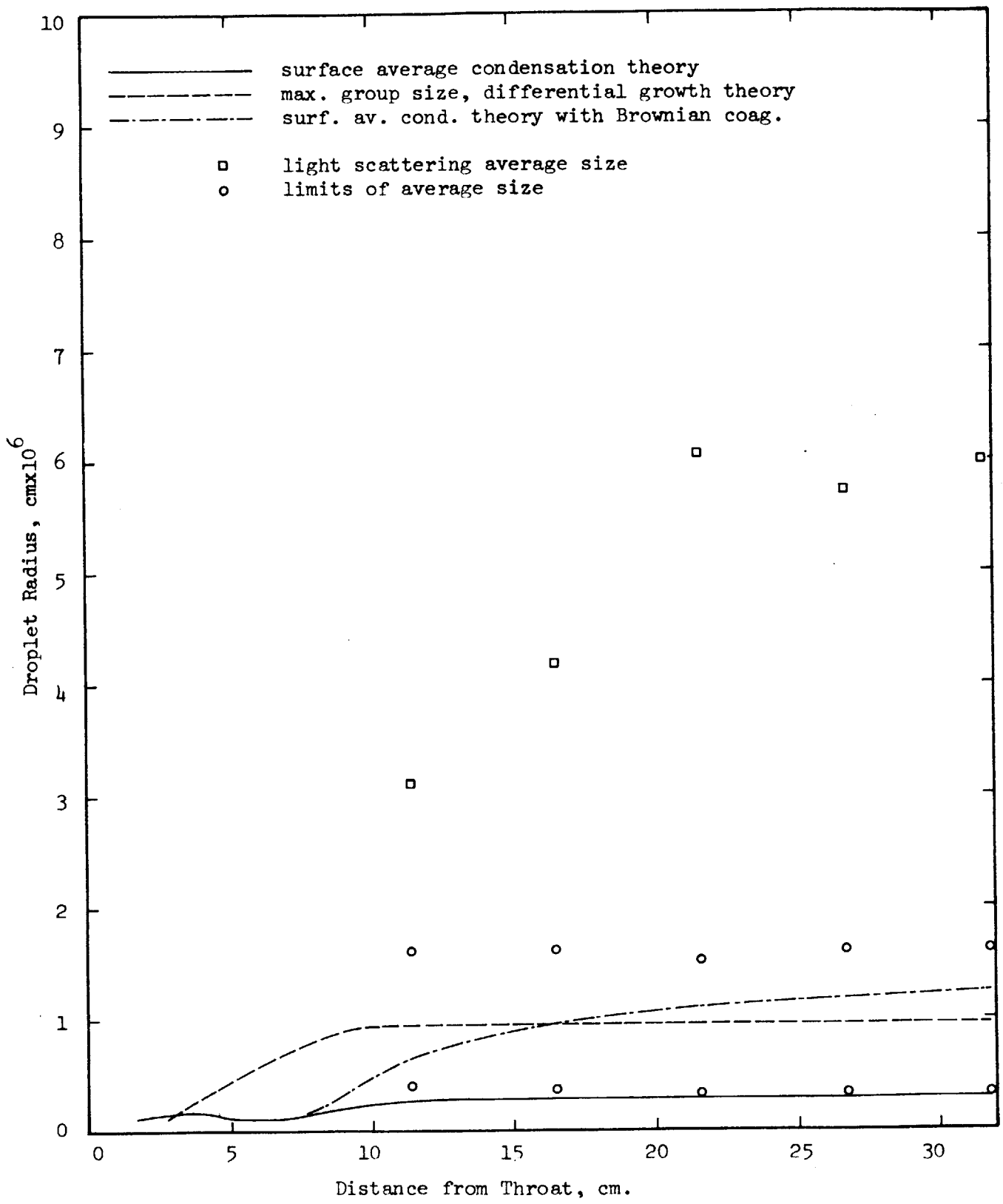


Figure 20(c). Droplet size vs. distance from throat; comparison of theory and experiment, $\omega_o = .005$, $(P/P_o)_i = 0.26$

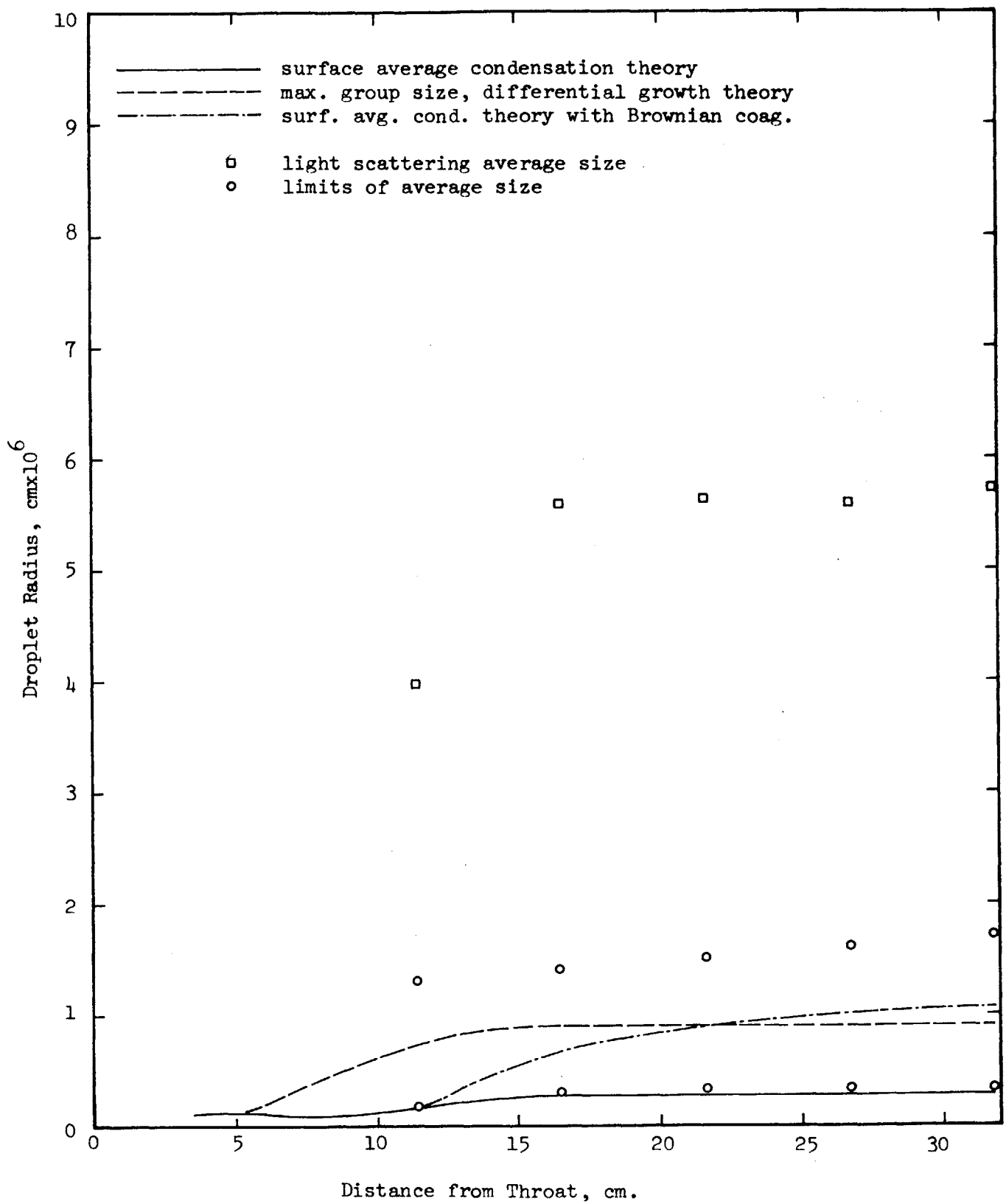


Figure 20(d). Droplet size vs. distance from throat; comparison of theory and experiment, $\omega_o = .005$, $(P/P_o)_i = 0.23$

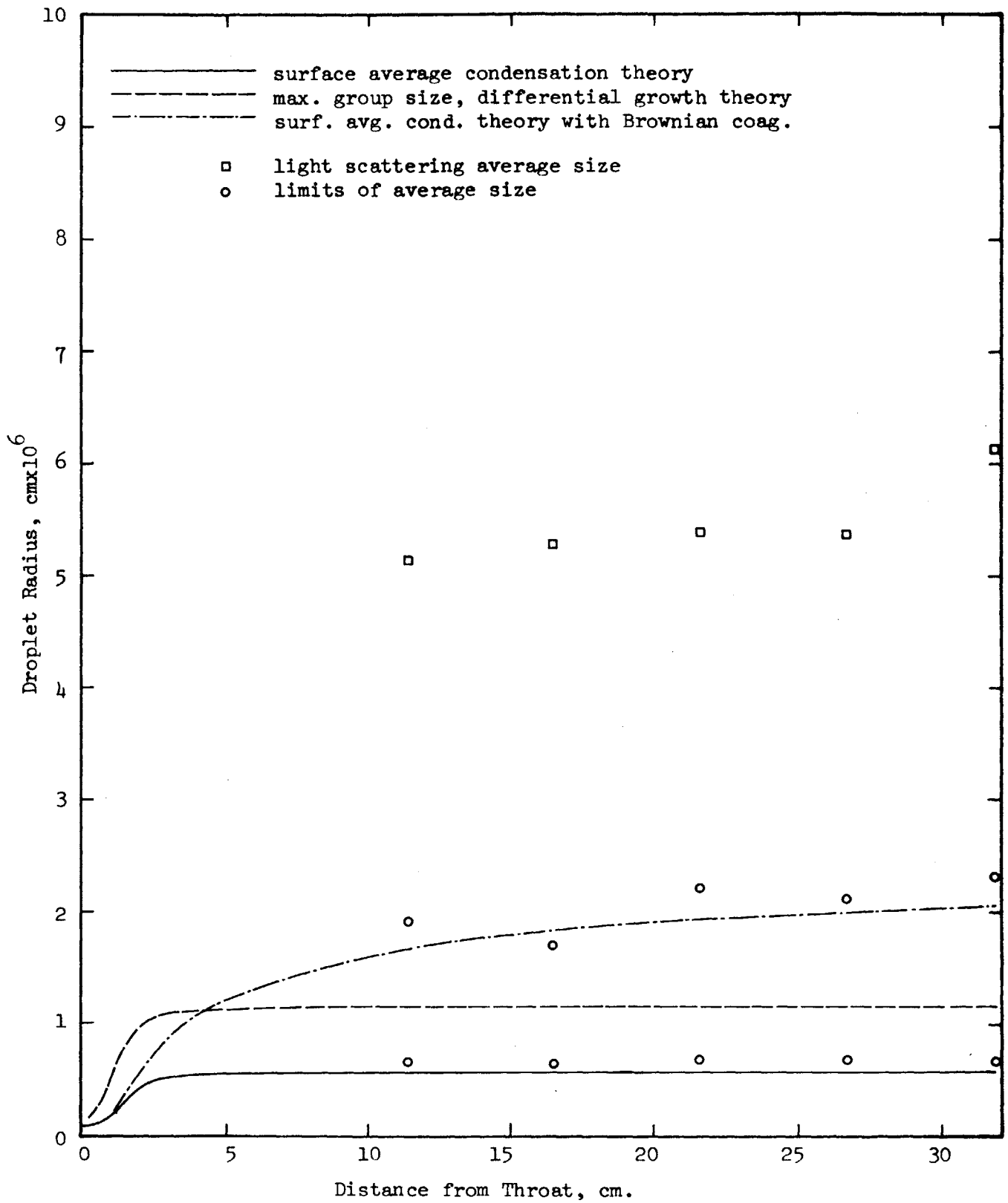


Figure 20(e). Droplet size vs. distance from throat; comparison of theory and experiment, $\omega_o = .010$, $(P/P_o)_i = 0.45$

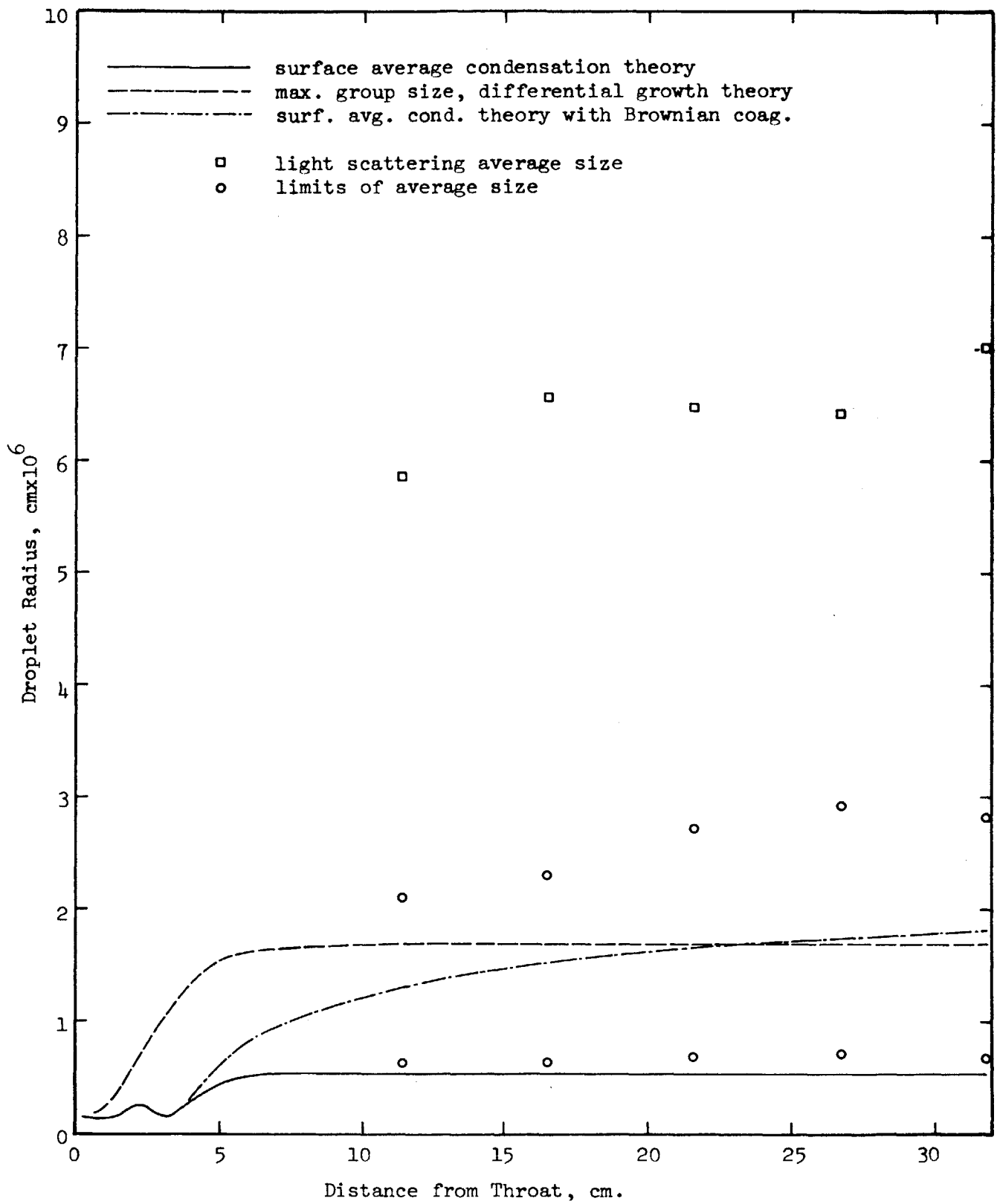


Figure 20(f). Droplet size vs. distance from throat; comparison of theory and experiment, $\omega_o = .010$, $(P/P_o)_i = 0.34$

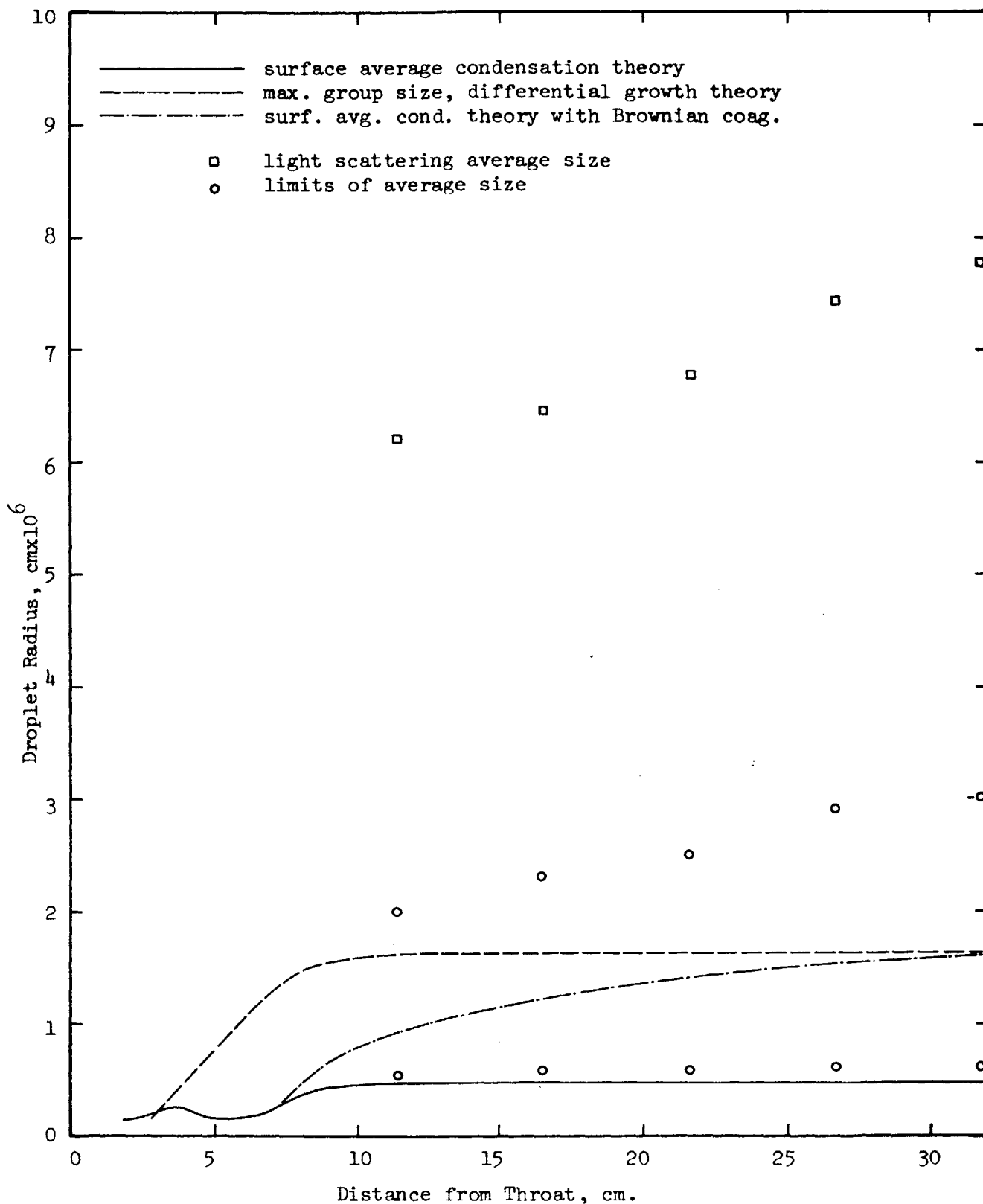


Figure 20(g). Droplet size vs. distance from throat; comparison of theory and experiment, $\omega_o = .010$, $(P/P_o)_i = 0.27$

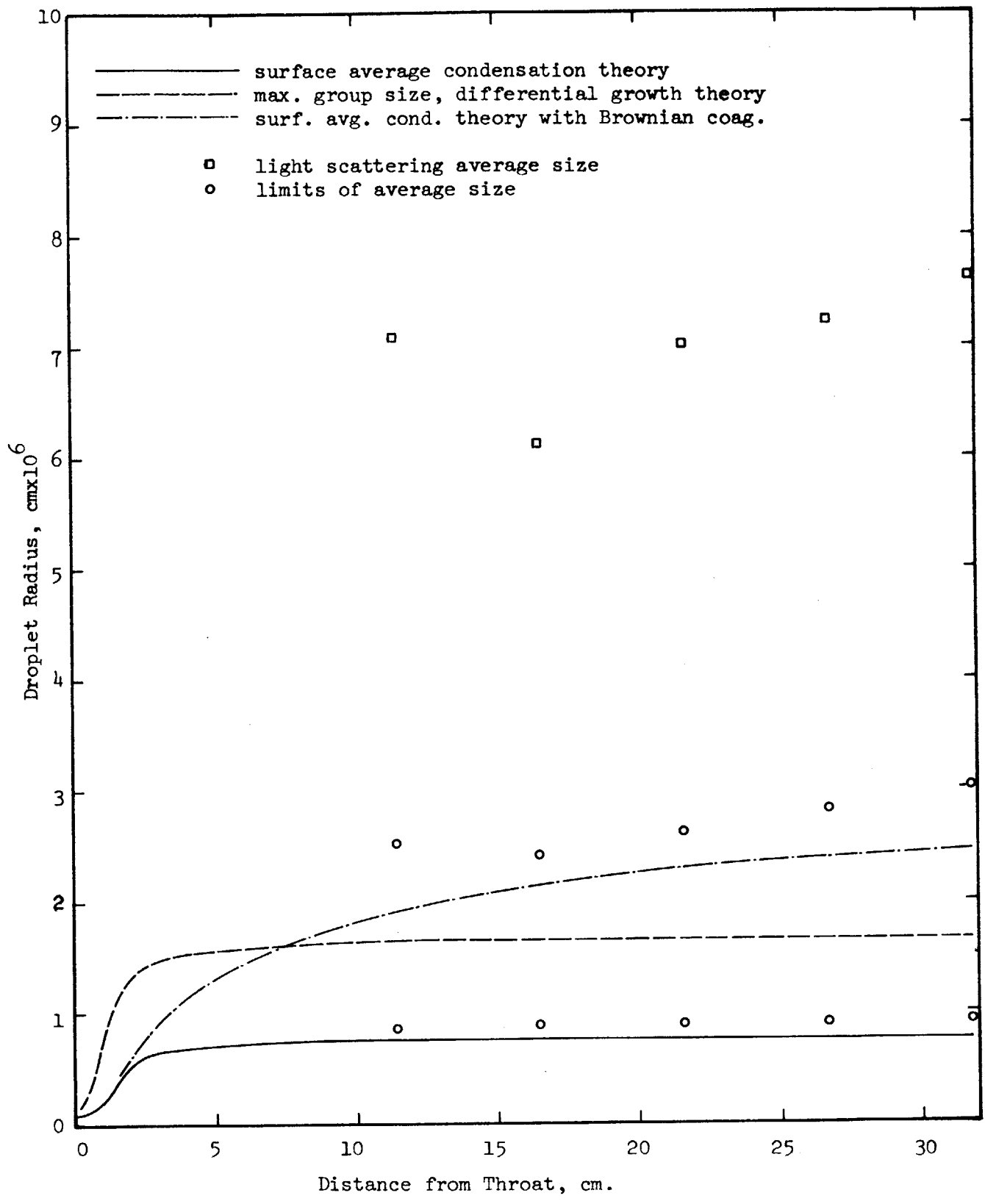


Figure 20(h). Droplet size vs. distance from throat; comparison of theory and experiment, $\omega_o = .015$, $(P/P_o)_i = 0.42$

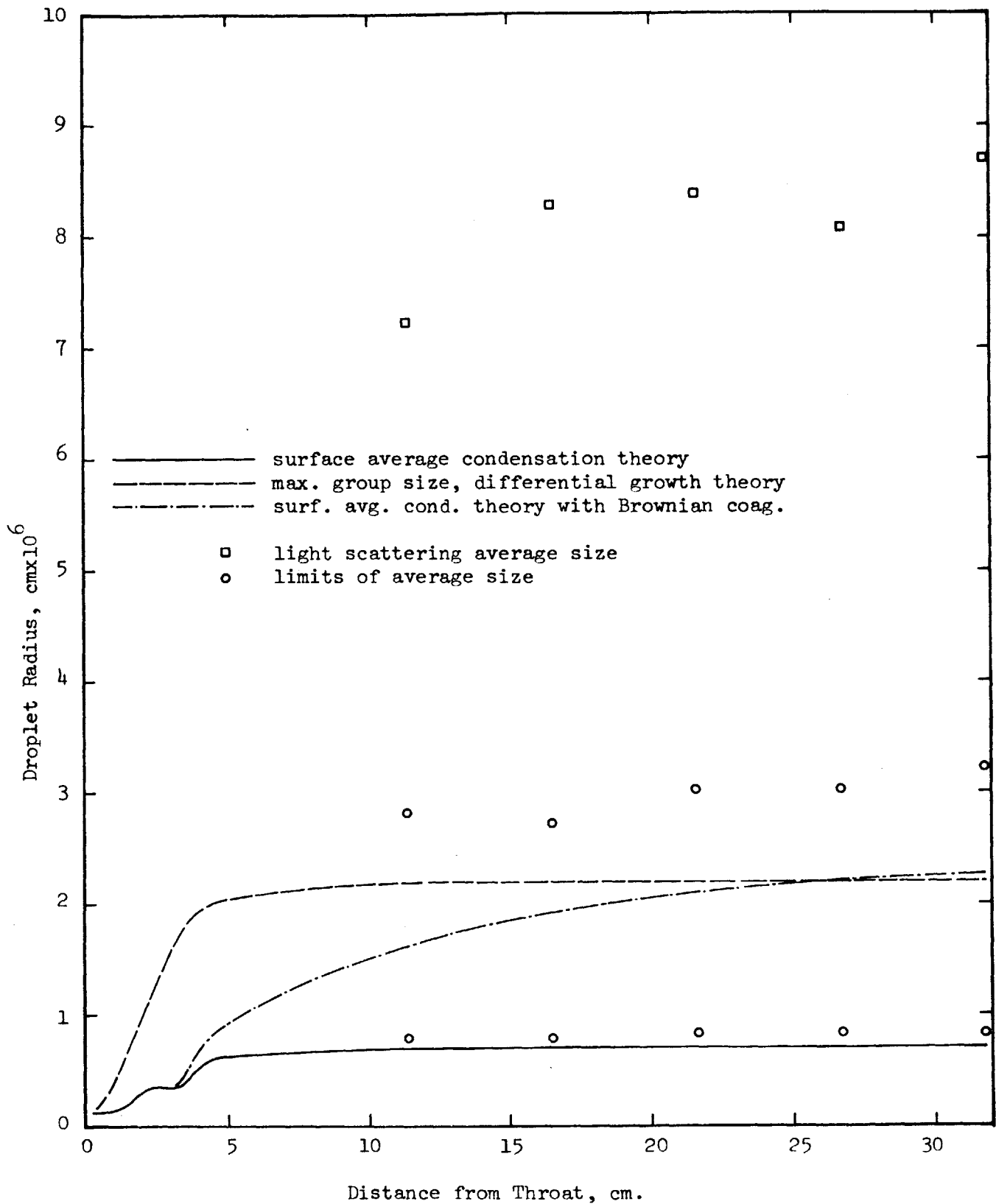


Figure 20(i). Droplet size vs. distance from throat; comparison of theory and experiment, $\omega_o = .015$, $(P/P_o)_i = 0.35$

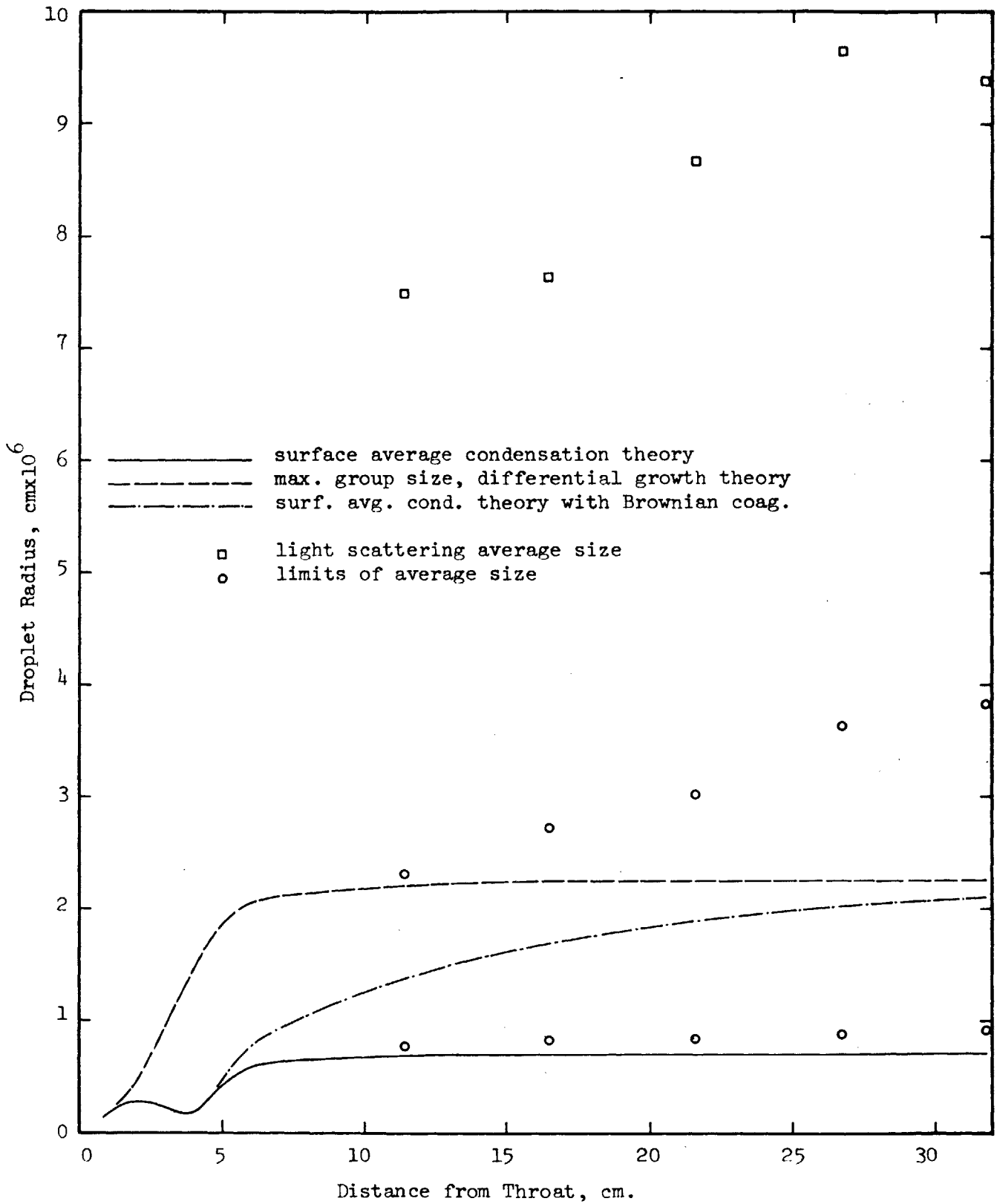


Figure 20(j). Droplet size vs. distance from throat; comparison of theory and experiment, $\omega_o = .015$, $(P/P_o)_i = 0.30$

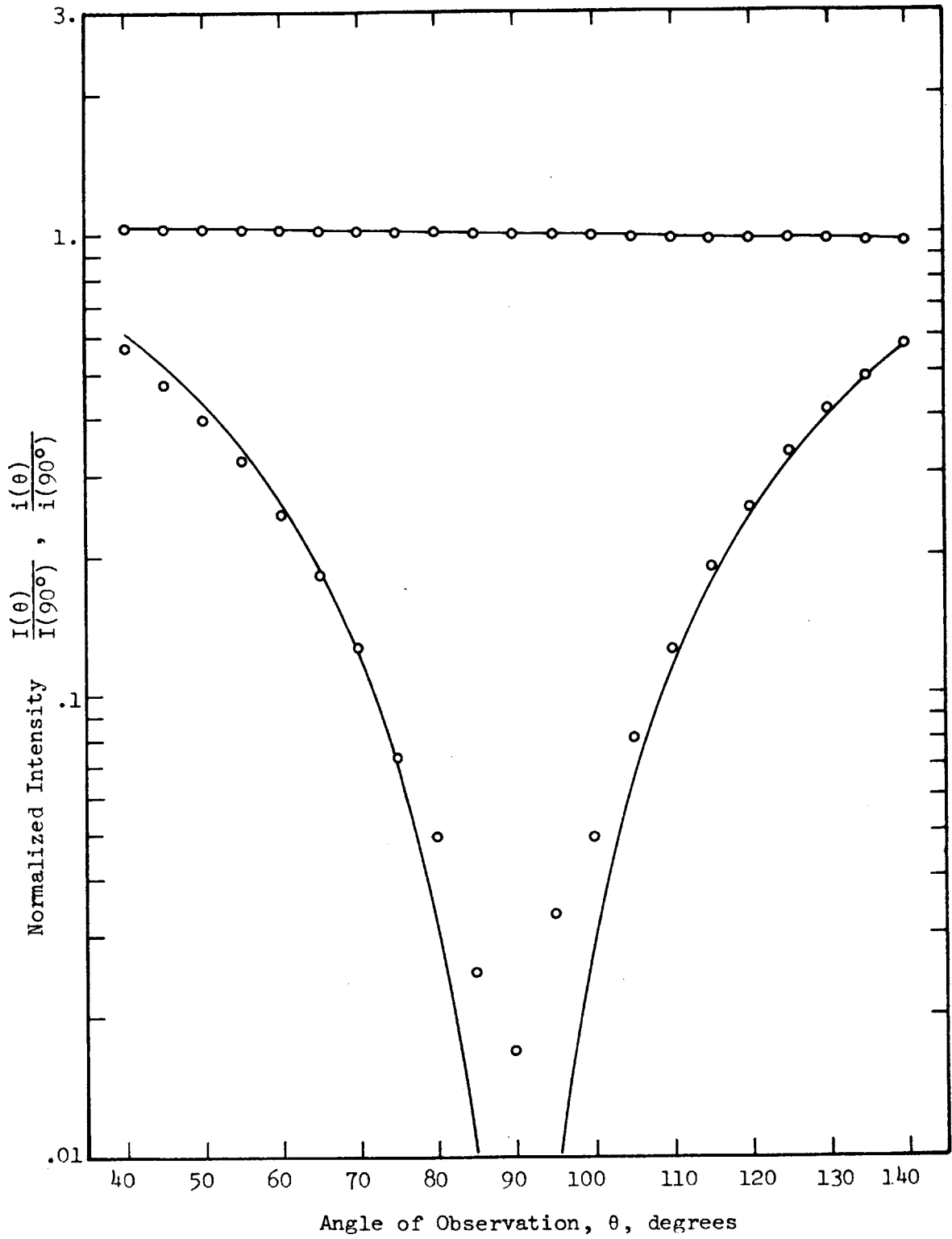


Figure 21. Comparison between theory and experiment, $\alpha = 0.325$

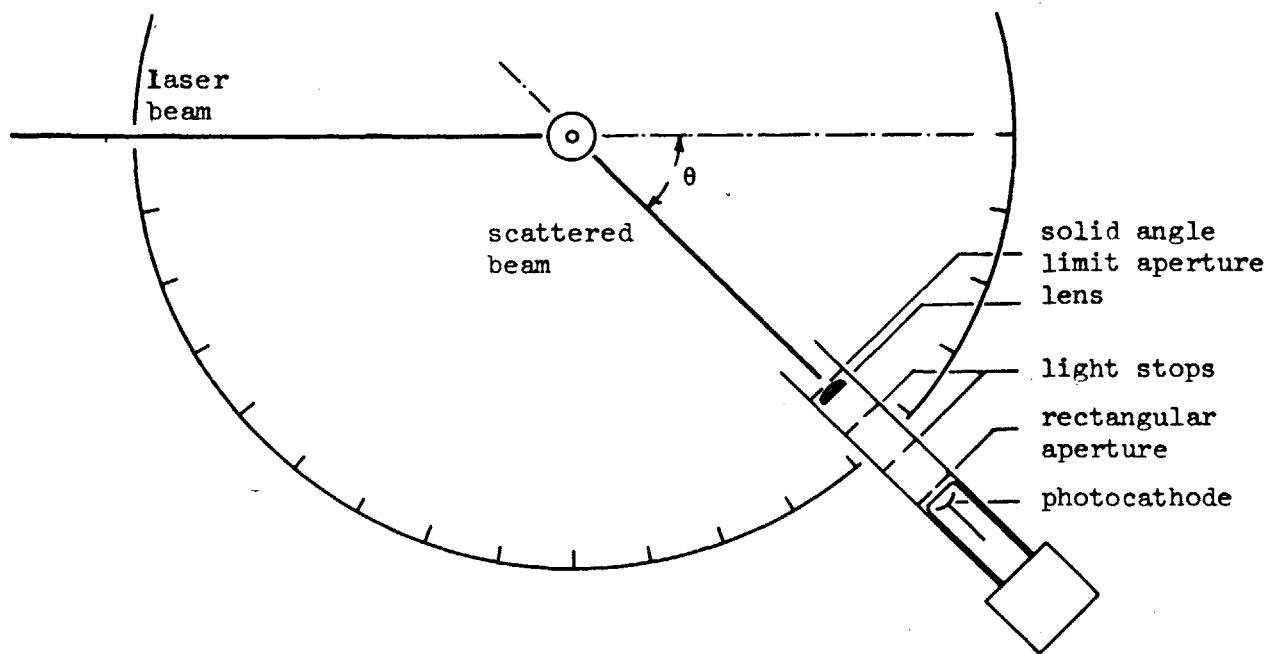


Figure 22(a). Schematic of light scattering geometry

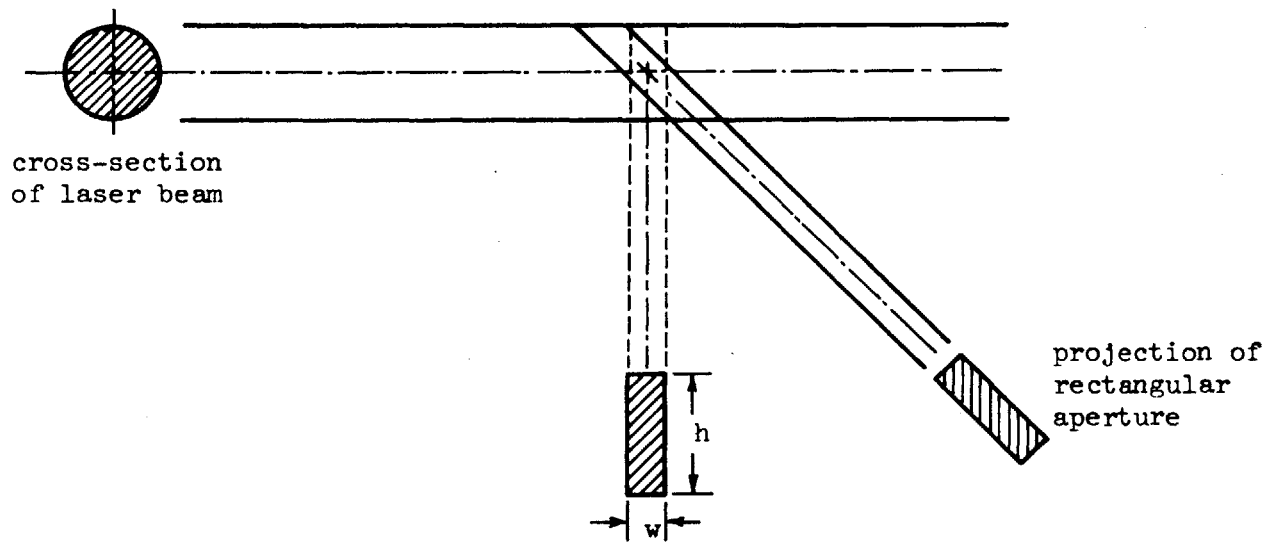


Figure 22(b). Variation of scattering volume with angle

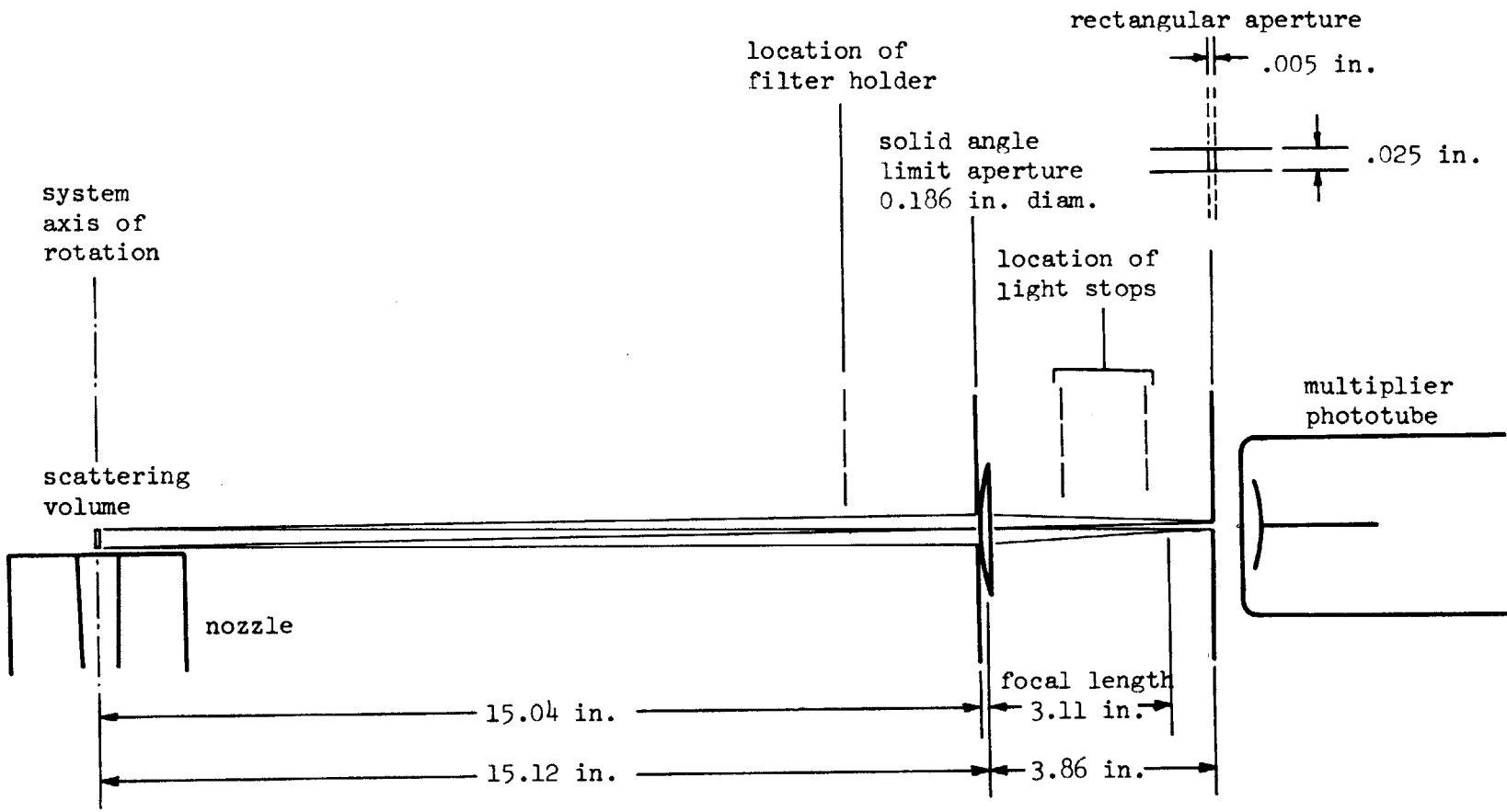


Figure 23. Dimensions of scattered light detection system

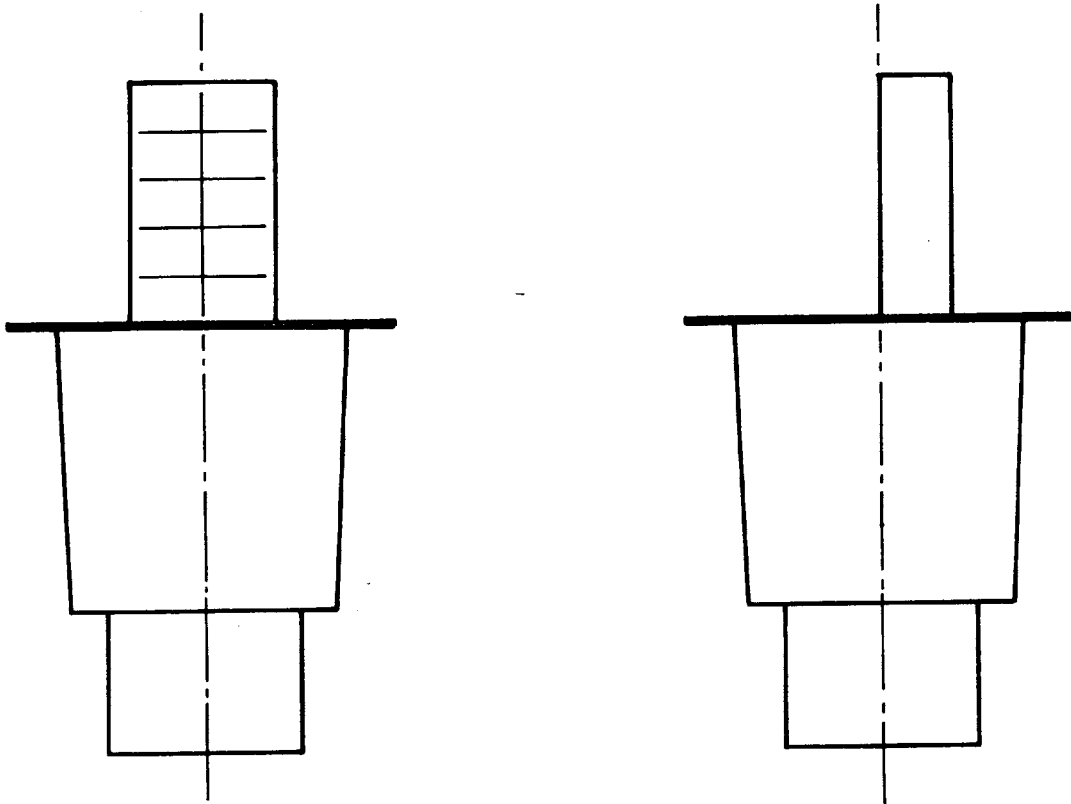


Figure 24(a). Exit plane target

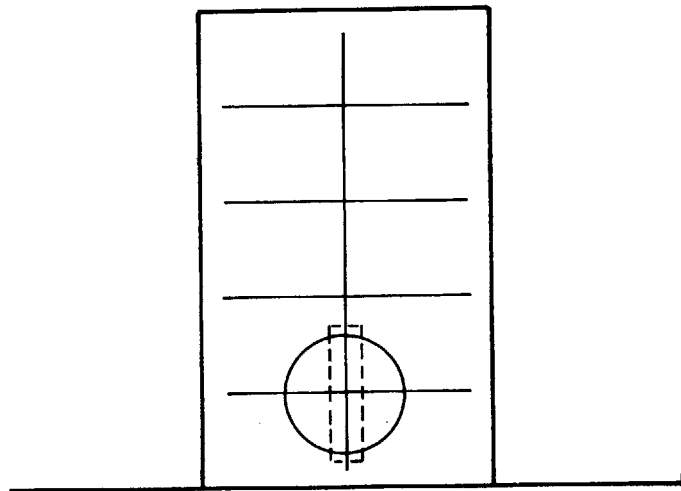


Figure 24(b). Position of alignment images on nozzle target

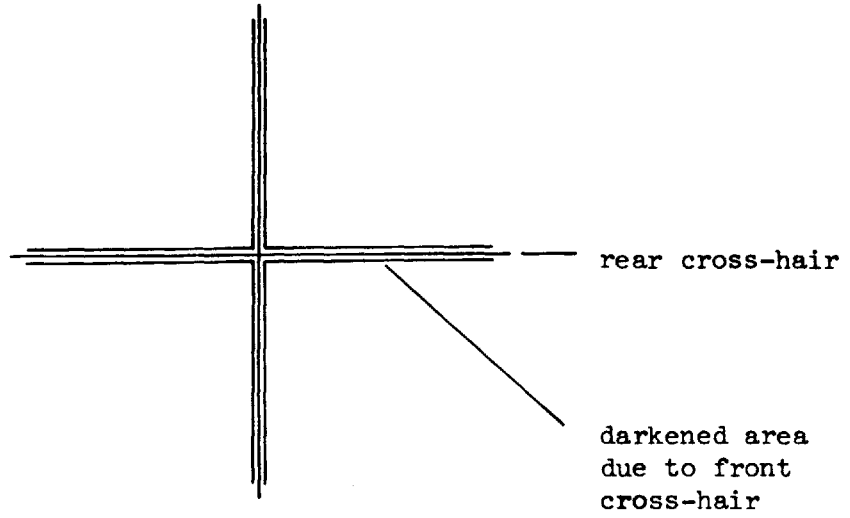


Figure 25(a). Pattern observed when aligning phototube housing

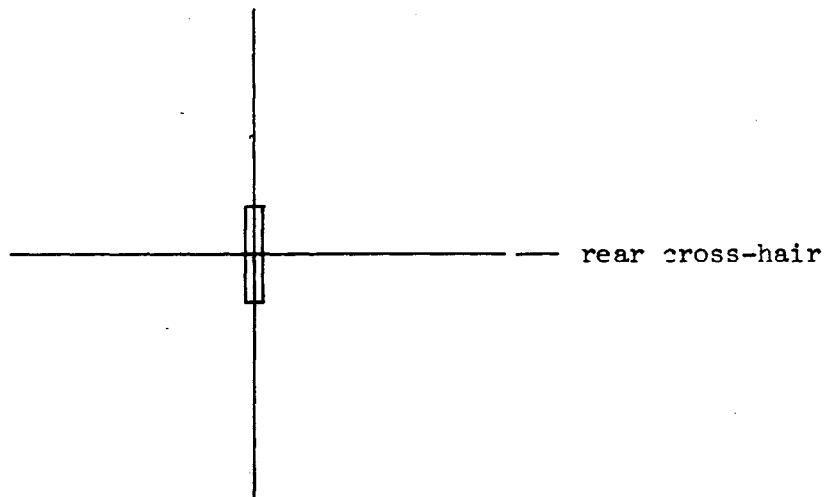


Figure 25(b). Alignment pattern with rectangular aperture installed

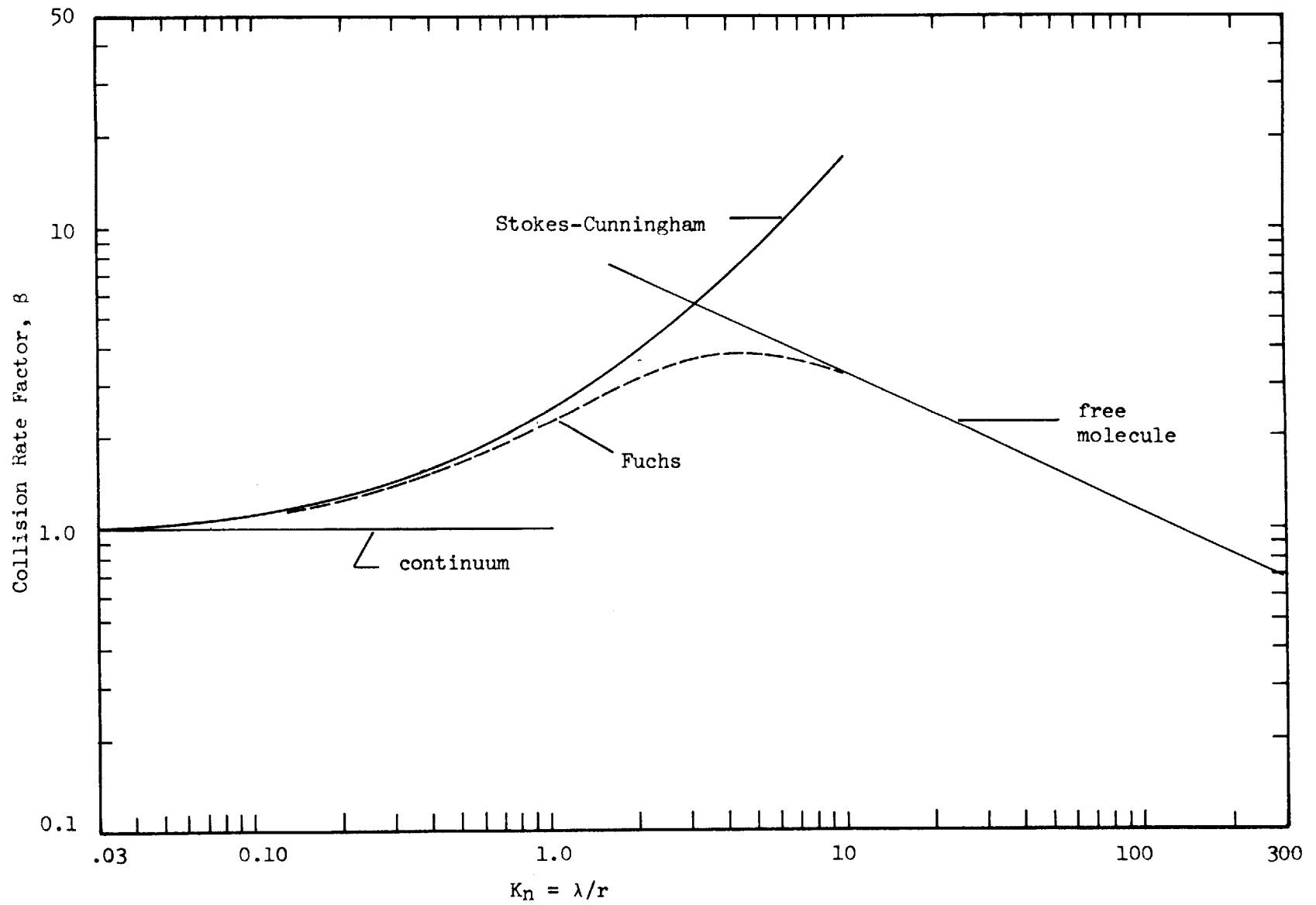


Figure 26. Variation in collision rate with Knudsen number for a homogeneous aerosol

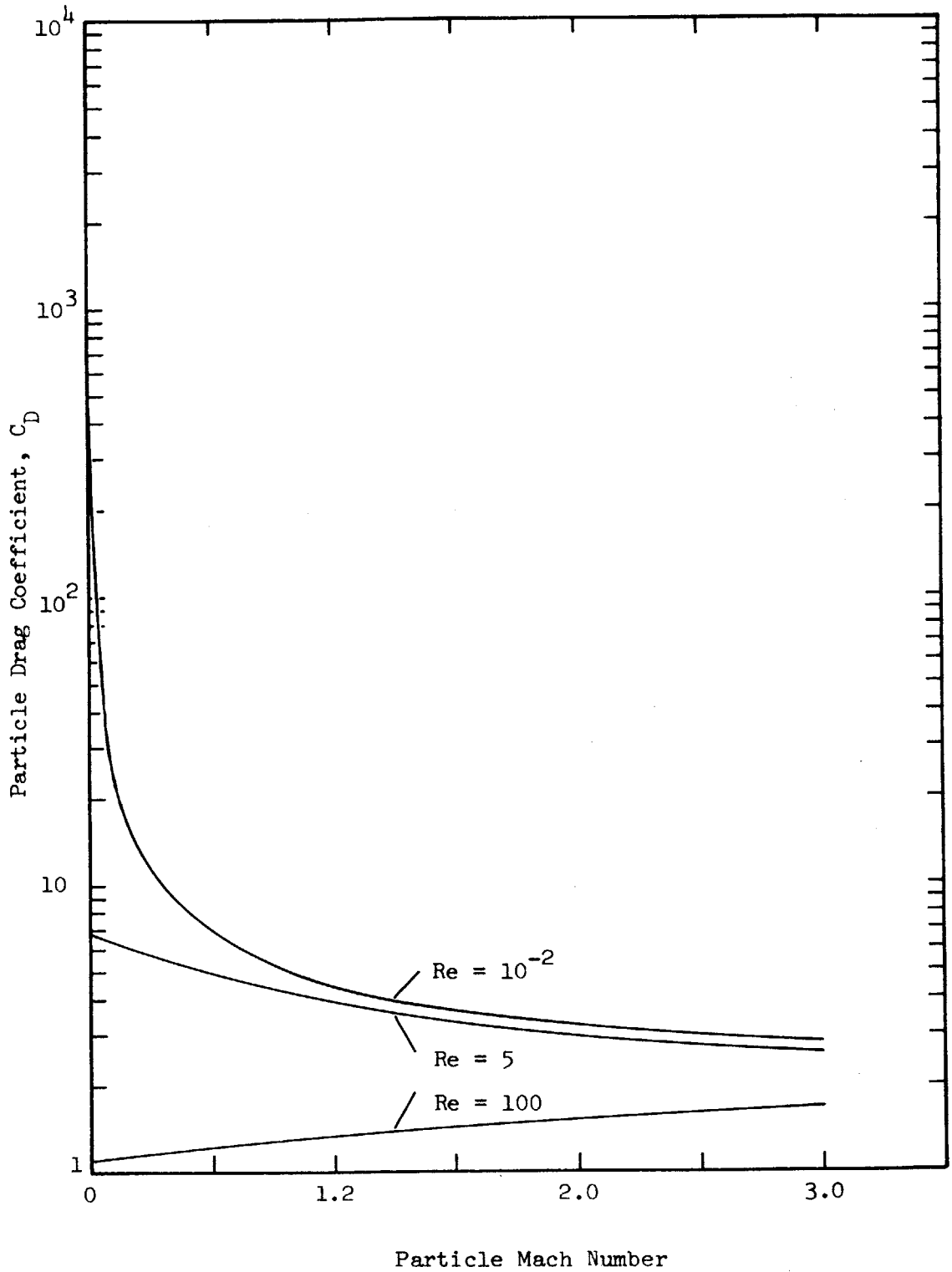


Figure 27. Particle drag coefficient vs. Mach Number for Reynold's Number = .01, 5, 100

INITIAL DISTRIBUTION LIST

<u>Copies</u>	<u>Organization</u>
4	Office of Naval Research Power Branch (Code 429) Department of the Navy Washington, D.C. 20360 Attn: John A. Satkowski
2	Commanding Officer Office of Naval Research Branch Office Box 39, Navy #100, Fleet Post Office New York, New York 09510
1	Dr. F.S. Gardner Office of Naval Research 495 Summer St., Boston, Mass.
6	U.S. Naval Research Laboratory Department of the Navy Washington, D.C. 20390 Attn: Technical Information Division
20	Defense Documentation Center Cameron Street Alexandria, Virginia 22314
1	National Aeronautics and Space Administration Lewis Research Center 21000 Brookpark Road Cleveland, Ohio 44135 Attn: Library
1	Dr. W.D. Jackson Electrical Engineering Department Massachusetts Institute of Technology Cambridge, Massachusetts 02139
1	Dr. W. Courtney Thiokol Chemical Corporation Reaction Motors Division Denville, New Jersey 07834
1	Professor Peter P. Wegener Department of Engineering and Applied Science Yale University 400 Temple Street New Haven, Connecticut 06511
1	Dr. George Rudinger, Jr. Aerodynamic Research Department Cornell Aeronautical Laboratory, Inc. P.O. Box 235 Buffalo, New York 14221

<u>Copies</u>	<u>Organization</u>
1	Dr. S.L. Soo Department of Mechanical and Industrial Engineering University of Illinois Urbana, Illinois 61801
1	Dr. I.S.G. Kovaszny Aeronautics Building The Johns Hopkins University Baltimore, Maryland 21218
1	Professor James Fay Department of Mechanical Engineering Massachusetts Institute of Technology Cambridge, Massachusetts 02139
1	Dr. John E. Scott, Jr. Director, Project SQUID University of Virginia Charlottesville, Virginia 22901
1	Professor John B. Fenn Department of Aerospace and Mechanical Sciences Princeton University Princeton, New Jersey 08540
1	Dr. M.J. Zucrow School of Mechanical Engineering Purdue Research Foundation Purdue University Lafayette, Indiana
1	Dr. D. Elliott Jet Propulsion Laboratory 4800 Oak Grove Drive Pasadena, California 91103
1	Dr. R.S. Levine Rocketdyne 6633 Canoga Avenue Canoga Park, California 91304
	Stanford Research Institute Menlo Park, California 94025
1	Attn: H. Wise
1	M.W. Evans
1	Dr. Chang Shi Nuclear Division Martin-Marietta Corporation Baltimore, Maryland 21203
1	Dr. B.C. Lindley International Research & Development Company, Ltd. Fossway, Newcastle upon Tyne 6, England

Copies

Organization

- 1 Dr. A. Sherman
General Electric Company
Valley Forge Space Technology Center
Post Office Box 8555
Philadelphia, Pennsylvania
- 1 U.S. Naval Ordnance Laboratory
White Oak
Silver Spring, Maryland 20910
Attn: Librarian
- 1 Professor G.M. Pound
Department of Metallurgy
Carnegie Institute of Technology
Pittsburgh, Pennsylvania
- 1 Dr. R. Buckle
Imperial College
London, England
- 1 Dr. W.J. Dunning
The University
Bristol 8, England
- 1 Dr. W. T. Yang
Dept. of Mechanical Engineering
University of New Hampshire
Durham, N.H. 03824

Security Classification

14. KEY WORDS	LINK A		LINK B		LINK C	
	ROLE	WT	ROLE	WT	ROLE	WT
Condensation						
Supersaturated Vapor						
Water Vapor						
Light Scattering						
Droplet Growth						
Droplet Size						

INSTRUCTIONS

1. **ORIGINATING ACTIVITY:** Enter the name and address of the contractor, subcontractor, grantee, Department of Defense activity or other organization (*corporate author*) issuing the report.

2a. **REPORT SECURITY CLASSIFICATION:** Enter the overall security classification of the report. Indicate whether "Restricted Data" is included. Marking is to be in accordance with appropriate security regulations.

2b. **GROUP:** Automatic downgrading is specified in DoD Directive 5200.10 and Armed Forces Industrial Manual. Enter the group number. Also, when applicable, show that optional markings have been used for Group 3 and Group 4 as authorized.

3. **REPORT TITLE:** Enter the complete report title in all capital letters. Titles in all cases should be unclassified. If a meaningful title cannot be selected without classification, show title classification in all capitals in parenthesis immediately following the title.

4. **DESCRIPTIVE NOTES:** If appropriate, enter the type of report, e.g., interim, progress, summary, annual, or final. Give the inclusive dates when a specific reporting period is covered.

5. **AUTHOR(S):** Enter the name(s) of author(s) as shown on or in the report. Enter last name, first name, middle initial. If military, show rank and branch of service. The name of the principal author is an absolute minimum requirement.

6. **REPORT DATE:** Enter the date of the report as day, month, year; or month, year. If more than one date appears on the report, use date of publication.

7a. **TOTAL NUMBER OF PAGES:** The total page count should follow normal pagination procedures, i.e., enter the number of pages containing information.

7b. **NUMBER OF REFERENCES:** Enter the total number of references cited in the report.

8a. **CONTRACT OR GRANT NUMBER:** If appropriate, enter the applicable number of the contract or grant under which the report was written.

8b, 8c, & 8d. **PROJECT NUMBER:** Enter the appropriate military department identification, such as project number, subproject number, system numbers, task number, etc.

9a. **ORIGINATOR'S REPORT NUMBER(S):** Enter the official report number by which the document will be identified and controlled by the originating activity. This number must be unique to this report.

9b. **OTHER REPORT NUMBER(S):** If the report has been assigned any other report numbers (*either by the originator or by the sponsor*), also enter this number(s).

10. **AVAILABILITY/LIMITATION NOTICES:** Enter any limitations on further dissemination of the report, other than those

imposed by security classification, using standard statements such as:

- (1) "Qualified requesters may obtain copies of this report from DDC."
- (2) "Foreign announcement and dissemination of this report by DDC is not authorized."
- (3) "U. S. Government agencies may obtain copies of this report directly from DDC. Other qualified DDC users shall request through _____."
- (4) "U. S. military agencies may obtain copies of this report directly from DDC. Other qualified users shall request through _____."
- (5) "All distribution of this report is controlled. Qualified DDC users shall request through _____."

If the report has been furnished to the Office of Technical Services, Department of Commerce, for sale to the public, indicate this fact and enter the price, if known.

11. **SUPPLEMENTARY NOTES:** Use for additional explanatory notes.
12. **SPONSORING MILITARY ACTIVITY:** Enter the name of the departmental project office or laboratory sponsoring (*paying for*) the research and development. Include address.
13. **ABSTRACT:** Enter an abstract giving a brief and factual summary of the document indicative of the report, even though it may also appear elsewhere in the body of the technical report. If additional space is required, a continuation sheet shall be attached.

It is highly desirable that the abstract of classified reports be unclassified. Each paragraph of the abstract shall end with an indication of the military security classification of the information in the paragraph, represented as (TS), (S), (C), or (U).

There is no limitation on the length of the abstract. However, the suggested length is from 150 to 225 words.

14. **KEY WORDS:** Key words are technically meaningful terms or short phrases that characterize a report and may be used as index entries for cataloging the report. Key words must be selected so that no security classification is required. Identifiers, such as equipment model designation, trade name, military project code name, geographic location, may be used as key words but will be followed by an indication of technical context. The assignment of links, rules, and weights is optional.